

# High-precision polarizability and transition amplitude measurements in In and Pb using vapor cell and atomic beam spectroscopy

by  
Bingyi Wang

Professor Protik K. Majumder, Advisor

A thesis submitted in partial fulfillment  
of the requirements for the  
Degree of Bachelor of Arts with Honors  
in Physics

WILLIAMS COLLEGE  
Williamstown, Massachusetts  
May 20, 2018

# Abstract

This thesis includes recent work in two precision measurements using laser spectroscopy in indium and lead. First, I present the completed high-precision measurements of the Stark shift polarizabilities in the  $7P_{1/2}$  and  $7P_{3/2}$  excited states of  $^{115}\text{In}$  in an atomic beam. Our final result for the scalar polarizabilities are  $1.811(4) \times 10^5 a_0^3$  and  $2.876(6) \times 10^5 a_0^3$  for the  $7P_{1/2}$  and  $7P_{3/2}$  states respectively (in atomic units). These are a factor of 30 to 50 times greater than the previously measured indium polarizabilities in our lab. For the tensor polarizability component of the  $7P_{3/2}$  state, we estimate its value to be  $-1.43(18) \times 10^4 a_0^3$ . These measurements represent the first high-precision benchmarks of transition properties of such high excited states of trivalent atomic systems. The precision of our experiment is sufficient to differentiate between the *ab initio* calculations of indium polarizabilities using two distinct theoretical models, as well as to allow precise determination of the indium  $7P-6D$  matrix elements. Second, I present our progress towards measuring the  $6s^26p^2\ ^3P_0 \rightarrow\ ^3P_2$  electric quadrupole (E2) transition amplitude in relation to the known  $6s^26p^2\ ^3P_0 \rightarrow\ ^3P_1$  magnetic dipole (M1) transition amplitude, using Faraday rotation spectroscopy in a lead vapor cell. We employ the Faraday rotation technique to detect induced optical rotations with sensitivity at the few  $\mu\text{rad}$  level, revealing the previously unobserved E2 transition. We have improved the apparatus and developed a new data acquisition and analysis method, as necessary preparatory work to a precise measurement of the E2 transition amplitude. Both precise measurements serve as tests to recent theoretical predictions of these quantities and provide much-needed guidance for the future refinement of theoretical approaches to complicated atomic systems.

# Executive Summary

This thesis presents two distinct high-precision measurements of atomic Stark shift and transition amplitudes using laser spectroscopy in indium and lead respectively. Both projects have been undertaken in collaboration with our theory colleague, Marianna Safronova, who has recently developed new approaches to calculating the wavefunctions of multi-valence-electron atomic systems. Our precise measurements of atomic observables, such as polarizability and transition amplitude, ultimately test and guide *ab initio* atomic theory calculations.

The thesis first describes the completed high-precision measurements of the  $7P$  excited states Stark shift polarizabilities in indium. We adopt a two-step excitation method in an indium atomic beam to realize the measurements. The indium sample is contained in a vacuum system held at roughly  $10^{-7}$  Torr and heated to above  $1100$  °C to produce a beam of atoms. The atomic beam interacts with two overlapped laser beams, which drive the two-step transition from the ground state. A 410 nm laser is locked to the first-step transition resonance. A second red laser (690 nm or 685 nm depending on the excited state) scans across the second-step transition resonant frequency. The interaction between atoms and the radiation fields is confined to a small region between parallel plates that produce a DC electric field on the order of a few kV/cm. With appropriate lock-in demodulation methods, we observe the absorption spectra and compare the relative frequency shift between the spectral peaks when the external electric field is turned on (from off). We use a LabVIEW program to systematically alter field strength and acquire data (typical data shown in Figure 1), which are later analyzed with MATLAB programs to find the Stark shift. Taking into account the known polarizabilities of the ground state and the intermediate state that our group has previously measured, we can then extract the  $7P_{1/2, 3/2}$  excited state polarizabilities.

We conclude that the (scalar) polarizability for indium  $7P_{1/2}$  state is  $1.811(4) \times 10^5 a_0^3$  in atomic units. For the more complicated  $7P_{3/2}$  state, we measure the scalar polarizability to be  $2.876(6) \times 10^5 a_0^3$  and the tensor polarizability to be  $-1.43(18) \times 10^4 a_0^3$  (both in atomic units). Measurements for both states are more than an order of magnitude larger than any previous polarizability measurement in our lab. These experimental results achieve sub-1% level of uncertainty for the scalar polarizabilities, and approximately 12% uncertainty for the tensor component of the  $7P_{3/2}$  state, all of which provide benchmarks to guide the development of more precise theoretical calculations. These values, together with past measurements of

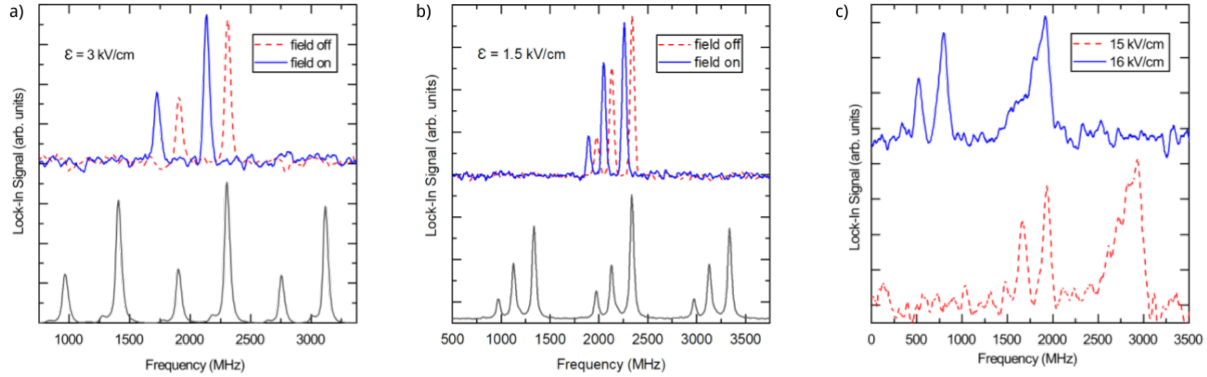


Figure 1: Typical indium absorption spectra depicting both Stark-shifted and unshifted case in each plot. a) Top half shows a typical scan for the  $7P_{1/2}$  excited state in the atomic beam and the bottom half shows an unshifted reference absorption signal from an indium vapor cell, with sidebands generated by an electro-optic modulator. Each peak corresponds to one hyperfine level. b) Top half represents the  $7P_{3/2}$  state data taken in the low electric field regime, where the scalar component of the polarizability dominates. Bottom half similarly shows the vapor cell reference signal. Due to selection rules, only three hyperfine levels out of four can be accessed through a particular excitation path. c) A typical atomic beam absorption signal of the  $7P_{3/2}$  state under a high field, where the tensor polarizability plays a non-negligible role. No vapor cell reference is involved in this regime, for reasons I will explain later.

indium Stark shift polarizabilities in a series of excited states, provide important tests for two different theoretical models (the so-called CC model and CI+all-order model) as illustrated in Figure 2. Our experimental measurements are consistent with both theories within error bars, but in terms of the center values, the CI+all-order approach to the trivalent system yields better predictions of the polarizabilities in indium. This work was recently published in collaboration with our theory colleagues.

Second, we present our progress towards measuring the electric quadrupole (E2) ( $6s^26p^2\ ^3P_0 \rightarrow\ ^3P_2$ ) transition amplitude in  $^{208}\text{Pb}$  using Faraday rotation spectroscopy. Because the forbidden E2 transition is too weak to be detected from direct absorption, unlike the case in the indium experiment, we indirectly infer the E2 transition amplitude using a sensitive Faraday rotation technique. In order to minimize the error from measuring experimental conditions involved in this technique, we in fact apply the technique to the E2 transition and a known magnetic dipole (M1) transition ( $6s^26p^2\ ^3P_0 \rightarrow\ ^3P_1$ ), and measure the ratio between the two transition amplitudes. Keeping all experimental conditions identical for both transitions, we can simply cancel these terms when taking the ratio. This M1 transition amplitude in lead has been precisely calculated and can be readily measured via absorption spectroscopy, making the extraction of the E2 transition amplitude straightforward. We alternately send two infrared lasers, tuned to the resonant frequencies of the two transitions,

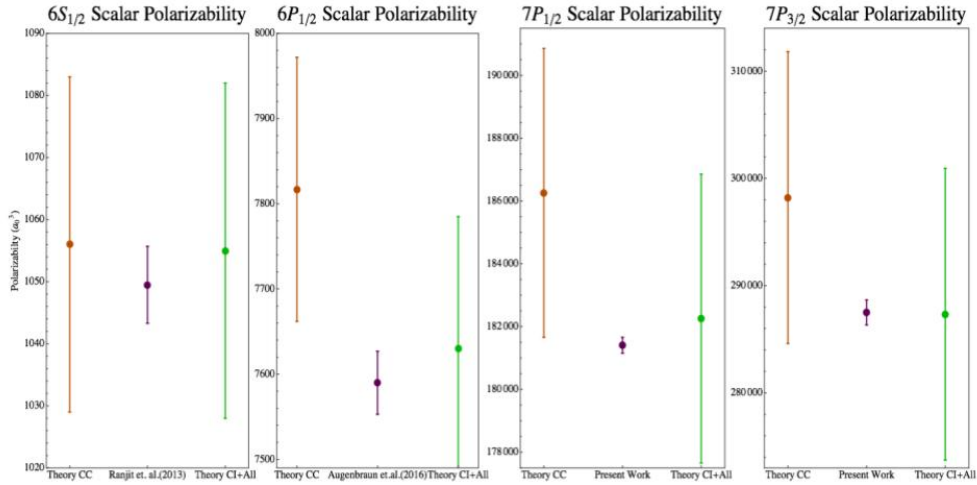


Figure 2: Summary of our experimental values for indium polarizabilities in the  $6S_{1/2}$ ,  $6P_{1/2}$ ,  $7P_{1/2}$ , and  $7P_{3/2}$  excited states, in comparison with the theoretical calculations using two distinct models for each state. The yellow data points show polarizability values calculated using the CC (coupled-cluster) model, a model based on a single valence system, while the green data points are predictions from the CI+all-order (configuration-interaction + all-order) method, a trivalent-electron approach. The middle purple data point in each plot is our experimental result.

to pass through a  $^{208}\text{Pb}$  cell heated to around 950 °C. We assemble a polarimeter system consisting of two crossed polarizers and place the heated lead vapor cell along with a Faraday modulation rod in between, so that once we apply external magnetic field, the induced optical rotation in the atoms and in the rod allows some light with rotated polarization to pass through. A schematic of the Faraday rotation setup is shown in Figure 3. This Faraday rotation technique is sensitive to small rotation signals down to a few  $\mu\text{rad}$ . With effective demodulation schemes, we pick out the tiny rotation signal from the background noise, from which we could infer the transition amplitude.

The spectral lineshapes from the Faraday rotation spectroscopy, as well as in the transmission spectra (for the M1 transition), are challenging to understand as they represent convolutions of two distinct line broadening mechanisms. We model these complicated lineshapes with two critical floating fit parameters: the Gaussian width  $\Gamma_D$  and the Lorentzian width  $\gamma$ . We achieve reliable temperature control through careful apparatus design and a PID (proportional integral derivative) control. Knowing the experimental temperature with confidence allows us to calculate the Doppler effect and the vapor pressure. We input these values as initial guesses of the fitting parameters to the convolution function describing lineshapes. We set good constraints to the Gaussian width  $\Gamma_D$  and gain some insight into the Lorentzian width  $\gamma$  as it depends on temperature as well. Our developed analysis program effectively

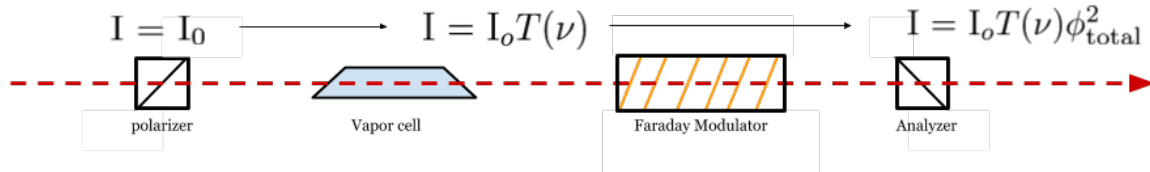


Figure 3: Schematic of our Faraday rotation technique. Two Glan-Thompson prisms are labeled as the polarizer and the analyzer, between which are the lead vapor cell and the Faraday modulator. The transmitted laser intensity after each step is indicated above individual components.  $T(\nu)$  represents the transmission profile through the lead cell.

extracts the remaining Lorentzian width  $\gamma$ , but further tests and improvements are still needed to refine the analysis routine. Figure 4 shows a typical fit for the E2 transition Faraday rotation spectrum.

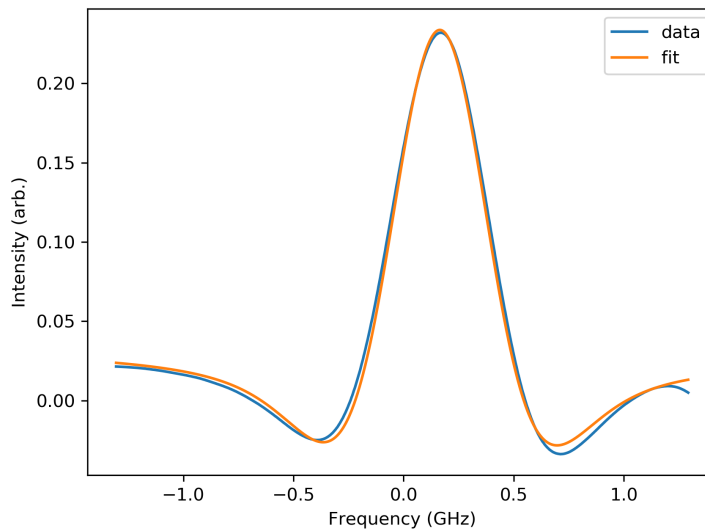


Figure 4: A plot of the raw data along with the fitted curve of a typical Faraday rotation spectrum from the E2 transition. For this particular scan, the lead cell is heated to and held at 960 °C and the current generating magnetic field is set to 4.0 A.

# Acknowledgments

First and foremost, I thank my thesis advisor and the interim president of the college, Professor Tiku Majumder, for his expertise as a physicist and unconditional support as a close mentor. Throughout my undergraduate research journey, Tiku has been an inspirational role model. I would also like to thank our extraordinary Postdoc Daniel Maser for his kind help and patience since he joined our group in the fall. I extend my gratitude to Professor Kevin Jones, the second reader of my thesis, as well as Professor Charlie Doret, whose presence and guidance have made my working experience in the Bronfman basement as pleasant as it could ever be. I also appreciate the technical help from Jason Mativi and Michael Taylor and the overall support from the physics community at Williams.

I thank the Majumder group veterans: Nathaniel Vilas, Eli Hoenig, and Dr. Milinda Rupasinghe, who introduced me to recent research projects, mentored me with great patience, and left the lab in a great shape when they passed the torch to me. Working together with other students in the lab is a constant learning experience and I thank Sauman Cheng, Abdullah Nasir, and Jeremy Thaller for that.

I want to express my deep appreciation for my friends, Kusika instructors, and Chinese music ensemble directors, for enriching my college life. Finally, I am eternally grateful for my parents and family, without whose love and guidance, I would not have become who I am today.

# Contents

|  |           |
|--|-----------|
| <b>Abstract</b>  | <b>i</b>  |
| <b>Executive Summary</b>   | <b>ii</b> |
| <b>Acknowledgments</b>   | <b>vi</b> |
| <b>1 Introduction</b>  | <b>1</b>  |
| 1.1 Motivation . . . . .   | 1         |
| 1.2 Heavy Atoms with Multi-Valence Electrons . . . . .                           | 3         |
| 1.3 Previous Work . . . . .  | 4         |
| 1.3.1 Stark Shift Polarizabilities Measurements in Atomic Beam . . . . .         | 4         |
| 1.3.2 Vapor Cell Spectroscopy and Faraday Rotation Spectroscopy . . . . .        | 5         |
| 1.4 Present Work . . . . .   | 6         |
| 1.5 Outline of This Thesis . . . . .   | 6         |
| <b>2 Atomic Theory</b>   | <b>7</b>  |
| 2.1 Spectroscopy and Spectral Lineshape . . . . .                                | 7         |
| 2.1.1 Absorption Spectroscopy . . . . .  | 7         |
| 2.1.2 Broadened Lineshape . . . . .  | 8         |
| 2.1.3 Voigt Profile . . . . .  | 12        |
| 2.2 Indium Stark Shift Polarizability . . . . .                                  | 13        |
| 2.2.1 Two-Step Excitation in Indium . . . . .                                    | 13        |
| 2.2.2 The Stark Shift Effect . . . . .   | 14        |
| 2.3 Transition Amplitude and Faraday Rotation . . . . .                          | 20        |
| 2.3.1 M1 and E2 Transition in Lead . . . . .                                     | 20        |
| 2.3.2 Faraday Rotation Spectroscopy . . . . .                                    | 22        |
| 2.3.3 Spectra Lineshape and Matrix Elements . . . . .                            | 28        |
| <b>3 Indium Atomic Beam Polarizability Measurements in the 7P Excited States</b> | <b>32</b> |
| 3.1 Experimental Setup and Method . . . . .                                      | 32        |
| 3.1.1 Atom Beam and External Electric Field . . . . .                            | 33        |
| 3.1.2 Vapor Cell . . . . .   | 35        |

|          |   |           |
|----------|---|-----------|
| 3.1.3    | Optical Setup . . . . .   | 36        |
| 3.2      | Data Acquisition . . . . .  | 38        |
| 3.3      | Data Analysis . . . . .   | 41        |
| 3.3.1    | Data Analysis Procedure . . . . .   | 41        |
| 3.3.2    | Systematic Error Considerations . . . . .   | 44        |
| 3.4      | Summary of Results . . . . .  | 48        |
| 3.4.1    | Summary of Indium Polarizability Measurements in 7P Excited States . . . . .  | 48        |
| 3.4.2    | Theory Summary . . . . .  | 49        |
| <b>4</b> | <b>Lead E2 Transition Amplitude Measurements: Apparatus and Experiment Techniques</b>   | <b>52</b> |
| 4.1      | Experimental Setup . . . . .  | 52        |
| 4.1.1    | Lead Vapor Cell in an Oven System . . . . .   | 52        |
| 4.1.2    | Lasers and Optics . . . . .   | 56        |
| 4.2      | Polarimeters and Faraday Rotation Technique . . . . .   | 57        |
| <b>5</b> | <b>Lead E2 Transition Amplitude Measurements: Data Analysis and Preliminary Results</b>   | <b>59</b> |
| 5.1      | Data Acquisition Scheme . . . . .   | 59        |
| 5.2      | Improving Data Analysis Method . . . . .  | 62        |
| 5.2.1    | Analysis Routine Outline . . . . .  | 62        |
| 5.2.2    | Fitting Convolted Lineshape and Extracting Width Parameters . . . . .   | 64        |
| 5.3      | Preliminary E2 Fitting Results and Systematics . . . . .  | 65        |
| <b>6</b> | <b>Future Work</b>  | <b>70</b> |
| 6.1      | Complete the Lead E2 Transition Measurement . . . . .   | 70        |
| 6.1.1    | Improvement in the Heating Element . . . . .  | 70        |
| 6.1.2    | Refinement of the Analysis Program using Data from the M1 Transition . . . . .  | 70        |
| 6.1.3    | Systematic Error Exploration . . . . .  | 71        |
| 6.2      | Future Applications of the Faraday Rotation Technique . . . . .   | 71        |
| 6.2.1    | Hyperfine Structure and Isotope Shift Measurements in $^{207}\text{Pb } 6p^2 \ ^3P_2$ Using Faraday Rotation Spectroscopy . . . . . | 71        |
| 6.2.2    | 368 nm ECDL Construction for Probing a Lead Transition . . . . .  | 72        |
| 6.3      | Stark Shift Polarizability Measurements in Thallium or Lead Atomic Beam . . . . .   | 73        |
| <b>A</b> | <b>Summary of Indium Polarizability Data</b>  | <b>74</b> |
| A.1      | Indium $7P_{1/2}$ data summary . . . . .  | 74        |
| A.2      | Indium $7P_{3/2}$ data summary . . . . .  | 75        |

# List of Figures

|   |  |     |
|---|--|-----|
| 1 | Typical indium absorption spectra depicting both Stark-shifted and unshifted case in each plot. a) Top half shows a typical scan for the $7P_{1/2}$ excited state in the atomic beam and the bottom half shows an unshifted reference absorption signal from an indium vapor cell, with sidebands generated by an electro-optic modulator. Each peak corresponds to one hyperfine level. b) Top half represents the $7P_{3/2}$ state data taken in the low electric field regime, where the scalar component of the polarizability dominates. Bottom half similarly shows the vapor cell reference signal. Due to selection rules, only three hyperfine levels out of four can be accessed through a particular excitation path. c) A typical atomic beam absorption signal of the $7P_{3/2}$ state under a high field, where the tensor polarizability plays a non-negligible role. No vapor cell reference is involved in this regime, for reasons I will explain later. | iii |
| 2 | Summary of our experimental values for indium polarizabilities in the $6S_{1/2}$ , $6P_{1/2}$ , $7P_{1/2}$ , and $7P_{3/2}$ excited states, in comparison with the theoretical calculations using two distinct models for each state. The yellow data points show polarizability values calculated using the CC (coupled-cluster) model, a model based on a single valence system, while the green data points are predictions from the CI+all-order (configuration-interaction + all-order) method, a trivalent-electron approach. The middle purple data point in each plot is our experimental result.  | iv  |
| 3 | Schematic of our Faraday rotation technique. Two Glan-Thompson prisms are labeled as the polarizer and the analyzer, between which are the lead vapor cell and the Faraday modulator. The transmitted laser intensity after each step is indicated above individual components. $T(\nu)$ represents the transmission profile through the lead cell.  | v   |
| 4 | A plot of the raw data along with the fitted curve of a typical Faraday rotation spectrum from the E2 transition. For this particular scan, the lead cell is heated to and held at 960 °C and the current generating magnetic field is set to 4.0 A.   | v   |

|     |  |    |
|-----|--|----|
| 1.1 | Level structure of $^{115}\text{In}$ states relevant to the present measurement. Our two-step spectroscopic scheme requires that we overlap 410 nm and 690 (685) nm lasers through an atom source to drive the ‘first-step’ $5P_{1/2} \rightarrow 6S_{1/2}$ transition and the ‘second-step’ $6S_{1/2} \rightarrow 7P_{1/2 (3/2)}$ transitions. . . . .  | 4  |
| 1.2 | Level structure of $^{208}\text{Pb}$ states relevant to the present measurement, namely the triplet $6s^26p^2$ states. The M1 transition is at 1279 nm and the E2 transition is at 940 nm, both in the infrared region. . . . .  | 5  |
| 2.1 | Energy structure of $^{115}\text{In}$ states relevant to the two-step excitation paths. The dotted energy levels represent the Stark shifted energy levels under an external electric field (not to scale). $\delta$ ’s label the Stark shift associated with each state.  | 14 |
| 2.2 | The Stark shift in indium $7P_{3/2}$ excited states corresponding to applied electric-field-squared. The dotted line is located at $9 (\text{kV}/\text{cm})^2$ , representing our decided cut-off field strength for the regime in which tensor polarizability is negligible. At higher fields, tensor polarizability begins to contribute significantly, causing energy splittings within each hyperfine state. . . . .   | 18 |
| 2.3 | Energy eigenvalue structure under an applied electric field for all hyperfine sub-levels of the indium $7P_{3/2}$ state. Here, the indicated energy shift only results from tensor polarizability, as we exclude the dominant scalar polarizability ( $-\frac{1}{2}\alpha_0\mathcal{E}^2$ , shared by all $ F, m_F\rangle$ levels). Each color represents one hyperfine level. . . . .   | 19 |
| 2.4 | A qualitative representation of the lineshapes associated with the real and imaginary parts of the complex refractive index. It is obvious that $\mathbf{Re}[\tilde{n}]$ corresponds to a dispersive shape, and $\mathbf{Im}[\tilde{n}]$ to a Lorentzian shape. . . . .  | 25 |
| 2.5 | Zeeman splittings in the energy states relevant to current experiment. Every $\delta\nu$ represents the frequency differences between $m_j$ states in a given energy level. RHC ( $\sigma_+$ ) and LHC ( $\sigma_-$ ) excite atoms to different $m_j$ sublevels, leading to the index of refraction’s polarization dependence. . . . .   | 26 |
| 2.6 | A qualitative representation of the Zeeman-shifted dispersive and Lorentzian curves, associated with the real and imaginary parts of the complex refractive index. The unshifted curves first shown in Figure 2.4 are replotted as dashed lines. . . . .   | 27 |
| 2.7 | The Faraday Lineshapes . . . . .   | 29 |
| 3.1 | Simplified schematic of the optical setup used in indium Stark shift measurements. Here PD refers to a photodetector, EOM to an electro-optic modulator, and ECDL to an external cavity diode laser. Two AOMs (acousto-optic modulators) are inserted in the path of the blue laser beam component which is incident on the atomic beam apparatus in order to maintain resonance for the first-step transition as the electric field, and therefore the resonance frequency, is changed in the interaction region. . . . . | 33 |

|     |   |    |
|-----|---|----|
| 3.2 | The experimental configuration in the interaction region in the atomic beam unit. The two overlapping laser beams (counter-propagating) are orthogonal to the atomic beam in a horizontal plane. The parallel plates provides a vertical static electric field. . . . .   | 35 |
| 3.3 | A qualitative representation of the raw first-step absorption ( $5P_{1/2} \rightarrow 6S_{1/2}$ ) curve and the RF demodulated derivative curve, which we utilize to lock our 410 nm laser. . . . .   | 37 |
| 3.4 | The AOM setup for correcting the Stark-shifted first-step transition resonant frequency. . . . .  | 38 |
| 3.5 | Atomic beam spectra for the case of the ( $F' = 4$ ) $\rightarrow$ ( $F'' = 4, 5$ ) transitions of the 690 nm $6S_{1/2} \rightarrow 7P_{1/2}$ line. The field-off spectrum (red dashed line) and the spectrum with a 3 kV/cm electric field applied (blue solid line) are shown. Displayed below is the corresponding (field-free) vapor cell spectrum, including 1000 MHz FM sidebands, used for frequency referencing and calibration. The small spectral features on the shoulders of the large vapor cell peaks are due to the $^{113}\text{In}$ isotope (4% abundance) which we account for in our line shape analysis. As noted in the text, the data shown here represent the average of thirty consecutive field off/field on scan pairs. . . . . | 40 |
| 3.6 | Energy eigenvalue structure under applied electric field for all hyperfine sub-levels of the indium $7P_{3/2}$ state. Here, we again have subtracted out the large scalar shift, $-\frac{1}{2}\alpha_0\mathcal{E}^2$ , shared by all $ F, m_F\rangle$ levels for clarity as in Figure 2.3. However, we plot the energy shift against electric field strength instead of electric-field-square, since we physically control the field itself. . . . .  | 41 |
| 3.7 | Atomic beam spectra for the case of the a) ( $F' = 4$ ) $\rightarrow$ ( $F'' = 3, 4, 5$ ) transitions and b) ( $F' = 5$ ) $\rightarrow$ ( $F'' = 4, 5, 6$ ) of the 685 nm $6S_{1/2} \rightarrow 7P_{3/2}$ line. The field off spectra (red dashed line) as well as the spectra with a 1.5 kV/cm electric field applied (blue solid line) are shown. Displayed on the bottom of each plot is the corresponding (field-free) vapor cell spectrum, including 1000 MHz FM sidebands, used for frequency referencing and calibration. As in the previous figure, the data shown here represent the average of thirty consecutive field off / field on scan pairs. . . . .  | 42 |
| 3.8 | For the 685 nm $6S_{1/2} \rightarrow 7P_{3/2}$ transition, spectra are shown for the case of $E = 15$ kV/cm and 16 kV/cm, showing a roughly 1 GHz overall Stark shift. For each electric field value, we have averaged a series of scans taken consecutively over a period of 10 minutes for display purposes. Referring to Fig. 3.6, one can see experimental evidence supporting our numerical model, where two relatively sharp experimental peaks are accompanied by a broad composite feature at the higher frequency end of both of the scans shown. . . . .  | 44 |

|      |  |    |
|------|--|----|
| 3.9  | The plot shows four $k_0$ results for the indium $7P_{3/2}$ state. Each data point represent the weighted average value of a subset of data under the denoted experimental conditions. Here we check that there is no systematic difference in results between the up/down laser scanning direction, nor between the ‘field-off’ / ‘field-on’ sequence when we collect data. . . . .   | 45 |
| 3.10 | a) For the 690 nm $6S - 7P_{1/2}$ transition, we plot the Stark shift constant derived from roughly 400 field-off / field-on scan pairs taken with $E = 3$ kV/cm. A Gaussian curve is laid over the data for display purposes. Central values and standard errors from such analyses complement a weighted average analysis approach to arrive at final statistical averages and uncertainties. b) All $7P_{1/2}$ Stark shift data, with Stark shift constant plotted versus electric field to explore potential field-dependent systematic errors. An analysis of these data shows the absence of a statistically resolved correlation. . . . .   | 46 |
| 3.11 | a) For the case of all data collected for the transition path $6S_{1/2}(F' = 5)$ to $7P_{3/2}(F'' = 4, 5, 6)$ , we average the results of the Stark shift constant for each upper-level hyperfine state, and the resulting average Stark shift constants at each electric field value are plotted. Given that the tensor polarizability is expected to contribute at higher fields, it is notable that over the 1 to 3 kV/cm range shown here we see no statistically significant variation in the measured polarizability. b) At the highest field used, where we expect some hyperfine peak broadening and possible peak asymmetry, we investigate the dependence of the measured Stark shift constant on hyperfine level, now including data taken for each of the four $7P_{3/2}$ -state sub levels. . . . . | 47 |
| 3.12 | Summary of our experimental values for indium polarizabilities in the $6S_{1/2}$ , $6P_{1/2}$ , $7P_{1/2}$ , and $7P_{3/2}$ excited states, in comparison with the theoretical calculations using two distinct models for each state. The yellow data points show polarizability values calculated using the CC model, while the green data points are predictions from the CI+all-order approach. The middle purple data point in each plot is our experimental result. . . . .   | 50 |
| 4.1  | The experimental layout of the lead transition amplitudes measurements. . .  | 53 |
| 4.2  | A cross-sectional view of the oven system for the lead transition amplitude measurement experiment. . . . .  | 54 |
| 4.3  | Oven setup schematics viewed from the top. The spatial configuration of the heaters and the cell is illustrated. . . . .   | 54 |
| 4.4  | Typical temperature data from the two thermocouples over the course of a day starting from room temperature. On this particular day, the first target temperature in PID program is set to be $900^\circ\text{C}$ (represented by the first converging range around 10,000 seconds), and then we lower the target temperature to $870^\circ\text{C}$ to take different data sets at a lower temperature (represented by the second converging phase after 22,000 seconds). . . . .   | 55 |

|     |  |    |
|-----|--|----|
| 4.5 | Schematic of our Faraday rotation technique. Two Glan-Thompson prisms are labeled as the polarizer and the analyzer, between which are the lead vapor cell and the Faraday modulator. The transmitted laser intensity after each step is indicated above individual components. $T(\nu)$ represents the transmission profile through the lead cell. . . . .  | 57 |
| 5.1 | Fitted 1279 nm Faraday Spectra . . . . .   | 61 |
| 5.2 | Fitted 939 nm Faraday Spectra . . . . .  | 61 |
| 5.3 | Top panel shows a raw Fabry-Perot transmission signal from one of the four traces taken. The middle panel fits to each Fabry-Perot peak overlaid with each peak, and the bottom panel plots the differences between each peak before (blue points) and after (orange points) linearization. . . . .  | 64 |
| 5.4 | The top panel shows a typical 1f lock-in signal (Faraday rotation spectrum) of the E2 transition. The middle panel shows the 2f signal (transmission) and we suspect the slope is a result of birefringence of optics in the apparatus and laser power drift. We can further investigate this effect by altering optical configurations in future scans. The bottom panel shows the fitted curve along with the input initial guesses. . . . . | 66 |
| 5.5 | a) shows the extracted Doppler widths plot against temperature. b) the relationship between the expected Doppler width and temperature (Equation 2.6). They agree in the general shape up to a scaling factor. . . . .   | 67 |
| 5.6 | a) shows the extracted Lorentzian widths plot against temperature. b) the general relationship (Equation 2.11) between the collisional width and temperature, up to a scaling factor. . . . .  | 67 |
| 5.7 | The measured spectral amplitudes plotted against the current driving the magnetic field coils. The linear relationship indicates that the observed peak amplitude simply scales with the field strength as expected from theory. . . .   | 68 |
| 5.8 | The fitted Lorentzian widths plotted against the current driving the magnetic field coils. . . . .   | 69 |
| 6.1 | Low-lying states for $^{208}\text{Pb}$ . The fractional populations of lead atoms (determined by thermal excitation) at the two ground states are shown for a temperature of $1000^\circ\text{C}$ . The indicated transition path requires the driving laser to be around 368 nm. . . . .  | 72 |

# Chapter 1

## Introduction

### 1.1 Motivation

The Standard Model (SM) successfully predicts the existence of all detected particles and the laws of particle interactions. Yet, the SM remains incomplete as it fails to explain some observable phenomena, such as dark matter and dark energy. The ongoing search for new particles and forces beyond the SM has been primarily taking place in high-energy particle colliders, but this frontier of fundamental physics could also be probed via tabletop-scale experiments in atomic systems. For instance, parity nonconservation (PNC) could be probed by observing PNC effects deviating from the ordinary quantum mechanic predictions on the atomic scale. This alternative approach requires precise measurements of atomic properties and refined theoretical models of atoms that separate the more complex effects from basic quantum mechanics. Moreover, heavy atoms are preferred when modeling high energy processes in low-energy atomic systems. Heavier atoms exhibit tiny deviations from SM more drastically because these effects often scale with the atomic number. On the other hand, heavy atoms, particularly those with multiple valence electrons, have rather complicated electron configurations and modeling such systems tends to be challenging. Improvement in the wavefunction calculations of these complicated atomic systems is necessary for searching physics beyond the SM. The Majumder group focuses on measurements of particular atomic properties, which serve to test existing wavefunction predictions and inspire further development in modeling complex atomic systems. In other words, our high-precision measurements of atomic properties in heavy atoms have direct bearing on future experiments searching PNC or other quantum phenomena beyond the SM.

One general way to study atomic systems is to conduct optical experiments, exciting resonant transitions between quantized energy states and observing the atoms' behavior in respond to external perturbations, such as an electric field or a magnetic field (Ref. [1]). This thesis explores two atomic systems under a perturbing electric or magnetic field using laser

spectroscopy technique in two distinct experiments:

- precise measurements of the Stark shift (the atomic response to an external electric field) polarizabilities in indium  $7P$  excited states;
- precise measurements of the electric quadrupole amplitude within the  $6p^2 \ ^3P_0 \rightarrow \ ^3P_2$  transition in lead using the Faraday rotation technique (enabled by applying an external magnetic field).

Measurements of these properties, however, cannot be directly linked to just the fundamental physics that we aim to explore, but are inseparable from the specific atom we choose as a testing site. Take the PNC measurements performed in Ref. [2] as an example. The goal of this PNC experiment is to measure the optical rotation  $\epsilon_w$ , which can be expressed as the product of two quantities,

$$\epsilon_w = Q_w \mathcal{C}(Z), \quad (1.1)$$

where  $Q_w$  represents the so-called weak charge from electroweak theory, or in a broader sense, an interesting particle physical property, and  $\mathcal{C}(Z)$  represents the relationship between the fundamental physics and the specific atom used to conduct the measurements. Hence, understanding  $\mathcal{C}(Z)$  in a particular atom with adequate precision becomes essential in order to determine the value of  $Q_w$ . It turns out that  $Q_w$  tends to be extremely small, making its effect rather challenging to detect. Therefore, to extract a meaningful value of  $Q_w$ , it demands not only the precise measurements of the observables, but also accurate theoretical calculations of  $\mathcal{C}(Z)$  specific to atoms. Such accurate understanding of atomic properties comes from both high-precision theoretical predictions and high-precision experimental measurements, and our group contributes to the latter.

There is still much we do not know about atoms, over a century after when the atomic structure was first imagined by Thomson’s “plum pudding” model. As a matter of fact, only hydrogen, the simplest atom in nature, has analytical wavefunction solutions. For atomic systems beyond the hydrogen atom, we only have approximate models. A mere understanding of this one-electron system certainly cannot satisfy our curiosity, nor assists to push the frontier of atomic physics. Constant theoretical effort in modeling atomic phenomena and studying physics beyond the SM goes hand-in-hand with experiments that probe fundamental atomic properties and serve as benchmarks to atomic theories. By conducting laser spectroscopic experiments on heavy atoms to measure quantities that test and illuminate the wavefunction calculations of particular atoms, we contribute to the refinement of theoretical atomic models. For multi-valence systems, like the trivalent indium atom, we consider two state-of-the-art atomic theory approaches to calculating valence electron wavefunctions. In particular, our theorist colleague, Professor Marianna Safronova, has developed two theoretical calculation methods: a coupled-cluster approach (CC) and a configuration-interaction + all-order method (CI+all), and recently published calculations of matrix elements in indium and lead (see Ref. [3] and [4]). These theoretical predictions motivate us to carry out experiments as a test and future guide to these two models.

## 1.2 Heavy Atoms with Multi-Valence Electrons

In the past, the specimens of our fundamental atomic property testing experiments have involved heavy Group IIIA atoms, namely, thallium and indium. Our loyal focus on this column of elements in the periodic table is caused by their intriguing multi-valence electron configuration. For such a multi-valence electron system, its theoretical model is both sufficiently complex so that the measurement of their fundamental properties illuminates our understanding of the theoretical model, and tractable enough so that the model yields accurate predictions. Further, heavy atoms, as opposed to lighter ones in the same group, are experimentally favored since many of the particle physics properties mentioned above scale with  $Z^3$ . Thus, using heavy atoms as our testbeds amplifies physical effects for measurement purposes.

The first experiment described in this thesis uses indium as its testbed. Indium has atomic number  $Z = 49$ . For our experiment, we focus on the more abundant indium isotope,  $^{115}\text{In}$ , whose natural abundance is  $\sim 96\%$ . The tiny peaks from the other isotope,  $^{113}\text{In}$ , are either spectroscopically unresolvable or clearly separated, causing no distortion in the spectral peak shape of  $^{115}\text{In}$ .  $^{115}\text{In}$  has a nuclear spin  $I = 9/2$ . The spin-spin interaction between the nuclei and electron further splits each  $J$  level (fine structure) into hyperfine structures. For states with  $J = 1/2$ , there are two hyperfine levels ( $F = 4$  and  $F = 5$ ), while for states with  $J = 3/2$ , there are four hyperfine levels ( $F = 3, 4, 5, 6$ ). The hyperfine splittings in the  $5P_{1/2}$  state and  $6S_{1/2}$  state are 11.4 GHz and 8.4 GHz respectively, and the hyperfine structures in the  $7P$  states were precisely measured by our group in 2016 (see Ref. [5] Appendix E for details). The energy levels relevant to this experiment along with their hyperfine structures are shown in Figure 1.1. In this experiment, we measure the Stark shift, which will be introduced in chapter 2, of indium  $7P_{1/2}$  and  $7P_{3/2}$  states.<sup>1</sup>

The second experiment studies transitions in lead, a heavy atom with four valence electrons. Recent theoretical wavefunction calculations in lead (see Ref. [4]) motivate us to conduct atomic property measurements in lead, providing experimental parameters of quantum mechanical properties for further refinement of the theory. Lead has atomic number  $Z = 82$  and four naturally occurring isotopes. Our experiment uses nearly pure  $^{208}\text{Pb}$  to measure transition amplitudes, as this even isotope lacks hyperfine structures and simplifies the transmission spectrum. We study two transitions within the triplet  $6P$  state. Due to selection rules, an electric dipole transition is forbidden. The two transitions of interest ( $6s^26p^2\ ^3P_0 \rightarrow\ ^3P_1$  and  $6s^26p^2\ ^3P_0 \rightarrow\ ^3P_2$ ) are driven by magnetic dipole (M1) moment and electric quadrupole (E2) moment respectively, as the energy diagram in Figure 1.2 indicates.

---

<sup>1</sup>All the indium states in this thesis are  $6s^2nl_J$ , but we abbreviate the notation to  $nl_J$  since two valence electrons out of three are always considered to be paired.

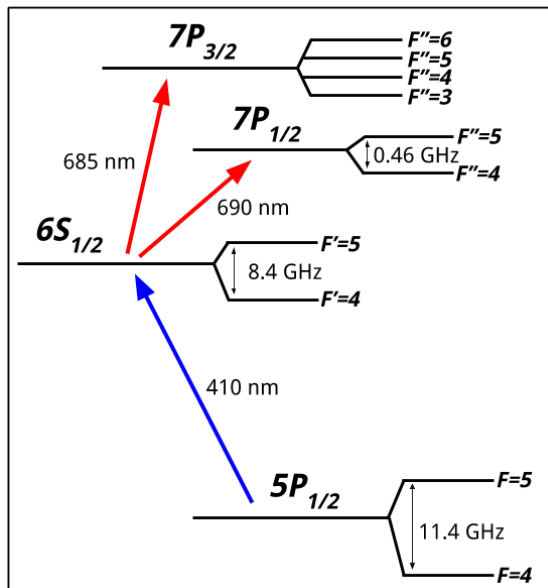


Figure 1.1: Level structure of  $^{115}\text{In}$  states relevant to the present measurement. Our two-step spectroscopic scheme requires that we overlap 410 nm and 690 (685) nm lasers through an atom source to drive the ‘first-step’  $5P_{1/2} \rightarrow 6S_{1/2}$  transition and the ‘second-step’  $6S_{1/2} \rightarrow 7P_{1/2(3/2)}$  transitions.

### 1.3 Previous Work

The Majumder group has performed a series of precise measurements of hyperfine structures, isotope shifts, Stark shift polarizabilities in several excited states of thallium and indium. Recently, we initiated work in lead. Past projects not only lend us knowledge and experiences working with these multi-valence electron systems, but more importantly, have driven us to develop transferrable techniques that can be adapted to probing new problems. The two experiments described in this thesis stem directly from Nathaniel Vilas’s and Eli Hoenig’s thesis work, Ref. [5] and [6], but benefit from tools engineered for the atomic beam system, vapor cell spectroscopy, and Faraday rotation spectroscopy throughout two decades of research in our lab.

#### 1.3.1 Stark Shift Polarizabilities Measurements in Atomic Beam

The Majumder group has conducted a series of experiments measuring the Stark shift polarizabilities in thallium and indium. The indium  $7P$  states polarizability work described in this thesis wraps up a line of Stark shift measurements in indium atomic beam. Previous work completed measuring the Stark effect in indium  $6S_{1/2}$  and  $6P_{1/2}$  states, and started to look at  $7P_{1/2}$  as well as  $7P_{3/2}$  excited states (see Ref. [7], [8], and [5]). All of these

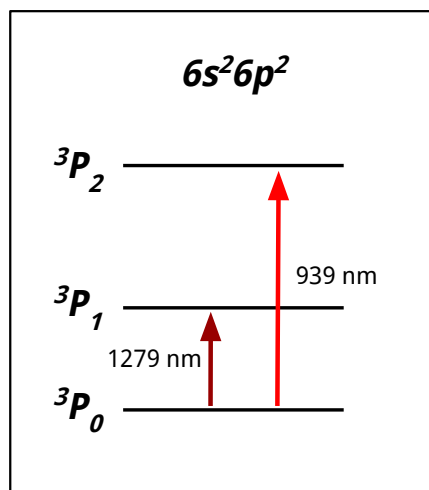


Figure 1.2: Level structure of  $^{208}\text{Pb}$  states relevant to the present measurement, namely the triplet  $6s^2 6p^2$  states. The M1 transition is at 1279 nm and the E2 transition is at 940 nm, both in the infrared region.

measurements are conducted in an atomic beam system, in which we generate a beam of indium atoms, direct the beam to interact with laser radiation under a controlled external electric field, and collect the post-interaction absorption spectra from which we extract the Stark shift. Nathaniel Vilas's thesis [5] is particularly relevant for our recent work, as it lays out the theoretical framework of a many-level system to treat the tensor polarizability of the  $7P_{3/2}$  state.

### 1.3.2 Vapor Cell Spectroscopy and Faraday Rotation Spectroscopy

Our group has abundant experiences working with vapor cell systems. From past vapor cell spectroscopic experiments, we have accumulated a wealth of experiences in experimental design and spectrum fitting. Our Faraday rotation technique was first used in 1999 to probe tiny Faraday rotation signal in a thallium M1/E2 transition. Last year, our group shifted the longstanding focus on trivalent electron systems to lead, an element with four valence electrons. The Faraday rotation setup was reassembled for studying an E2 transition in lead as presented in Eli Hoenig's thesis work [6]. In that thesis, the hyperfine structure in lead was measured with great precision and the preliminary work towards a precise measurement of an E2 transition was described.

## 1.4 Present Work

The indium polarizability measurement portion of this thesis further studies the  $7P$  excited states, especially the more complicated  $7P_{3/2}$  case. Extending and modifying from previous work, we continue to improve our experimental techniques and seek new approaches to data analysis, though on the grand scale, the experimental design and method are the same as previous experiments. We explore various systematics by acquiring the Stark shift spectra under varying circumstances, yielding a precise final result of Stark shift polarizabilities for the  $7P$  excited states in indium. This project was completed by the end of 2017 and published together with theoretical colleagues, see Ref. [9].

The lead transition amplitude measurement is an extension from the groundwork laid out in Ref. [6]. We aim to determine the amplitude ratio of two transitions: the  $6s^26p^2\ ^3P_0 \rightarrow\ ^3P_1$  magnetic dipole (M1) transition and the  $6s^26p^2\ ^3P_0 \rightarrow\ ^3P_2$  electric quadrupole (E2) transition in  $^{208}\text{Pb}$ . Since the M1 transition amplitude is known (it is a strong enough transition to be measured via direct absorption), we could extract the amplitude of the E2 transition once we have the ratio. Our goal is to achieve a precision of below 2% error for the E2 transition, which has never been measured. This thesis presents a work-in-progress of this project. I will underline the experimental strategies and analysis developments, as well as present preliminary results.

## 1.5 Outline of This Thesis

This thesis describes the ongoing two projects in the Majumder lab: measurements of indium Stark shift polarizability in the  $7P$  states and measurements of lead E2 transition amplitude. Chapter 2 introduces relevant concepts of atomic structure and properties, and highlights theoretical methods used to model and understand the structure. This theory chapter first discusses basic ideas of spectroscopy and spectral lineshapes, common background knowledge for both experiments. It then moves on to theory particular to each experiment in detail, such as the Stark effect for the indium polarizability measurements and the theory behind the Faraday rotation technique for the lead experiment. Chapter 3 is a thorough report of the completed indium experiment. It covers the experimental setup and method, data acquisition, data analysis, and finally presents the summary of results. Chapter 4 changes the direction and describes the experimental setup for the lead experiment. In chapter 5, we continue to discuss the data acquisition and analysis approach to the lead E2 transition amplitude measurement. Finally, chapter 6 addresses the remaining work to be completed in the lead experiment and propose future projects that will follow from this year's research work.

# Chapter 2

## Atomic Theory

### 2.1 Spectroscopy and Spectral Lineshape

#### 2.1.1 Absorption Spectroscopy

Despite drastic differences between the two experiments described in this thesis, they share the same underlying methodology: laser spectroscopy. This essential concept has been our group's main tool to probe various fundamental atomic properties, such as hyperfine structures, isotope shifts, and polarizabilities. Spectroscopy assists us to “see” on the atomic scale via studying the interactions between controlled electromagnetic (EM) radiation and atoms (or any matter) of interest. This thesis describes laser spectroscopy in an indium vapor cell as well as an atomic beam in order to measure the Stark shift, and in a lead vapor cell along with the Faraday rotation technique to extract an electric quadrupole transition amplitude.

Both experiments make use of direct absorption spectroscopy. When the EM wave resonates with the atoms of interest, both are perturbed and we can infer the energy changes of the atoms from observing the transmitted EM wave after the interaction, which mirrors the perturbations of the atomic system. More quantitatively, if one directs a laser beam at frequency  $\omega$  and of intensity  $I$  to interact with a sample of atoms of length  $dz$ , the laser intensity after the beam passing through the sample will decrease by:

$$dI = -A(\omega)I dz, \tag{2.1}$$

where  $A(\omega)$  represents the probability of atoms absorbing the laser light as a function of frequency. By convention,  $A(\omega) = \alpha P(\omega)$ , in which  $\alpha$  is the so-called optical depth of the atomic sample and  $P(\omega)$  is the normalized probability function. The optical depth  $\alpha$  of a

sample characterizes how strong the resonant absorption is in the particular sample. We can derive the transmitted intensity by integration:

$$I(\omega, z) = I_0 e^{-\alpha P(\omega)}. \quad (2.2)$$

Then, through measuring the transmitted intensity  $I(\omega, z)$ , we can extract information about the atomic absorption probability  $P(\omega)$ , from which we could locate the transition frequency and infer atomic properties listed above.

### 2.1.2 Broadened Lineshape

Theoretically, every transition has an intrinsic resonant frequency corresponding to its energy level difference, meaning a single wavelength of light and no other would induce the transition. In reality, however, an observed transmission spectral peak never strictly has the features of a delta function at the atomic resonance. In other words, the spectral lineshape is broadened. Quantum mechanical effects as well as experimental properties both influence the range over which atoms respond to light, resulting in such a broadened absorption profile. The nonzero linewidth in our case typically spreads over many MHz or a few GHz about the resonance. Understanding various mechanisms causing the lineshape broadening is essential for the experimental design and data analysis process. Here, we outline a few important mechanisms accountable for the broadened spectral lineshape in our two experiments.

#### Doppler Broadening

For an absorption spectroscopy experiment, especially in thermal atomic vapors, Doppler broadening often dominates among all line broadening mechanisms. At high temperatures, atoms confined in a vapor cell move with large velocity in random directions. The observed optical transitions are related to Doppler shifts of the laser light “seen” by these moving atoms. Considering radiation in the  $z$ -direction and for atoms moving along  $\hat{z}$ , the observed frequency of the emitted radiation is  $f \approx f_0(1 + \frac{v_z}{c})$ , where  $f_0$  is the unshifted frequency. The Maxwell-Boltzmann statistics characterize the atoms’ velocity distribution, following which the number density  $n(v_z)$  of atoms with velocity between  $v_z$  and  $v_z + dv_z$  is

$$n(v_z)dv_z = n_{tot} \sqrt{\frac{m}{2\pi k_B T}} e^{-mv_z^2/(2k_B T)} dv_z, \quad (2.3)$$

where  $n_{tot}$  is the total density,  $k_B$  is the Boltzmann constant,  $T$  is the atomic temperature, and  $m$  is mass of the atom. In frequency space, letting  $f_0$  be the transition resonance, the number density between frequency  $f$  and  $f + df$  can be written as:

$$n(f)df = n_{tot} \frac{c}{f_0} \sqrt{\frac{m}{2\pi k_B T}} e^{-mc^2(f-f_0)^2/(2k_B T f_0^2)} df. \quad (2.4)$$

Then, the transmission spectrum is a Gaussian profile (we effectively derive the form of  $P(\omega)$  in Equation 2.2):

$$I(\Delta) = I_0 e^{-\left(\frac{\Delta}{\Gamma_D}\right)^2}, \quad (2.5)$$

where  $\Delta$  is the detuning from the resonance,  $\Delta = f - f_0$ , and  $\Gamma_D$  is the Doppler width (FWHM),

$$\Gamma_D = \frac{f_0}{c} \sqrt{\frac{8k_B T \ln 2}{m}}. \quad (2.6)$$

Doppler broadening has a salient effect in vapor cells, as the heated atoms move rapidly in randomized directions. In our indium experiment, the temperature of the indium vapor cell is  $T \sim 750^\circ\text{C}$ , leading to a Doppler width  $\Gamma_D \approx 1.6$  GHz for the first-step transition. In the lead experiment, the lead vapor cell is heated to an even higher temperature  $T \sim 950^\circ\text{C}$ , resulting in Doppler widths  $\Gamma_D \approx 400$  MHz for the M1 transition and  $\Gamma_D \approx 544$  MHz for the E2 transition. In the case of an atomic beam, Doppler broadening has a less dominant effect. Unlike most broadening mechanisms relevant to this thesis that will be introduced below, Doppler broadening is an inhomogeneous broadening mechanism, meaning it does not affect individual atom in the sample uniformly.

## Lifetime Broadening

It turns out to be unrealistic for an atom to occupy an excited state indefinitely. Instead, an excited atom decays spontaneously to its ground state or a more stable level with a characteristic time  $\tau$ . The Heisenberg uncertainty principle indicates an limit on its possible energy:

$$\Delta E \Delta t = \Delta E \tau \cong \hbar. \quad (2.7)$$

This means laser radiation detuned from the resonance by an amount within the frequency range  $\pm\omega = \Delta E/\hbar$  still drives the transition. Hence, the broadened width can be written as:

$$\gamma = \frac{\Delta\omega}{2\pi} = \frac{1}{2\pi\tau}. \quad (2.8)$$

From the width of lifetime broadening, we can derive the associated lineshape and natural linewidth caused by spontaneous radiation via modeling this system as a damped classical harmonic oscillator (a step-by-step derivation can be found in Ref. [10]). It turns out that the lineshape follows a Lorentzian profile, with a FWHM of exactly  $\gamma$  in Equation 2.8.

For our indium polarizability experiment, we adopt a two-step excitation scheme. For the second step transition between two excited states, the overall linewidth is the sum of the two natural linewidths associated with each excited state. According to Ref. [3], the relevant states in indium have lifetimes  $\tau_{6S_{1/2}} \sim 7$  ns,  $\tau_{7P_{1/2}} \sim 219$  ns, and  $\tau_{7P_{3/2}} \sim 192$  ns. The expected natural linewidth, then, is dominated by  $\tau_{6S_{1/2}}$ , which corresponds to a width:  $\gamma \approx 23.5$  MHz. For the case of the lead, we are measuring a magnetic dipole (M1) and an electric quadrupole (E2) transition, both of whose strength are much smaller than their

electric dipole (E1) counterparts. Consulting Eli Hoenig's thesis [6], we draw the conclusion that the natural linewidth is on the magnitude of a few hundred Hz, totally negligible comparing with the effects of other types of broadening.

### Power Broadening

The laser intensity determines how strongly the light field perturbs the atomic properties, if it does perturb at all. Following the discussion in Ref. [11], we define the saturation parameter, a crucial measure of whether or not the light field strongly perturbs the population of atomic states, to be

$$\kappa = \frac{\text{excitation rate}}{\text{relaxation rate}}. \quad (2.9)$$

The exact functional form of  $\kappa$  (some literatures use symbol S for saturation parameter) is system specific, depending on the atomic level structure, the relaxation mechanism and other factors. For the indium E1 transitions of our interest, the laser intensity is large enough to cause significant Rabi oscillations. The saturated excited states introduce further broadening in addition to the natural linewidth, producing a Lorentzian profile with increased linewidth

$$\gamma = \gamma_0 \sqrt{1 + \kappa}, \quad (2.10)$$

where  $\gamma_0$  is the natural linewidth in Equation 2.8, when we only take lifetime broadening into account. For the indium experiment, based on calculations of the dipole matrix elements in indium in Ref. [3] along with measured laser power and beam size, we estimate the power broadened linewidths to be  $\sim 25$  MHz for the 410 nm laser and  $\sim 5$  MHz for the 685 nm or 690 nm laser. For the lead experiment, on the other hand, the M1 and E2 transitions we examine are extremely weak. Thus, neither transition in lead involves the possibility of saturation, dismissing power broadening as a contributor to the spectral linewidths. For a more detailed explanation of saturation and power broadening, see Ref. [10] and [11].

### Pressure Broadening

Collisions among atoms are another important contributor to broadened spectral lineshapes.<sup>1</sup> By collision, we mean the mutual interactions between atoms within a characteristic radius  $R_C$ , inducing energy shifts in collision partners as their electron configurations are perturbed. The collision-induced line profile depends on the interaction potential between two atoms, but for our purpose, we only consider elastic collisions which do not change the amplitude of transition probability but add a phase shift. We approximate the collision-related lineshape

---

<sup>1</sup>There are situations in which collisions lead to line *narrowing* instead, known as Dicke narrowing. For our cases, only collision-induced broadening is relevant.

| Broadening Mechanism    | FWHM              |                    |                 |
|-------------------------|-------------------|--------------------|-----------------|
|                         | Indium Vapor Cell | Indium Atomic Beam | Lead Vapor Cell |
| Lifetime Broadening     | 23.5 MHz          | 23.5 MHz           | 200 Hz          |
| Doppler Broadening      | 1.6 GHz           | -                  | ~500 MHz        |
| Power Broadening        | 30 MHz            | 30 MHz             | -               |
| Pressure Broadening     | 10 kHz            | -                  | 75 MHz          |
| Transit-Time Broadening | ~500 Hz           | ~500 Hz            | 70 kHz          |
| Laser Linewidth         | 2 MHz             | 2 MHz              | 2 MHz           |

Table 2.1: Summary of broadened linewidths associated with relevant broadening mechanisms for three atomic systems we study in this thesis.

to be Lorentzian, with a FWHM (for more details, see Ref. [10]):

$$\gamma_P = 4p_v\sigma_b\sqrt{\frac{2}{2\pi\mu k_B T}}, \quad (2.11)$$

where  $p_v$  is the vapor pressure,  $\mu$  is the reduced mass for the collision pairs, and  $\sigma_b$  is the collisional cross section. Because of  $\gamma_P$ 's apparent dependence on the vapor pressure, this phenomenon is referred to as pressure broadening. In a vapor cell, this mechanism plays a crucial role setting limits for the spectral lineshape. For our lead experiment, we heat up the lead vapor cell to  $\sim 950^\circ\text{C}$ , yielding  $\sim 1$  Torr of vapor pressure in the lead cell. We approximate the pressure broadened linewidth to be roughly 75 MHz [6]. In an atomic beam system, the collisional cross section is extremely small and we could neglect its effect as lifetime broadening and power broadening dominate.

### Other Broadening Mechanisms and Summary

The above listed broadening mechanisms are by no means exhaustive but account for the majority of the broadened linewidth we observe. Table 2.1 summarizes various line broadening mechanisms and their contributions to atomic systems relevant to this thesis. It is worth noting that many values quoted in the table indicate the estimated order of magnitude rather than precise measurements, as we vary laser power, operational temperature and other parameters to provide different experiment conditions as a test of systematic errors. Yet, these estimated widths do offer an insight into dominant linewidth contributors for each atomic system. The next subsection discusses the line shapes in the context of each experiment and the fitting strategy we undertake in data analysis.

### 2.1.3 Voigt Profile

The absorption spectra of our atomic samples are broadened as a result of the listed mechanisms. The homogeneous broadening mechanisms, dominated by lifetime broadening or collisional broadening, yield a Lorentzian profile, while the inhomogeneous broadening source, Doppler broadening, follows a Gaussian shape as a consequence of the Maxwell-Boltzmann distribution. Quantum mechanically, every single atom has a Lorentzian-shape response about some center frequency. Statistical mechanics suggests that there exists an ensemble of atoms with different velocities, distributed in a Gaussian shape at a given temperature. Our sample in the vapor cell, then, consists of individual lead atom with a Lorentzian absorption profile centered at a particular Doppler-shifted frequency, dictated by its velocity with respect to the observer in the lab frame. Therefore, we need to consider the convolution of Gaussian and Lorentzian functions, the so-called Voigt profile, to model the observed absorption lineshape. Understanding the characteristics of the Voigt profile becomes pivotal for the analysis of collected spectra. Mathematically, normalized line profiles are equivalent to probability distributions. If we consider a Gaussian (normal) distribution with standard deviation  $\sigma$  and a Lorentzian (Cauchy) distribution with width parameter  $\gamma$ , both centered at 0 for convenience, then we define the Voigt profile as their convolution

$$V(x, \sigma, \gamma) = \int_{-\infty}^{\infty} G(x', \sigma) L(x - x', \gamma) dx', \quad (2.12)$$

where  $x$  is the shift from the line center, and

$$G(x, \sigma) \equiv \frac{1}{\sqrt{2\pi}\sigma} e^{-\frac{x^2}{2\sigma^2}} \text{ and} \quad (2.13)$$

$$L(x, \gamma) \equiv \frac{\gamma}{\pi(x^2 + \gamma^2)}. \quad (2.14)$$

The Voigt profile has no analytical solution, but approximations to Voigt profile have been widely studied and we take advantage of the error function. For a detailed discussion of how to use error function to describe Voigt convoluted lineshapes, see Ref. [12].

For the indium Stark shift experiment, we adopt a two-step excitation scheme (formally discussed in Section 2.2.1) which allows us to get rid of the Doppler broadening effect to a large extent. Hence, the lineshape is almost completely determined by a Lorentzian shape. Simulations from previous work in our group have shown that there is no systematic differences between fitting spectra from such a two-step excitation path to a Lorentzian function and fitting these spectra to a Voigt profile. The fitting program that considers a simple Lorentzian profile improves the computation efficiency by a noticeable amount. Thus, we elect to characterizing the lineshape with a Lorentzian profile.

For the lead transition amplitude measurements, both the Gaussian width and Lorentzian width need to be incorporated, and thus a Voigt profile is necessary to describe the lineshape. According to Table 2.1, Doppler broadening governs the Gaussian width and pressure

broadening overwhelmingly determines the Lorentzian width, as other broadening mechanisms contribute negligible amount of Lorentzian widths in comparison. The Gaussian width is closely related to the temperature as Equation 2.6 demonstrates and the Lorentzian width is determined by Equation 2.11. Consequently, it is key for us to have accurate temperature control to confine the possible range of the Gaussian width. The extraction of the Lorentzian width is more tricky, as the collisional cross-section for our lead cell is difficult to know. We will elaborate how we analyze convoluted lineshapes and extract these two width parameters in Chapter 5.

## 2.2 Indium Stark Shift Polarizability

This section highlights a few key theoretical concepts that are necessary to design and conduct measurements of indium Stark shift. By no means does this section covers all background theories, but it pinpoints most essential ideas for understanding the general scheme of this experiment. This section starts with a discussion of indium’s energy levels pertinent to the experiment as well as the excitation paths that we consider to use. Then, it moves on to introducing the idea of “polarizability” in the context of indium  $7P$  excited states. Lastly, the section bridges the atomic theory to observables that this experiment actually measures.

### 2.2.1 Two-Step Excitation in Indium

The energy states of interest in the indium Stark effect experiment are the  $7P$  excited states, namely the  $7P_{1/2}$  and the  $7P_{3/2}$  states. In order to drive the atoms up to these excited states, we adopt a two-step excitation scheme. The ground state of the indium atoms is the  $5P_{1/2}$  state, since its ground-level electron configuration is  $[\text{Kr}]4d^{10}5s^25p$  and it has electronic angular momentum  $J = 1/2$ . Direct excitation from this state to  $7P$  states is forbidden by the selection rules. Hence, we bypass an intermediate state, the  $6S_{1/2}$  state, to drive indium atoms to the  $7P$  states through two electric dipole transitions, as Figure 1.1 shows. The first-step transition ( $5P_{1/2} \rightarrow 6S_{1/2}$ ) is at 410 nm while the second step transition ( $6S_{1/2} \rightarrow 7P_{1/2, 3/2}$ ) are in the near IR range (690 nm and 685 nm respectively). Conveniently, all these wavelengths can be produced by economical external cavity diode lasers (ECDLs). Moreover, the two-step excitation path eliminates Doppler broadening, as the first-step transition effectively selects a single velocity class of indium atoms.<sup>2</sup> As a consequence, the second-step laser only interacts with atoms with one or a very small range of velocities, taking the dominant Doppler width out of the analysis picture for this experiment.

---

<sup>2</sup>In reality, a few velocity classes of indium atoms are excited to populate the intermediate state.

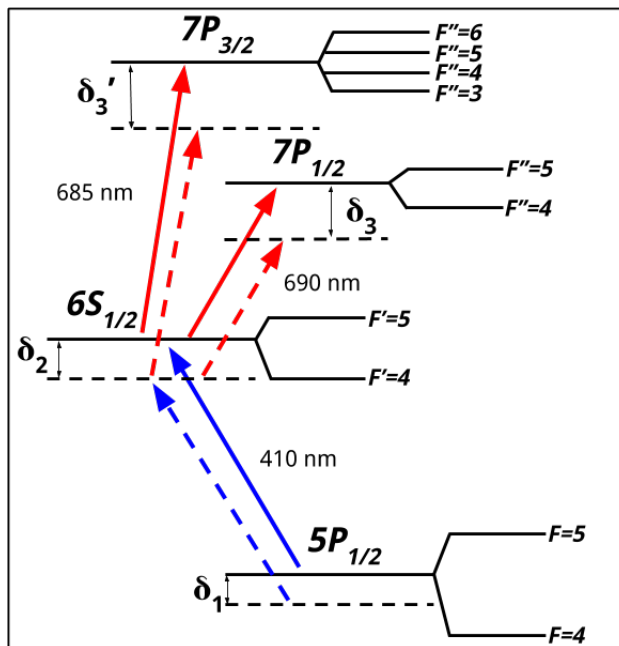


Figure 2.1: Energy structure of  $^{115}\text{In}$  states relevant to the two-step excitation paths. The dotted energy levels represent the Stark shifted energy levels under an external electric field (not to scale).  $\delta$ 's label the Stark shift associated with each state.

The excited indium atoms in the  $6S_{1/2}$  state have extremely short lifetime  $\tau \sim 7$  ns. Therefore, in practice, we interact the sample atoms with both lasers at the same time by overlapping two laser beams through the atomic sample, so that some population of indium atoms can access the  $P$  states before relaxing back to the ground state from the intermediate state. In other words, we need to treat the naive two-(independent)-step transition as a three-level system coupled to two near-resonance EM fields. Treatment of such a three-level system is discussed in detail in Ben Augenbraun's thesis work [7].

## 2.2.2 The Stark Shift Effect

### Perturbation Approach

When an atom is placed in an external electric field, it presents an induced electric dipole, which gives rise to shifted energy levels, as Figure 2.1 illustrates. This phenomenon is known as the Stark shift. With the presence of a relatively low external field,<sup>3</sup> we apply perturbation theory to quantitatively derive the Stark shift effect. The interaction between a sample of

<sup>3</sup>The intrinsic electric field that an indium atom experience on the magnitude of  $\sim 10^7$  kV/cm, while our experiment is executed under a field of order  $\sim 10$  kV/cm or lower. Hence, it is safe to reckon our operation is indeed in the low external field regime

atoms and an external electric field  $\vec{\mathcal{E}}$  can be described by the operator  $V_{\mathcal{E}} = -\vec{\mathcal{E}} \cdot \vec{D}$ , where  $\vec{D}$  represents the atomic sample's electric dipole moment operator,  $\vec{D} = \sum_i q_i \vec{r}_i$ . Proceeding to the first-order perturbation theory,

$$E_{\eta}^{(1)} = -\langle \psi_{\eta}^0 | V_{\mathcal{E}} | \psi_{\eta}^0 \rangle = 0. \quad (2.15)$$

There exists no linear energy shift due to the odd parity of  $\vec{\mathcal{E}}$ .<sup>4</sup> Turning to second-order perturbation theory, it yields the quadratic Stark effect:

$$E_{\eta}^{(2)} = -\sum_{\nu \neq \eta} \frac{\langle \psi_{\nu}^0 | V_{\mathcal{E}} | \psi_{\eta}^0 \rangle \langle \psi_{\eta}^0 | V_{\mathcal{E}} | \psi_{\nu}^0 \rangle}{E_{\nu}^0 - E_{\eta}^0} = -\frac{1}{2} \sum_{i,j} \alpha_{ij} \mathcal{E}_i \mathcal{E}_j, \quad (2.16)$$

where  $\alpha_{ij}$  are components of the polarizability tensor, defined by:

$$\alpha_{ij} = 2 \sum_{\nu \neq \eta} \frac{\langle \psi_{\nu}^0 | D_i | \psi_{\eta}^0 \rangle \langle \psi_{\eta}^0 | D_j | \psi_{\nu}^0 \rangle}{E_{\nu}^0 - E_{\eta}^0}. \quad (2.17)$$

For our purpose, this complex formalism is simplified by taking the applied uniform and static external field to be in the z-direction,  $\vec{\mathcal{E}} = \mathcal{E} \hat{z}$ . Then we derive a quadratic relationship between the shifted energy and the applied electric field strength:

$$E_{\eta}^{(2)} = -\frac{1}{2} \alpha \mathcal{E}^2, \quad (2.18)$$

where  $\alpha$  is traditionally defined as the Stark shift polarizability. By convention, we write  $\alpha$  in the form

$$\alpha = \alpha_0 \mathcal{J} + \alpha_2 \mathcal{Q}, \quad (2.19)$$

where  $\alpha_0$  and  $\alpha_2$  are numerical constants, while  $\mathcal{J}$  and  $\mathcal{Q}$  are operators which may involve the unit vector of the energy operator  $\hat{E}$  and the angular momentum operator  $\hat{J}$ . Conventionally, the constants  $\alpha_0$  and  $\alpha_2$  are called the *scalar* polarizability and the *tensor* polarizability. It turns out  $\mathcal{J}$  is just the identity and the components of  $\mathcal{Q}$  are discussed in Ref. [13]. For our purpose, we quote the expressions of  $\alpha_0$  and  $\alpha_2$  of an atom in a state  $\psi$  with energy  $E$  and total angular momentum  $J$  as:

$$\alpha_0 = \frac{2}{3(2J+1)} \sum_n \frac{|\langle \psi || D || \psi_n \rangle|^2}{E_n - E}, \quad (2.20)$$

---

<sup>4</sup>Note that hydrogen is an exception of a significant linear Stark shift, because of its near degenerate  $s$  and  $p$  states. For indium, there is no such near states to cause a linear shift.

$$\alpha_2 = 4 \left( \frac{5J(2J-1)}{6(J+1)(2J+1)(2J+3)} \right)^{1/2} \times \sum_n (-1)^{J+J_n} \begin{Bmatrix} J & 1 & J_n \\ 1 & J & 2 \end{Bmatrix} \frac{|\langle \psi || D || \psi_n \rangle|^2}{E_n - E}. \quad (2.21)$$

For a more complete discussion and theoretical derivation of the scalar and tensor polarizabilities' functional forms, see Ref. [13] and [14].

### $7P_{1/2}$ State Polarizability

It is apparent from the expressions of the scalar and tensor polarizabilities, for states with  $J = 0$  or  $J = 1/2$ , the tensor polarizability is zero. Thus, for the case of our  $7P_{1/2}$  state Stark shift measurement, there is only a scalar Stark shift common for all hyperfine sublevels. It is expected that we observe an energy shift for each hyperfine sublevel of  $\Delta E = -\frac{1}{2}\alpha_0\mathcal{E}^2$ . In the prior section, we mentioned that we are dealing with Stark shift in a three-level system and a “quantum optic” style approach to such a system is carefully discussed in Ref. [7]. The Hamiltonian of the system can be written as:

$$H_{7P_{1/2}} = \begin{pmatrix} 0 & \Omega_1 & 0 \\ \Omega_1 & -\Delta_1 + (\delta_2 - \delta_1) & \Omega_2 \\ 0 & \Omega_2 & -\Delta_2 - \Delta_1 + (\delta_3 - \delta_1) \end{pmatrix} \quad (2.22)$$

where  $\Omega_1$  and  $\Omega_2$  are the Rabi frequencies of the two laser fields,  $\delta_i$  is the Stark shift at each energy state  $i$ , and  $\Delta_1$  and  $\Delta_2$  are the detuning of the lasers from the resonant frequency. We are interested to know the probability  $P_3$  of excitation from state  $|1\rangle$  to state  $|3\rangle$ , whose time average (what we observe in experiment using photo receiving devices) is given in Ref. [7] by

$$\langle P_3 \rangle = \sum_{j=1}^3 |\langle 3|v_j\rangle\langle v_j|1\rangle|^2, \quad (2.23)$$

where  $|v_j\rangle$  is the  $j$ th eigenvector of the Hamiltonian in Equation 2.22. In practice, we lock our first-step laser to the *true* resonant frequency (Stark-shifted resonance if the electric field is turned on), meaning that  $\Delta_1 = \delta_2 - \delta_1$ . Then, the Rabi frequencies do not have a significant impact on the measured Stark shifts ( $\delta_3 - \delta_2$ ) at our desired level of precision. The analytical lineshape of  $P_3$  is derived to be:

$$\langle P_3 \rangle(\omega) = \frac{2\Omega_1^2\Omega_2^2(\omega^2 + 3(\Omega_1^2 + \Omega_2^2))}{4\omega^4\Omega_1^2 + \omega^2(-8\Omega_1^4 + 20\Omega_1^2\Omega_2^2 + \Omega_2^4) + 4(\Omega_1^2 + \Omega_2^2)^3}. \quad (2.24)$$

The exact shape depends on the ratio  $\Omega_2/\Omega_1$ , whose value needs to be kept high enough to avoid Autler-Townes splitting. Experimentally, we guarantee the absence of Autler-Townes

effect by setting the second-step laser power one order of magnitude larger than the first-step laser power. To bridge our measured Stark shift  $\delta_3 - \delta_2$  and polarizability  $\alpha_0$  (recall that  $\alpha_2 = 0$  here), we define a Stark shift constant

$$k_S \equiv -\frac{\delta_3 - \delta_2}{\mathcal{E}^2} = \frac{1}{2}(\alpha_0(7P_{1/2}) - \alpha_0(6S_{1/2})) , \quad (2.25)$$

which can be readily extracted from our spectral data and fitting. We can then translate  $k_S$  into polarizability language:

$$\alpha_0(7P_{1/2}) = 2k_S + \alpha_0(6S_{1/2}) = 2k_S + \Delta\alpha_0(6S_{1/2} - 5P_{1/2})_{\text{measured}} + \alpha_0(5P_{1/2})_{\text{theory}} , \quad (2.26)$$

where we quote the theoretical calculation of  $\alpha_0(5P_{1/2})$  from Ref. [15] and measured result of  $\Delta\alpha_0(6S_{1/2} - 5P_{1/2})$  from our previous work [16].

### $7P_{3/2}$ State Scalar and Tensor Polarizabilities

In contrast, the  $7P_{3/2}$  state admits a tensor polarizability in addition to the scalar component as  $J = 3/2$  (referring to Equation 2.21). The additional tensor component complicates the picture as we no longer have a clean quadratic relationship between the Stark shift and the electric field strength. As Figure 2.2 shows, the curvature in the Stark shift vs. electric-field-squared plot is introduced by the tensor polarizability. For clarity, we plot the energy shift solely as a result of the tensor piece in Figure 2.3, where the large, common scalar shift is removed from all sublevels. In the low electric field regime (roughly to the left of the dotted line), the tensor polarizability has a relatively minor effect, but under higher fields, the tensor polarizability can no longer be ignored. The tensor component mixes hyperfine states (F states), resulting in a Hamiltonian in the presence of an electric field:

$$H = V_S + V_{\text{hf}}, \quad (2.27)$$

where the hyperfine Hamiltonian,  $V_{\text{hf}}$ , can be found in Ref. [17] and the Stark Hamiltonian,  $V_S$ , is given by

$$\langle Fm_F | V_S | F'm_F \rangle = -\frac{1}{2}\alpha_0\mathcal{E}^2\delta_{FF'} - \frac{1}{2}\alpha_2\mathcal{E}^2\langle Fm_F | Q | F'm_F \rangle,$$

where again, the hyperfine-basis Stark mixing operator  $Q$  is derived in Ref. [13]. Instead of a 3-by-3 matrix, we can generalize the Hamiltonian as a 60-by-60 block matrix

$$H_{7P_{3/2}} = \begin{pmatrix} 0 & \mathbf{\Omega}_1 & 0 \\ \mathbf{\Omega}_1^\dagger & -\Delta_1 + (\delta_2 - \delta_1) & \mathbf{\Omega}_2 \\ 0 & \mathbf{\Omega}_2^\dagger & -\Delta_2 - \Delta_1 + (\delta_3 - \delta_1) + \mathbf{V}_{\text{hf}} + \mathbf{V}_{\text{tens}} \end{pmatrix}. \quad (2.28)$$

The Hamiltonian is block diagonal in  $m_F$  because we take the electric field along the quantization axis. Similarly, we lock the first-step laser to the actual resonant frequency (Stark-shifted or not). For excitation from the ground state to a particular state labeled with

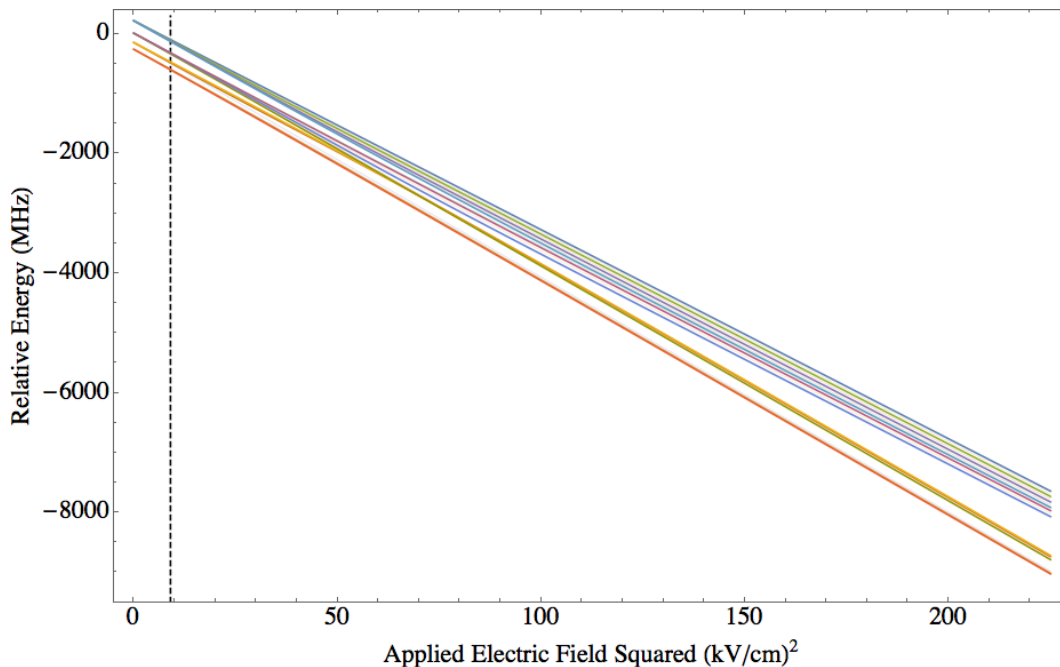


Figure 2.2: The Stark shift in indium  $7P_{3/2}$  excited states corresponding to applied electric-field-squared. The dotted line is located at  $9 \text{ (kV/cm)}^2$ , representing our decided cut-off field strength for the regime in which tensor polarizability is negligible. At higher fields, tensor polarizability begins to contribute significantly, causing energy splittings within each hyperfine state.

hyperfine level  $F''$  and spin  $m_F''$ , the time-averaged probability  $\langle P_{F''m_F''} \rangle$  can be numerically calculated as discussed in Ref. [5].

Analogous to the Stark shift constant  $k_S$  used in the extraction of the  $7P_{1/2}$  scalar polarizability in Equation 2.25, we introduce an “effective” Stark shift constant for each sublevel of the  $7P_{3/2}$  state,

$$k_{\text{eff}} \equiv k_0 + c(F, m_F)k_2, \quad (2.29)$$

which combines the effects of the tensor and scalar polarizabilities so that the observed shift of a level  $|Fm_F\rangle$  between fields  $\mathcal{E}_1$  and  $\mathcal{E}_2$  is given by

$$\Delta\nu = k_{\text{eff}}(\mathcal{E}_2^2 - \mathcal{E}_1^2). \quad (2.30)$$

Here  $k_0 = -\frac{1}{2h}[\alpha_0(7P_{3/2}) - \alpha_0(6S_{1/2})]$  as above, and  $k_2 = -\frac{1}{2h}\alpha_2(7P_{3/2})$  analogously. Given this parameterization, we note that both  $k_{\text{eff}}$  and  $k_0$  have negative values, whereas  $k_2$  itself turns out to be positive, though much smaller in magnitude. The coefficients  $c(F, m_F)$  are level-dependent factors of order unity that reflect the relative shift of distinct hyperfine states and can be calculated numerically by diagonalizing the Hamiltonian. The sign of these coefficients is positive for the group of upward-trending states in Fig. 2.3 and negative for the lower frequency, downward-trending states.

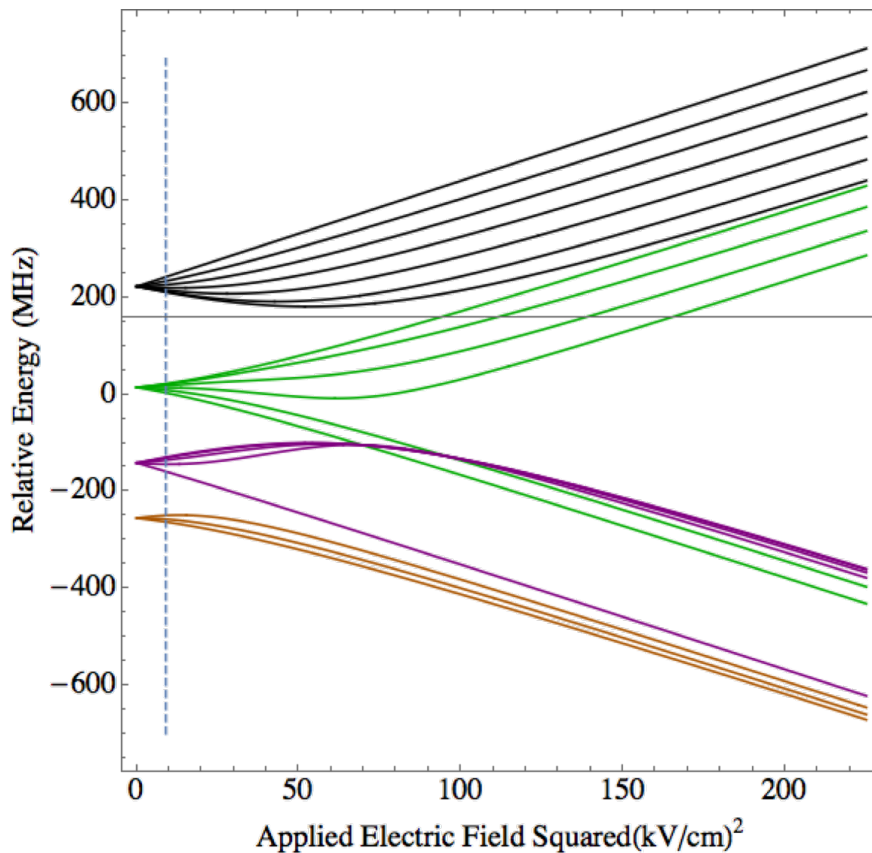


Figure 2.3: Energy eigenvalue structure under an applied electric field for all hyperfine sub-levels of the indium  $7P_{3/2}$  state. Here, the indicated energy shift only results from tensor polarizability, as we exclude the dominant scalar polarizability ( $-\frac{1}{2}\alpha_0\mathcal{E}^2$ , shared by all  $|F, m_F\rangle$  levels). Each color represents one hyperfine level.

Such a formulation is only approximate, as the shift effected by the tensor polarizability is not purely quadratic in the electric field. Equivalently, one can view the coefficient  $c(F, m_F)$  as having a slight electric-field dependence. Nonetheless, for the limited range of large electric fields used to extract the tensor polarizability, the uncertainty in a measurement of  $\alpha_2$  due to imprecision in this simple field-independent model for  $c(F, m_F)$  is at the level of 0.5% or below, and can be neglected when compared to other experimental errors, as discussed in chapter 3. The final fractional experimental uncertainty in the tensor polarizability of the  $7P_{3/2}$  state is quite large in comparison to our scalar polarizability measurements, partly because of its size relative to the scalar component, and partly because of the complications of composite spectral peaks associated with multiple unresolved, but non-degenerate magnetic sublevels. We note that our final result for the  $7P_{3/2}$  state polarizability with  $\sim 12\%$  experimental uncertainty is in agreement with, and of comparable precision to, the theoretical prediction as presented in Chapter 3.

## 2.3 Transition Amplitude and Faraday Rotation

Now we shift gears to survey a few atomic theory topics relevant to the second experiment described in this thesis: measuring an electric quadrupole (E2) transition amplitude in lead using Faraday rotation spectroscopy. The target E2 transition in lead is too weak to be observed in direct absorption spectroscopy. The first experimental challenge then is to design and implement an experimental technique sensitive to this extremely weak transition. We employ the Faraday rotation spectroscopy technique as a solution. To minimize the measurement error from experimental parameters involved in this technique, we choose to find the transition amplitude ratio between two transitions driven from the same ground state ( $6s^26p^2\ ^3P_0 \rightarrow\ ^3P_{1,2}$ ), as shown in Figure 1.2. Since the transition probability of the M1 transition is known, we can extract the desired E2 transition amplitude from the ratio. Both the magnetic dipole (M1) and the electric quadrupole (E2) transitions are much weaker than their electric dipole (E1) counterpart, but the Faraday rotation technique enables us to probe these transitions with a great signal-to-noise ratio. The Faraday rotation technique makes the E2 transition amplitude measurement possible but at the cost of complicating the spectral lineshapes. The second major challenge of this experiment then emerges: we need to understand these complicated lineshapes as well as to develop a robust analysis routine to extract the amplitude. In this section, I outline the theoretical background knowledge necessary to understand our Faraday rotation technique and to tackle the lineshape fitting challenge. Similar to the organization in Section 2.2, I begin with discussing the transition matrices in the context of perturbation theory; next, I outline the Faraday rotation technique, derive the expected lineshapes, and explain the connection between the lineshapes and matrix elements. This section serves as a theoretical preparation for comprehending our experimental method and data analysis approach, which are described in detail in Chapter 4 and 5 respectively.

### 2.3.1 M1 and E2 Transition in Lead

Just like the E1 transition discussed in the indium experiment, the M1 and E2 transitions can be modeled by thinking of the interaction between the incident EM field and the atomic system. Again, we use perturbation theory in the regime of a weak perturbing EM field to express the matrix elements governing the intrinsic transition strengths.

#### Time-Dependent Perturbation Theory

In this experiment, we aim to measure the ratio of matrix elements governing the intrinsic strength of the  $6s^26p^2\ ^3P_0 \rightarrow\ ^3P_{1,2}$  transitions. We first write down the matrix elements

associated with the intrinsic strength of the two transitions of interest:

$$\frac{\langle j' = 2 | q_e | j = 0 \rangle}{\langle j' = 1 | \mu_m | j = 0 \rangle}, \quad (2.31)$$

where  $q_e$  and  $\mu_m$  are the electric quadrupole and magnetic dipole moments, respectively.

Following the semi-classical treatment of the interaction between atoms and a loosely coupled EM field in Ref. [18], we turn to time-dependent perturbation theory to derive the probability of a certain transition. The perturbing EM field can be characterized by its scalar and vector potentials,  $V$  and  $\mathbf{A}$ , giving a total Hamiltonian of:

$$\hat{H} = \frac{1}{2m} [\hat{\mathbf{p}} - e\mathbf{A}(r, t)]^2 + eV(r), \quad (2.32)$$

where  $\hat{\mathbf{p}}$  is the momentum operator of an atom, and  $e$  and  $m$  are the atom's charge and mass. The unperturbed Hamiltonian for an atom is  $\hat{H}_0 = \frac{\hat{\mathbf{p}}^2}{2m} + V$ . Then, the total Hamiltonian becomes (dropping the negligibly small term  $e^2\mathbf{A}^2$ ):

$$\hat{H} = \hat{H}_0 - \frac{e}{2m} (\hat{\mathbf{p}} \cdot \mathbf{A} + \mathbf{A} \cdot \hat{\mathbf{p}}). \quad (2.33)$$

Consider a transverse field, for which  $[\mathbf{A}, \hat{\mathbf{p}}] = 0$ . Then  $\hat{H} = \hat{H}_0 - \frac{e}{m} \hat{\mathbf{p}} \cdot \mathbf{A}$ . Let the propagation direction of the EM wave be in the  $\hat{z}$ -direction, then the vector potential  $\mathbf{A} = A_0 \cos(\omega t - kz)\mathbf{x}$ , where  $\omega$  is the oscillation frequency and  $k$  is the magnitude of the wave vector  $\mathbf{k}$ . Without loss of generality, we use  $x$  to represent a general transverse direction in which the electric field or magnetic field points. Going through the rotating wave approximation discussed in Ref. [18], we conclude that the matrix elements of the perturbing Hamiltonian are:

$$\hat{H}_{ij} = A_0 \frac{e}{m} \langle i | \hat{\mathbf{p}} \cdot \mathbf{x} e^{-ikz} | j \rangle. \quad (2.34)$$

The transition rates are governed by the square of the matrix elements. If we take the decaying mechanism from an excited state into account, we need to additionally include a phenomenological damping parameter  $\Gamma$ , the natural linewidth we discussed in Section 2.1.2.

The atomic length scale approximately is a few  $\text{\AA}$  while our laser wavelengths are near  $1 \mu\text{m}$ . For very small  $z$  deviation, we Taylor expand:  $e^{-ikz} = 1 - ikz + \dots$ . Our typical laser beam waist is around  $10^4$  times larger than the atomic size. In this regime, the EM radiation can be regarded to have negligible spatial variation and one may be attempted to approximate the field as a standing wave by only considering the first term, the unity, in the multipole expansion. This term is accountable for the electric dipole transition and thus the above procedure is commonly known as the dipole approximation. As Ref. [18] shows, one can use commutation properties to reduce Equation 2.34 to

$$\hat{H}_{ij} = A_0 i \omega_0 \langle i | e \mathbf{r} | j \rangle. \quad (2.35)$$

The matrix element in the above equation only depends on position and electric charge: it is indeed the familiar electric dipole moment. This method is sufficient when an E1 transition overwhelmingly dominates,<sup>5</sup> but when the first-order effect vanishes in accordance with the selection rules, this approximation overlooks the nuances caused by higher order EM radiation. In order to study M1 and E2 transitions, we cannot entirely ignore the EM field's minute spatial variation. Instead, we include the second term in the multipole expansion, which leads to a description of magnetic dipole and electric quadrupole radiation. Following a derivation similar to the electric dipole matrix element, we find the perturbing Hamiltonians for the magnetic dipole and electric quadrupole are:

$$\begin{aligned}\hat{H}_m^2 &= A_0^2 \left(\frac{\omega_0}{c}\right)^2 \langle i | \mu_m | j \rangle^2, \\ \hat{H}_{qe}^2 &= A_0^2 \left(\frac{\omega_0^2}{2c}\right)^2 \langle i | e(xz + yz) | j \rangle^2.\end{aligned}\tag{2.36}$$

M1 and E2 have different multipole orders, and therefore different selection rules. As a consequence, the magnetic dipole operator is only allowed to drive atoms in the triplet states from  $^3P_0$  ground state to  $^3P_1$ , while the electric quadrupole operator is solely responsible for driving ground state atoms to  $^3P_2$  state, as shown in Figure 1.2. For more details regarding the derivation of matrix elements, see Ref. [18] and Ref. [12]. As I alluded in the beginning of this section, the experiment aims to find the ratio between the M1 and E2 transition amplitudes rather than a single transition in isolation. Hence, we just need to theoretically determine the ratio between the matrix elements associated with M1 and E2 transition. I shall defer further discussion of the matrix elements' ratio until the very end of this section, where the link between this theoretical ratio and the expected spectral lineshapes will be made clear.

### 2.3.2 Faraday Rotation Spectroscopy

Now, putting our favorite perturbation theory aside, I will lay out the theoretical foundation for the Faraday rotation spectroscopy technique, the understanding of which is indispensable for deriving the lineshapes we expect to observe. To begin with, we introduce the concept of the complex index of refraction and derive its mathematical expression.

#### Complex Index of Refraction

Consider the complex form of an EM field propagating in  $\hat{z}$ -direction:

$$\begin{aligned}\tilde{\mathbf{E}} &= E_0 e^{i(\omega t - kz)} \hat{x}, \\ \tilde{\mathbf{B}} &= \frac{E_0}{c} e^{i(\omega t - kz)} \hat{y},\end{aligned}\tag{2.37}$$

---

<sup>5</sup>The relative transition strengths ratio between E1 and M1 (or E2) scales with the fine constant  $\alpha^2$ , as shown in Ref. [18].

where  $\omega$  is the oscillation frequency and  $k$  is the complex wave number. These two quantities are related by the complex index of refraction  $\tilde{n}$ :

$$k = \frac{\omega \tilde{n}}{c}. \quad (2.38)$$

The complex index of refraction consists two terms as expected,  $\tilde{n} = n + i\kappa$ . The real part, our familiar index of refraction  $n$ , indicates the phase velocity, while the imaginary part,  $\kappa$ , is the extinction ratio, suggesting the level of attenuation when an EM wave passes through a material. The complex index of refraction is in fact polarization-dependent. Hence, before further discussion, we convert these field expressions from the linear basis to the circular basis for convenience:

$$\begin{aligned} \tilde{\mathbf{E}} &= \frac{E_0}{\sqrt{2}} \left[ e^{(i\omega t - i\frac{\omega \tilde{n}_-}{c}z)} \hat{\sigma}_- - e^{(i\omega t - i\frac{\omega \tilde{n}_+}{c}z)} \hat{\sigma}_+ \right], \\ \tilde{\mathbf{B}} &= \frac{iE_0}{c\sqrt{2}} \left[ e^{(i\omega t - i\frac{\omega \tilde{n}_-}{c}z)} \hat{\sigma}_- + e^{(i\omega t - i\frac{\omega \tilde{n}_+}{c}z)} \hat{\sigma}_+ \right], \end{aligned} \quad (2.39)$$

where  $\hat{\sigma}_+$  and  $\hat{\sigma}_-$  are unit vectors denoting the directions of two basis polarizations, right-handed circularly polarized light (RHC) and left-handed circularly polarized light (LHC);  $\tilde{n}_+$  and  $\tilde{n}_-$  are the complex indices of refraction associated with RHC and LHC. From the expressions in Equation 2.39, we can conceptualize the significance of the real and imaginary parts of  $\tilde{n}$  from a mathematical perspective. It is apparent that the real part of  $\tilde{n}_\pm$ , together with  $e^{i\omega t}$ , becomes a phase shift term. In contrast, the imaginary part of  $\tilde{n}_\pm$  is an exponential decay term, corresponding to the observed atomic absorption.

We can derive the form of  $\tilde{n}$  for the M1 transition. Under an applied magnetic field, the induced magnetic dipole moment  $\mu_m$  is

$$\rho \langle \mu_m \rangle = \frac{1}{\mu_o} (1 - \mu) |\mathbf{B}|, \quad (2.40)$$

where  $\rho$  is the macroscopic number density and  $\mu$  is magnetic permeability.<sup>6</sup> Using time-dependent perturbation theory, we can express  $\mu_m$  in terms of the dipole matrix element  $\langle 1 | \mu_m | 0 \rangle$ . Analogous to the derivation for the case of an electric dipole moment in Ref. [19], we find

$$\langle \mu_m \rangle = \frac{1}{\hbar} \frac{\langle 1 | \mu | 0 \rangle^2}{(\omega - \omega_o)^2 + \Gamma^2} (\omega - \omega_o + i\Gamma) |\tilde{\mathbf{B}}|. \quad (2.41)$$

For an M1 transition, the electric permittivity  $\epsilon \approx 1$ , and since  $\tilde{n} = \sqrt{\epsilon\mu}$ , we can replace each  $\mu$  in Equation 2.41 with  $\sqrt{\tilde{n}}$ . Then, we solve for  $\tilde{n}$  and find:

$$\tilde{n} = 1 + \beta \frac{\omega - \omega_o + i\Gamma}{(\omega - \omega_o)^2 + \Gamma^2}, \quad (2.42)$$

---

<sup>6</sup> $\mu_o$  is the magnetic permeability in free space.

where  $\beta$  depends on the specific matrix element. For the M1 transition,

$$\beta_{M1} = \langle 1|\mu_m|0\rangle^2 \frac{\rho\mu_0}{2\hbar}. \quad (2.43)$$

For the case of an E2 transition, the background theory is much more intricate, as it involves a second-order tensor relating the quadrupole moments of the atomic system to the external EM field. However, the functional form of an electric quadrupole moment ends up being the same as that of an electric dipole moment after replacing the dipole matrix element with the quadrupole matrix element, as Ref. [12] shows. Following the same argument, we arrive at the expression of the electric quadrupole moment:

$$\langle q_e \rangle = \frac{1}{\hbar} \frac{\langle 2|q_e|0\rangle^2}{(\omega - \omega_o)^2 + \Gamma^2} (\omega - \omega_o + i\Gamma) \left| \tilde{\mathbf{E}} \right|. \quad (2.44)$$

Similarly, in the expression of an induced electric dipole  $\rho\langle D \rangle = \epsilon_o(1 - \epsilon)|\mathbf{E}|$ , we replace the electric permittivity  $\epsilon$  with  $\sqrt{\tilde{n}}$  since the magnetic permeability  $\mu \approx 1$  for an electric dipole or quadrupole transition. Solving for  $\tilde{n}$ , we derive the same expression as in Equation 2.42, just with a different  $\beta$ :

$$\beta_{E2} = \langle 2|q_e|0\rangle^2 \frac{\rho}{2\epsilon_o\hbar}. \quad (2.45)$$

If we expand our expression for  $\tilde{n}$  into a sum of a real term and an imaginary one, we find

$$\begin{aligned} \mathbf{Re}[\tilde{n}] &= 1 + \beta \frac{(\omega - \omega_0)}{(\omega - \omega_0)^2 + (\frac{\Gamma}{2})^2} = 1 + \beta D(\omega - \omega_0), \\ \mathbf{Im}[\tilde{n}] &= \beta \frac{\frac{\Gamma}{2}}{(\omega - \omega_0)^2 + (\frac{\Gamma}{2})^2} = \beta L(\omega - \omega_0). \end{aligned} \quad (2.46)$$

These functional forms imply the lineshapes that the real and imaginary parts of the refractive index are associated to. The imaginary term corresponds to a Lorentzian function  $L(\omega)$  with width parameter  $\Gamma$  around  $\omega_0$ . The real term, as it turns out, represents a dispersive shape  $D(\omega)$ , as Figure 2.4 shows. Now armed with the expression of the complex index of refraction, we can readily determine the atomic absorptivity and thus infer the transmission lineshape from the imaginary part of  $\tilde{n}$ . Yet, in order to derive the lineshape of the Faraday rotation signal, which is governed by the real part of the index of refraction, more theory work needs to be laid out.

## Zeeman Effect

The essential theory behind our Faraday rotation spectroscopy is the Zeeman effect: in the presence of an external static magnetic field,  $m_j$  energy levels shift and thus splitting from otherwise degenerate spectral line. In the regime of a weak external field, in which the

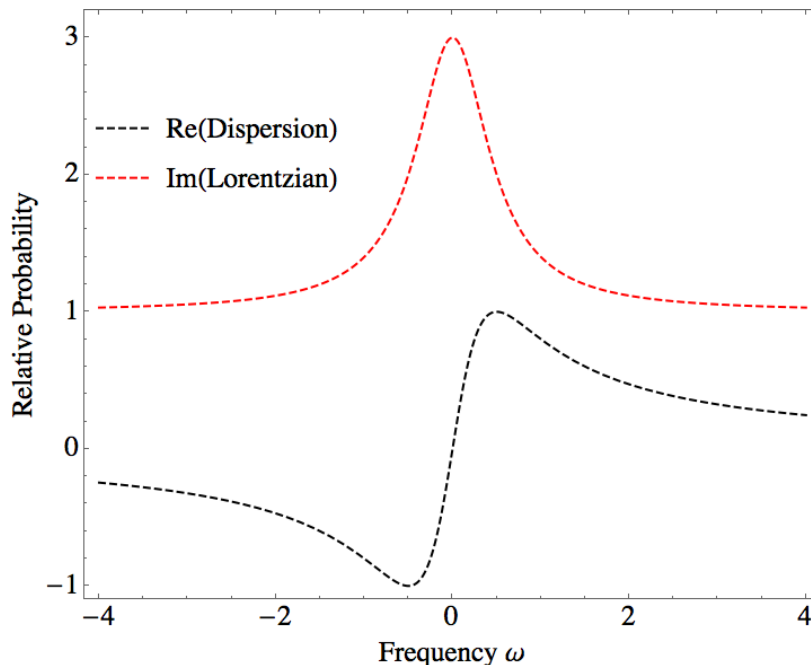


Figure 2.4: A qualitative representation of the lineshapes associated with the real and imaginary parts of the complex refractive index. It is obvious that  $\mathbf{Re}[\tilde{n}]$  corresponds to a dispersive shape, and  $\mathbf{Im}[\tilde{n}]$  to a Lorentzian shape.

Zeeman splitting is small compared with the fine structure, we can approximate the energy shift to be:

$$\delta E = \hbar\delta\nu = \mu_B B m_j g_j, \quad (2.47)$$

where  $\mu_B$  is the Bohr magneton and  $g_j$  is the Landé  $g$ -factor corresponded to total angular momentum  $j$ . The expression of the  $g$ -factor and details of the weak field approximation of Zeeman effect are discussed in detail in Ref. [18]. The Zeeman effect gives rise to differential absorption for RHC and LHC, leading to the so-called optical activity. Intuitively, optical activity results from the different indexes of refraction associated with RHC and LHC, meaning the two circular polarization states have different phase velocities in a material. In our case, the Zeeman shifted energy levels cause a frequency difference in absorption between RHC and LHC, which is a special case of optical activity – the Faraday rotation.

We apply an axial (parallel to the light propagation direction) magnetic field to the lead cell.<sup>7</sup> The resulting energy shift slightly separates  $m_j$  sublevels in the two excited states ( $6s^26p^2\ ^3P_{1,2}$ ), causing a differential index of refraction as a consequence of the frequency shift. Due to the selection rule by angular momentum conservation,  $\Delta m = \pm 1$ , the laser light imparts  $\pm\hbar$  angular momentum along the quantization axis depending on the circular polarization. As Figure 2.5 shows, the atoms absorbing RHC ( $\sigma_+$ , composed of only photons

<sup>7</sup>This measure eliminates light with  $\pi$  polarization, which drives the ground atoms to  $m_j = 0$  excited state, and thus maximizing the Faraday rotation signal.

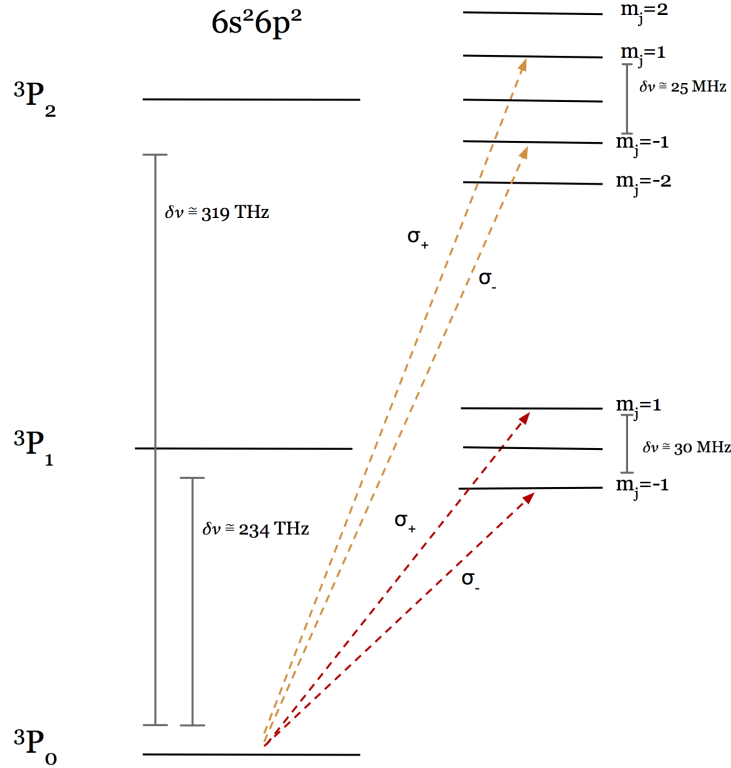


Figure 2.5: Zeeman splittings in the energy states relevant to current experiment. Every  $\delta\nu$  represents the frequency differences between  $m_j$  states in a given energy level. RHC ( $\sigma_+$ ) and LHC ( $\sigma_-$ ) excite atoms to different  $m_j$  sublevels, leading to the index of refraction’s polarization dependence.

with angular momentum  $\hbar$ ) are excited to  $m_j = 1$  states while those absorbing LHC ( $\sigma_-$ , composed exclusively of photons with the opposite angular momentum  $-\hbar$ ) are excited to a lower frequency,  $m_j = -1$  states. Note that for  $^{208}\text{Pb}$ , there is no hyperfine structure to further complicate the situation, due to the isotope’s lack of nuclear spin. Our argument so far only considers the Zeeman effect in LS coupling, dismissing the interplay between Zeeman splitted  $m_j$  sublevels and hyperfine structures. For  $^{208}\text{Pb}$ , this treatment is totally valid in the absence of hyperfine structures, but if we study other isotopes in lead in future, such as  $^{207}\text{Pb}$ , we need to take the mixing between hyperfine structure and Zeeman splitting into account.

Recall that in the previous sub-section, we demonstrated how the complex index of refraction depends on frequency (Equation 2.42). Putting these two ideas together,  $\tilde{n}$ ’s dependence on laser frequency and helicity results in a frequency-dependent optical rotation when light passes through an optically active material, in our case, the lead cell. We can write the Zeeman-shifted refractive index by adding the Zeeman shift  $\delta\nu$  to the argument in Equation

2.46:

$$\begin{aligned}\mathbf{Re}[\tilde{n}_{\pm}(\omega)] &= 1 + \beta \frac{(\omega - \omega_0 \pm \delta\nu)}{(\omega - \omega_0 \pm \delta\nu)^2 + (\frac{\Gamma}{2})^2}, \\ \mathbf{Im}[\tilde{n}_{\pm}(\omega)] &= \beta \frac{\frac{\Gamma}{2}}{(\omega - \omega_0 \pm \delta\nu)^2 + (\frac{\Gamma}{2})^2}.\end{aligned}\tag{2.48}$$

Recall that the real part of the complex refractive index represents the phase shift. Therefore, the relative phase shift between the LHC and RHC leads to a difference in polarizations, giving rise to the the optical rotation angle:

$$\phi_F(\omega) = \frac{\omega l}{c}(\mathbf{Re}[\tilde{n}_+(\omega)] - \mathbf{Re}[\tilde{n}_-(\omega)]),\tag{2.49}$$

where  $l$  represents the length of our lead cell and  $\delta\nu$  is the Zeeman shift in a given  $m_j$  state as indicated in Figure 2.5 for lead  $6p^2 \ ^3P_{1,2}$  levels. We plot the Zeeman-shifted refractive index for the two polarizations of light in Figure 2.6.

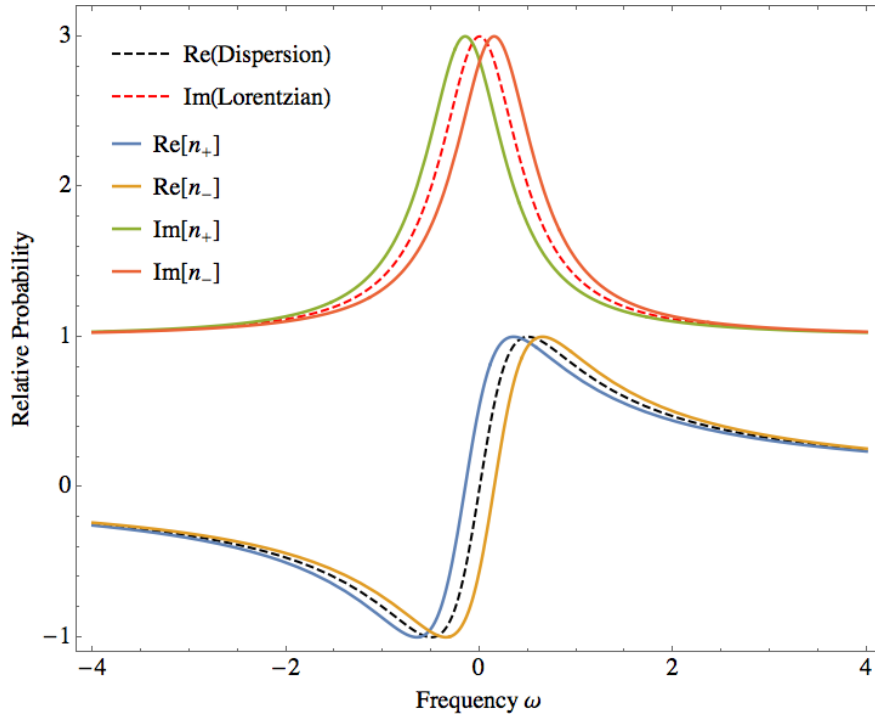


Figure 2.6: A qualitative representation of the Zeeman-shifted dispersive and Lorentzian curves, associated with the real and imaginary parts of the complex refractive index. The unshifted curves first shown in Figure 2.4 are replotted as dashed lines.

### 2.3.3 Spectra Lineshape and Matrix Elements

In practice, the characteristic shapes of the real and imaginary parts of the complex refractive index are reflected in the Faraday rotation spectra and transmission spectra. In other words, collecting these two types of spectra enables the uncovering of underlying physics at the heart of an atomic transition. Yet, linking the laser spectra we observe back to fundamental atomic theory (the transition matrix elements, in our case), is neither trivial nor transparent. We now discuss how we connect the abstract matrix elements to our experimental observables.

#### Faraday Rotation Lineshape

We can explicitly express the lineshape of a Faraday rotation spectrum for a generic matrix element  $\langle j'|T^k|j\rangle$ , where  $T^k$  represents the magnetic dipole moment or the electric quadrupole moment for this experiment (with superscript  $k$  indicating the multipole order). Recall that the expression for  $\mathbf{Re}[\tilde{n}_{\pm}(\omega)]$  involves  $\beta$ , which contains the matrix element of interest. We can describe the ideal lineshape, without Doppler broadening, produced by our Faraday rotation unit as:

$$F(\omega) = \omega_0 \langle j'|T^k|j\rangle^2 \frac{\rho\ell}{2\hbar c} \left[ D(\omega - \omega_0 - \delta\nu) - D(\omega - \omega_0 + \delta\nu) \right], \quad (2.50)$$

where  $D(\omega)$  is defined in the real part of the complex refractive index in Section 2.3.2 and the expression of  $\beta$  is generalized for a generic transition. We perform an expansion in the real part of the index of refraction:  $n'_{\pm}(\omega) = n_{\pm}(\omega) + \delta\nu \frac{dn_{\pm}}{d\omega}$ , for small frequency deviation  $\delta\nu$ .<sup>8</sup> This approximation transforms  $F(\omega)$  from a difference-like function to a derivative-like one, where the Zeeman shift no longer participates as part of the argument but conveniently as a scaling factor. As mentioned in Section 2.1.3, the expected lineshape  $F(\omega)$  is broadened, dominantly by the Doppler effect. Consequently, the real lineshape we observe is the described Faraday rotated curve convoluted over the velocity distribution of atoms following the Maxwell-Boltzmann statistics (a Gaussian function), which we define as:

$$C(\omega) = \int_{-\infty}^{\infty} G(x') F(\omega - x') dx'. \quad (2.51)$$

The convolved lineshape depends on a Gaussian width  $\Gamma_D$  in addition to the Lorentzian width parameter  $\gamma$  (introduced in the dispersion curve  $D(\omega)$ ). As we alluded, the Voigt profile is not analytic but numerically integrated. The derivative approximation eases the integration process when calculating the Voigt convolution. Figure 2.7 shows the idealized lineshape  $F(\omega)$  and the convolution  $C(\omega)$ . Suppose we collect Faraday rotation spectra for the M1 of E2 transitions in lead and extract the peak heights from experimental measurements.

---

<sup>8</sup>We can do such an approximation because the Zeeman shift ( $\sim 15$  MHz) is much smaller than the Lorentzian width and Doppler width (a few hundred MHz).

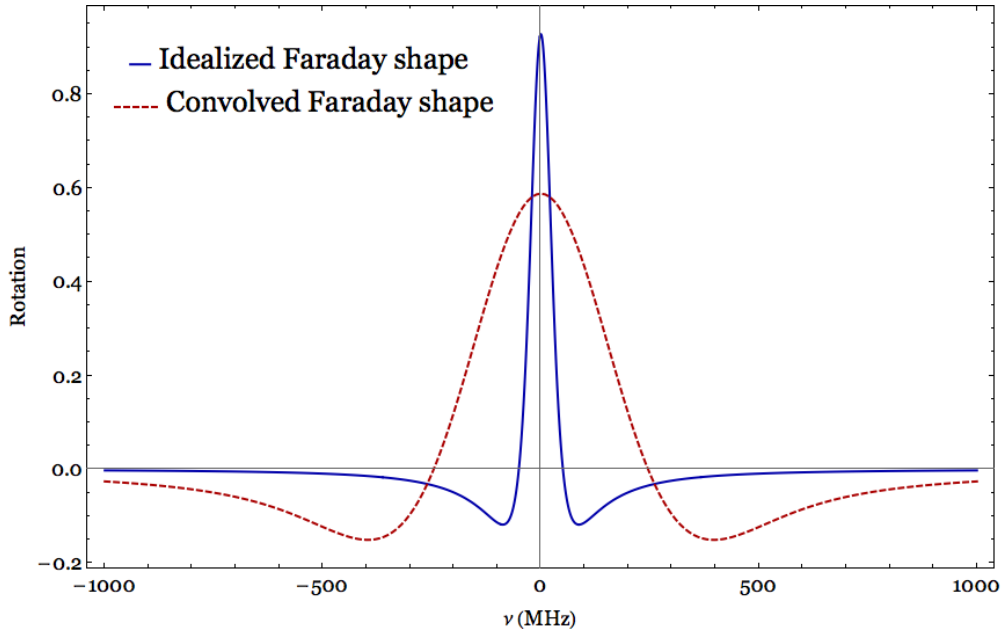


Figure 2.7: The Faraday rotation lineshape is shown along with its convolution with a Gaussian function. The center frequency  $\omega_0$  is set to 0 for convenience. Note that the amplitude of the convolution lineshape has been scaled up by a factor of 10. The absolute scaling is arbitrary, but the relative maxima are dependent; in this case, their ratio is a function of the Lorentzian and Gaussian widths.

Then, we can infer the ratio between the squares of the two matrix elements that govern the intrinsic transition strengths. The relationship between the measured amplitudes and the matrix elements is summarized below:

$$\frac{C(\omega_0)_{\text{expt},E2}}{C(\omega_0)_{\text{expt},M1}} \propto \frac{B\rho l \langle 2|q_e|0\rangle^2}{B\rho l \langle 1|\mu_m|0\rangle^2} \frac{f_{E2}(\omega, \Gamma_{D,E2}, \gamma_{E2})}{f_{M1}(\omega, \Gamma_{D,M1}, \gamma_{M1})} \frac{\omega_{0,E2} g_{E2}}{\omega_{0,M1} g_{M1}}, \quad (2.52)$$

where  $C(\omega_0)$ 's are the observed peak of optical rotation and  $g$ 's are Landé factors as mentioned earlier. We pull the constants (effectively one correction factor) outside the convolution integral, leaving  $f(\omega, \Gamma_D, \gamma)$  to represent the essence of the convoluted lineshape as a function of frequency  $\omega$ , the Doppler width  $\Gamma_D$ , and the Lorentzian width  $\gamma$ . The above expression explicitly shows the advantages of taking the ratio approach to determining the desired E2 transition matrix element, because many constants, such as the density  $\rho$ , the magnetic field strength  $B$ , and cell length  $l$  cancel each other. We introduce fewer potential error sources to the experiment since we do not need to measure these quantities.

### Transmission Spectra and Matrix Element

Now I turn to the imaginary part of the complex refractive index, which is associated with the direct atomic absorption. This important quantity is usually the focus of absorption

spectroscopy, measured by the transmitted laser intensity after the light passes through the Faraday rotation unit. For the lead experiment, even though we cannot obtain much useful information about the E2 transition from the extremely small absorption, we can observe the M1 transmission and extract the M1 transition strength directly from the absorption. Below, we briefly discuss the expected transmission spectra lineshape. The transmitted intensity is proportional to

$$\begin{aligned} \mathbf{E} \cdot \mathbf{E}^* &= \frac{E_0^2}{2} \left( e^{\frac{-\omega \mathbf{Im}[\tilde{n}_-]l}{c}} \hat{\sigma}_- - e^{\frac{-\omega \mathbf{Im}[\tilde{n}_+]l}{c}} \hat{\sigma}_+ \right)^2 \\ &= \frac{E_0^2}{2} \left( e^{\frac{-2\omega \mathbf{Im}[\tilde{n}_-]l}{c}} + e^{\frac{-2\omega \mathbf{Im}[\tilde{n}_+]l}{c}} \right) \\ &\approx E_0^2 e^{-\frac{2\omega l \beta}{c} L(\omega)}, \end{aligned} \quad (2.53)$$

where  $L(\omega)$  is the Lorentzian curve as defined in Section 2.3.2. Similarly, the above expression is the idealized lineshape for our transmission spectra. Doppler broadening ought to be considered in addition to this naive Lorentzian shape when analyzing the transmission spectra. The resulting Voigt profile allows us to directly calculate the transition matrix element, recalling that  $\beta$  contains the matrix element of interest. For a more detailed derivation of how one can extract the matrix element from the Voigt profile, see Ref. [6]. In fact, the observable M1 transition has been well-studied and its matrix element has been calculated with great precision, so we take this known value for granted. Furthermore, collecting M1 absorption data is meaningful for our analysis procedure, since the transmission curve and the convoluted Faraday rotation curve share the same width parameters. The fitted M1 transmission signal then functions as a reference to cross-check the fitted width parameters.

## Reduced Matrix Element Conversion

So far, we have been working with matrix elements that depend on the polarization of light. A more general form, the reduced matrix element, is favored by theorists: after all, the polarization of interacting radiation field should not change a certain atomic system's intrinsic transition strength. To get one more step closer to theoretical predictions, we convert our matrix element to the reduced matrix element following the Wigner-Eckart theorem,

$$\langle j' m' | T_q^k | j m \rangle = \frac{\langle j' || T^k || j \rangle}{\sqrt{2j' + 1}} \langle j, m, k, q | j' m' \rangle, \quad (2.54)$$

where subscript  $q$  denotes the light's polarization and  $\langle j' || T^k || j \rangle$  denotes the reduced matrix element. For a formal discussion of the Wigner-Eckart theorem, see Ref. [11]. For the current lead experiment, the ratio between the reduced matrix elements related to the M1 and E2 transition and that between the corresponding matrix elements differs by a scaling factor,

as explained in Eli Hoenig's thesis [6],

$$\frac{\langle 2||q_e||0\rangle}{\langle 1||\mu_m||0\rangle} = \sqrt{\frac{5}{3}} \frac{\langle 2|q_e|0\rangle}{\langle 1|\mu_m|0\rangle}. \quad (2.55)$$

# Chapter 3

## Indium Atomic Beam Polarizability Measurements in the $7P$ Excited States

This chapter describes the experimental method and presents the final results of the polarizability measurements in indium  $7P$  excited states. This work builds on many previous theses in the Majumder group, such as projects described in Refs. [7, 8], and completes the series of indium Stark shift measurements that began in 2011. In particular, the indium experiment described in this thesis directly stems from Nathaniel Vilas's thesis [5], in which he describes the experimental schematics and method of measuring the Stark shift in indium  $7P$  excited states. Given this history, this chapter will refrain from going into great experimental detail, such as the apparatus, the laser design, and the optical setup. Rather, this chapter aims to concisely provide an outline of the experimental procedure and to highlight new developments as well as the final results, which serve as valuable benchmarks for future theoretical calculations. This work was recently published together with our theoretical collaborators as co-authors (see Ref. [9]).

### 3.1 Experimental Setup and Method

In this section, we outline the experimental approach to indium polarizability measurements in the  $7P_{1/2}$  and  $7P_{3/2}$  states. To achieve the goal of extracting polarizability constants, we measure the energy shifts (the Stark shifts) in the indium  $7P$  hyperfine levels in the presence of an external DC electric field. We apply an external electric field, of order several kV/cm, to a beam of indium atoms housed in a vacuum chamber. In the region of the applied field, the atomic beam intersects with two overlapped counter-propagating laser beams. The first laser is locked to the 410 nm  $5P_{1/2} \rightarrow 6S_{1/2}$  resonance using an auxiliary

indium vapor cell. The second is scanned across the hyperfine levels of either the 690 nm  $6S_{1/2} \rightarrow 7P_{1/2}$  or the 685 nm  $6S_{1/2} \rightarrow 7P_{3/2}$  transition to complete the two-step excitation. We simultaneously observe the same two-step transition in the indium vapor cell without an applied field. A Fabry-Pérot cavity is used to monitor the slightly nonlinear behavior of the second-step scanning laser, as well as to establish a mapping from the voltage applied to the second-step laser to the frequency axis. At the same time, an electro-optic modulator (EOM) generates 1000 MHz sidebands, providing an absolute frequency calibration. A simplified overall experimental schematic is shown in Fig. 3.1.

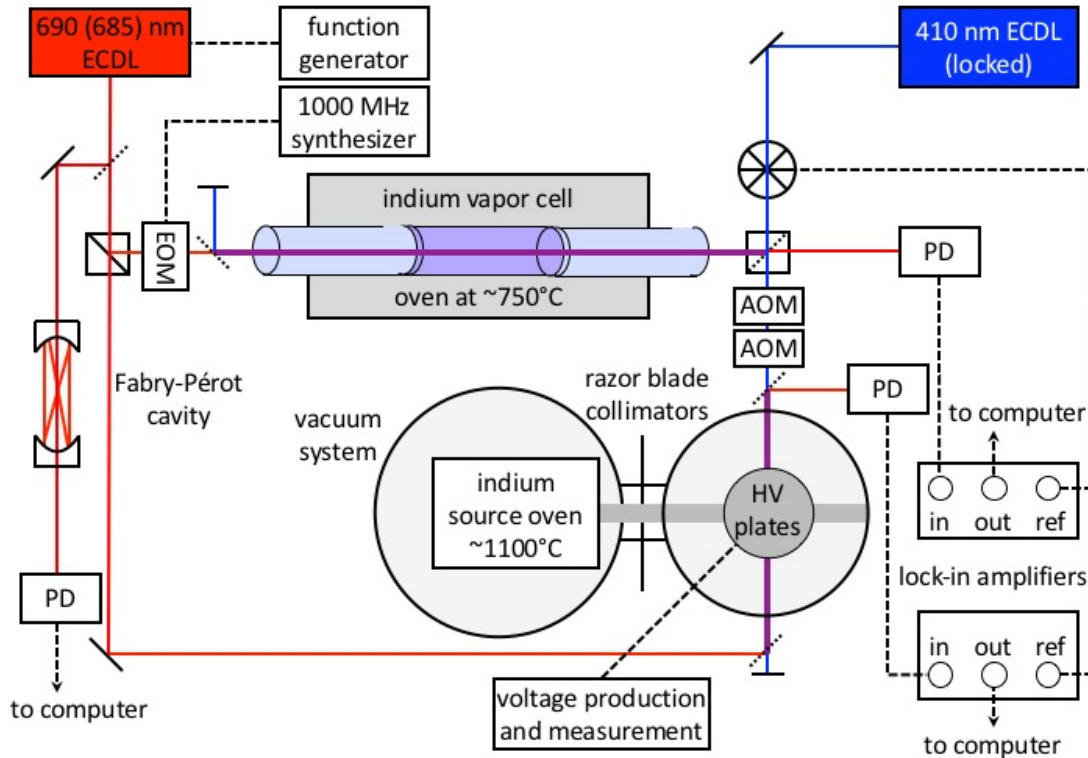


Figure 3.1: Simplified schematic of the optical setup used in indium Stark shift measurements. Here PD refers to a photodetector, EOM to an electro-optic modulator, and ECDL to an external cavity diode laser. Two AOMs (acousto-optic modulators) are inserted in the path of the blue laser beam component which is incident on the atomic beam apparatus in order to maintain resonance for the first-step transition as the electric field, and therefore the resonance frequency, is changed in the interaction region.

### 3.1.1 Atom Beam and External Electric Field

The core experimental design for measuring the Stark shift consists of a collimated beam of indium atoms to which precisely calibrated external DC electric fields are applied. The

electric field generates a static Stark shift, from which we extract the polarizability constants:  $\alpha_0$  and  $\alpha_2$ . The atomic beam path as well as the interaction between the atoms and laser beams are entirely contained in a home-built vacuum chamber. The vacuum chamber is held at the magnitude of  $10^{-6} \sim 10^{-7}$  Torr, which is achieved with the aid of two oil diffusion pumps. The pressure is constantly monitored by an ionization gauge. There are two chambers in the vacuum system: one houses the oven containing a molybdenum crucible filled with solid indium sample, and the other serves as the interaction region where the electric field is applied. The sample of indium metal is first heated up to around  $1100^\circ\text{C}$  by a pair of clamshell heaters to produce an effusive atomic beam, with a water cooling system preventing overheating outside of the crucible. We use several thermocouples to monitor the realtime temperature of the crucible, water pipes, and ambient chamber, and provide a signal for the PID (proportional integral derivative) circuit used to stabilize the temperature. Then, several geometrical collimating stages are inserted along a roughly half-meter-long beam path between the source oven and the interaction region. When we direct the 410 nm first-step laser transversely to the atomic beam, we see a residual Doppler width of roughly 100 MHz as a consequence of this geometry, a significant reduction when compared with the approximately 1.5 GHz Doppler widths we observed in the indium vapor cell.

In the interaction region of the vacuum system, we direct the two laser beams, the atomic beam, and the applied electric field to form a mutually orthogonal configuration, as Figure 3.2 illustrates. The electric field is generated by two circular, 10-cm diameter stainless steel parallel capacitor plates. We measured the plate separation with great care both in the beginning and at the end of data collection process, and the two statistically consistent measurements yield 1.0038(5) cm. We apply voltages of up to 20 kV using a commercial high-voltage (HV) supply (Glassman ER40P07.5) and measure them using a high-precision voltage divider and a calibrated  $6\frac{1}{2}$  digit voltmeter (Keithley 2100) in parallel with the field plates. In the two-step excitation process, the first-step blue laser counter-propagates with respect to the second-step red laser. The first-step laser is locked to the Stark shift-corrected  $5P_{1/2} \rightarrow 6S_{1/2}$  resonance using the signal obtained in an auxiliary vapor cell, which will be discussed in greater depth in the next section. The second-step laser scans over the hyperfine structure of  $6S_{1/2} \rightarrow 7P_{1/2, 3/2}$  resonance to achieve the two-step excitations. The lasers interact with the indium atoms over a 2-cm-wide region in the center of the circular field plates, where the edge effect of the capacitor plates could be neglected. In order to minimize the influence from the Earth's magnetic field in the measurement region, we use three orthogonal sets of magnetic field coils, which manage to cancel the Earth's field to approximately 1  $\mu\text{T}$  locally. The design of this atomic beam unit is practically identical to the that illustrated in our group's previous papers [16, 20] and Nathaniel Vilas's thesis [5].

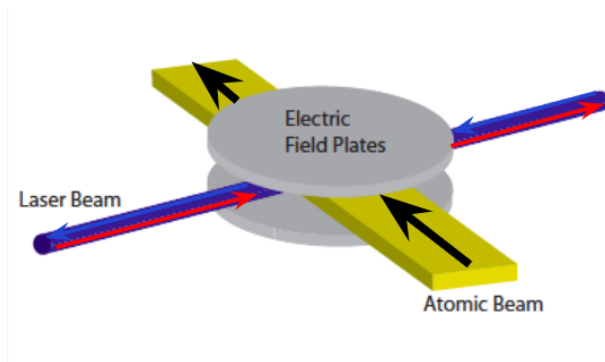


Figure 3.2: The experimental configuration in the interaction region in the atomic beam unit. The two overlapping laser beams (counter-propagating) are orthogonal to the atomic beam in a horizontal plane. The parallel plates provides a vertical static electric field.

### 3.1.2 Vapor Cell

In theory, an atomic beam along with an external electric field would suffice our purpose of measuring the static Stark shift, but our actual experimental scheme includes an additional indium vapor cell system. Atoms in the indium vapor undergo the same two-step transition  $5P_{1/2} \rightarrow 6S_{1/2} \rightarrow 7P_{1/2, 3/2}$  as those in the atomic beam unit, with, of course, no electric field applied to the vapor cell.

The reasons behind including a vapor cell system in the experimental setup are mainly twofold. First, since we apply no electric field to the vapor cell system, the Stark-shift-free spectra obtained from the vapor cell serve as a reliable frequency reference. Due to a higher indium density, we observe a much better signal-to-noise ratio in the second-step laser's transmission signal in the vapor cell than its counter part in the atomic beam. We also perform pivotal frequency calibrations using these the vapor cell spectra.

Second, the vapor cell plays an indispensable role in the locking scheme for the first-step 410 nm laser. A 10-cm-long cylindrical quartz cell containing indium is placed inside of a tabletop oven, which heats the cell to around  $800^\circ\text{C}$ , allowing roughly 80% first-step absorption through the indium sample.<sup>1</sup> The choice of obtaining a roughly 80% absorption instead of a saturated one results from the need of deriving the locking slope from the  $5P_{1/2} \rightarrow 6S_{1/2}$  transition, as there is a trade off between the atomic density and a large locking slope. Further discussion of the locking method will be presented in the next section.

From a practical perspective, the establishment of the vapor cell setup also aids the daily procedure of hunting for an atomic beam signal. The high optical depths of the vapor cell enable us to readily observe the two-step transmission, which allows us to pinpoint the proper scanning range of the second-step laser and to flag the exact location of the hyperfine peaks,

<sup>1</sup>Over the course of data collection, we used different tabletop ovens after the original one broke. We ensured to find the desired temperature associated with each heating device to produce  $\sim 80\%$  absorption.

aiding the optimization of the atomic beam signal.

### 3.1.3 Optical Setup

Our two-step laser spectroscopy experiment obviously involves two lasers – both are external cavity diode lasers (ECDLs) in the Littrow configuration. The first blue ECDL (Toptica DL 100) is locked to one of the Doppler-broadened 410 nm  $5P_{1/2}(F = 4, 5) \rightarrow 6S_{1/2}(F' = 5, 4)$  first-step hyperfine transitions in the supplementary vapor cell using an frequency-modulation spectroscopy technique whose details can be found in Ref. [20]. In short, we pass the a blue laser beam through an EOM driven by a 100 MHz RF synthesizer before directing the beam to interact with the heated vapor cell. The transmitted blue beam is collected by a fast photoreceiver (New Focus Model 1601). We use a RF lock-in amplifier (Stanford Research SR830) and an audio amplifier (Stanford Research SR810) to demodulate the beam, yielding a characteristic dispersive curve with a steep slope. For the purpose of locking, an odd curve about the locking point is desired. Thus we make use of the derivative of the first-step direct absorption, a broadened Gaussian shape curve, to produce a steep locking slope, as Figure 3.3 shows. This technique allows us to achieve frequency stabilization of approximately 0.5 MHz RMS over a timescale of at least two hours. One typical scan only lasts 20 to 30 seconds and our goal is to achieve  $\sim 1$  MHz precision, meaning that we effectively eliminate significant long-term drift of the laser and the residual fluctuations should not contribute to errors above 1 MHz level. Further, by stabilizing the first-step laser directly to the first-step absorption in the vapor cell, we ensure that the blue laser sits at the correct resonance and ideally selects a single velocity class of atoms to populate the intermediate  $6S_{1/2}(F' = 4, 5)$  state, generating a Doppler-free second-step spectrum.

When we apply an external electric field, the shifted energy levels result in a different resonant frequency for the first-step transition in the atomic beam unit. To address this subtlety in the disparate first-step resonances in the vapor cell and the atomic beam, we employ a setup consisting of two acousto-optic modulators (AOMs) to shift the frequency of the 410 nm light, as shown in Figure 3.4. While locking the blue laser to the unshifted first-step resonance through the vapor cell, we direct a portion of the beam through two AOMs (Isomet model 1250C-829A) at 250 MHz before its interaction with the atomic beam.<sup>2</sup> We carefully align the optics so that we pick out the +1 order beam after the first AOM and then the -1 order beam after the second AOM. When the electric field is turned off, the two AOMs effectively output the original frequency. However, once we turn the electric field on, we must shift down the resonant frequency of the 410 nm light by a value that we know precisely from our group’s previous Stark shift measurement (see Ref. [16] and Nathaniel Vilas’s thesis [5]). If calling the shifted amount  $\Delta\nu$ , we program the first AOM to decrease the frequency by  $\Delta\nu/2$  and the second AOM to increase the frequency by  $\Delta\nu/2$ . As a consequence, we manage to

---

<sup>2</sup>Or at a frequency shifted by a small amount from 250 MHz to accommodate the field-on situation as explained.

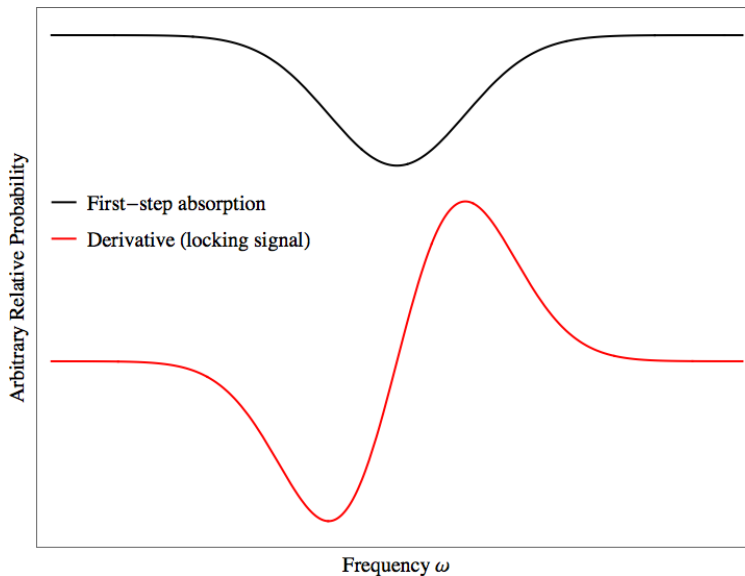


Figure 3.3: A qualitative representation of the raw first-step absorption ( $5P_{1/2} \rightarrow 6S_{1/2}$ ) curve and the RF demodulated derivative curve, which we utilize to lock our 410 nm laser.

shift the first-step laser by the correct frequency to maintain resonant with the shifted 410 nm  $5P_{1/2} \rightarrow 6S_{1/2}$  transition in the atomic beam unit.

A second, home-built ECDL is scanned over the hyperfine levels of the relevant 690 (685) nm  $6S_{1/2} \rightarrow 7P_{1/2(3/2)}$  second-step transition. This second-step red laser is directed in a spatially overlapping, counter-propagating geometry through the atomic beam, while it interacts with both co-propagating and counter-propagating blue beams in the vapor cell. Because of a relatively low indium density in the atomic beam,<sup>3</sup> the red laser absorption signal observed here is rather weak. As a solution, we modulate the 410 nm blue beam directed through the atomic beam with a chopping wheel at  $\sim 1$  kHz. Then, we detect the red laser absorption with a 10 MHz-bandwidth photodiode (New Focus model 2051) and demodulate at the first-step chopping frequency using a lock-in amplifier (Stanford Research SR810). This technique enable us to eliminate background and improve the signal-to-noise ratio for the second-step signal. Despite low optical depths in the atomic beam ( $\sim 10^{-3}$  for the 410 nm transition) and relatively small line strengths associated with the indium  $6S \rightarrow 7P$  transitions (1 to 2 orders of magnitude weaker than in the case of our recent  $6S \rightarrow 6P$  polarizability work), the lock-in detection scheme is sufficiently sensitive to yield second-step hyperfine spectra with peaks resolvable at the 1~2 MHz level for a typical scan. An identical detection scheme is used for the second-step signal detection. The resulting high-resolution spectra of the hyperfine structures serve as stable frequency references for the Stark shift measurements in the atomic beam. Additionally, the red laser beam directed to the vapor cell is modulated

<sup>3</sup>We could increase the atomic density by heating the indium sample to a higher temperature, but such action would expedite the consuming rate of solid indium in the crucible. Hence, we find an appropriate temperature at which the signal-to-noise is acceptable while we avoid opening the vacuum chamber too often.

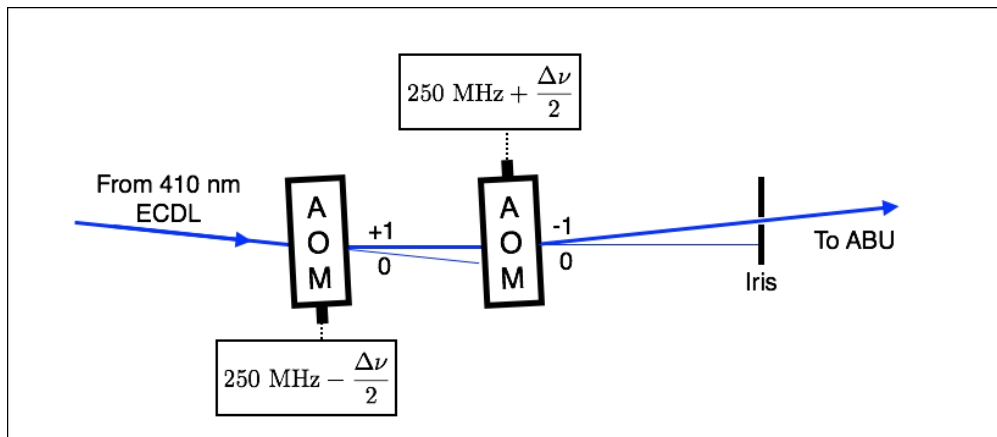


Figure 3.4: The AOM setup for correcting the Stark-shifted first-step transition resonant frequency.

at  $\omega_m = 2\pi \times 1000$  MHz using an EOM, which introduce first-order sidebands at  $\pm\omega_m$  into the vapor cell spectra. The EOM sidebands are used to calibrate the frequency axes of our scans. A small portion of red laser light is also directed into a Fabry-Pérot (FP) cavity, whose free spectral range is  $\approx 363$  MHz. By collecting light through the Fabry-Pérot cavity, we obtain FP transmission spectra whose analysis allows us to eliminate small non-linearity in the tuning of the ECDL with applied voltage, originating in the non-linear response of the piezoelectric element used for the tuning.

## 3.2 Data Acquisition

Data acquisition in this experiment is an automated process realized via a LabVIEW program. This program essentially records four categories of data: the triangle wave voltage ramp driving the red laser’s piezo, the spectrum produced in the Fabry-Pérot cavity, the red laser’s transmission through the vapor cell, and the atomic beam transmission signal. We consider one period of the driving triangle wave as one scan and we typically run the experiment for about 300 successive laser scans before realigning and re-optimizing the optics. Each individual scan is separated into one “upscan” and one “downscan,” which correspond to increasing and decreasing laser frequency with time respectively. To observe the Stark shift in the atomic beam, we collect the pairs of scans under virtually the same condition, except for that each pair has one scan with the external field on and one scan without. We repetitively switch the high voltage (HV) source on and off and the LabVIEW program is designed to pause for around ten seconds after such a switch for the electric field to achieve an equilibrium and then read the true voltage, skipping one scan out of three consecutive ones. As a systematic check, we alternate the order of “field-on” and “field-off” scans in each pair as a way of testing systematics related to the long-term drifts in the field. The program

simply repeats the cycle of “field-on”  $\rightarrow$  switch HV  $\rightarrow$  “field-off”  $\rightarrow$  “field-off”  $\rightarrow$  switch HV  $\rightarrow$  “field-on” (start of another new cycle). Besides the primary data collection, LabVIEW routines are utilized to control and measure the external electric field applied to the atomic beam, as well as to apply and adjust AOM frequency for the purpose of maintaining 410 nm resonance with the Stark shifted transition.

For the  $7P_{1/2}$  scalar polarizability measurements, we collect data at various electric fields between 1 and 6 kV/cm, producing measurable Stark shifts of order several hundred MHz, given the large polarizability of this excited state. We follow the same data acquisition method as described in Nathaniel Vilas’s thesis and for details, see Ref. [5]. Previous experimental work took around 2000 scans of data exclusively in the  $5P_{1/2}(F = 4) \rightarrow 6S_{1/2}(F' = 5)$  first-step transition to draw a preliminary result of the scalar polarizability in this state. More recent work mainly focuses on collecting data along the alternative first-step transition, namely driving the atoms from the  $F = 5$  hyperfine state in the  $5P_{1/2}$  state to populate the  $F' = 4$  hyperfine state in the  $6S_{1/2}$  state, to complete an important systematic check on the possible dependence of our polarizability result on hyperfine transition pathways. Fig. 3.5 shows typical atomic beam field-off/field red laser spectra for the  $7P_{1/2}$  state (top), with the accompanying vapor cell reference/calibration scan below.

For the more complicated  $7P_{3/2}$  case, we instead collect data in two voltage regimes due to complications introduced by the tensor polarizability. From the simulation for the  $7P_{3/2}$  state Stark shift corresponded to only the tensor polarizability (see Fig 3.6), we notice that the tensor contribution is negligible when the external field is low but becomes significant as the field strength increases. Thus, we perform a similar procedure in the low field regime to extract the scalar piece of the  $7P_{3/2}$  state polarizability, as used for the  $7P_{1/2}$  scalar polarizability measurements. Here, we only collect data under electric fields from 1.5 up to 3 kV/cm, for fear that under larger fields, the tensor component of the polarizability plays a noticeable role in complicating the lineshape and the data analysis process. Data collected in this regime yield clean three-hyperfine-peak spectra, confirming that the tensor polarizability has negligible influence under such a low field. Fig. 3.7 shows typical scans in the low field regime for the three excited  $7P_{3/2}$  hyperfine sublevels through two possible excitation paths.

To study the  $7P_{3/2}$  tensor polarizability, we perform spectroscopy under higher electric fields near 15 kV/cm. High fields lead to such large Stark shifts that the scanning range of the second-step laser no longer reach over both the non-shifted hyperfine peaks and the Stark-shifted spectra. Hence, it requires a detuning of the 685 nm laser by roughly 8 GHz from the field-free resonance and the vapor cell reference signal loses its magic. In this regime, rather than alternate “field-on” and “field-off” scans, we set the LabVIEW to alternate between a couple of different high voltage values. For instance, a typical data set acquires scans in the order: 14 kV/cm  $\rightarrow$  15 kV/cm  $\rightarrow$  16 kV/cm  $\rightarrow$  16 kV/cm  $\rightarrow$  15 kV/cm  $\rightarrow$  14 kV/cm (the field switching occurs between every two different fields). This allows for the comparison of consecutive scans with increasing vs. decreasing electric fields, a useful check on systematics relating to long-term drifts in the apparatus, in a similar fashion as we alternate the order

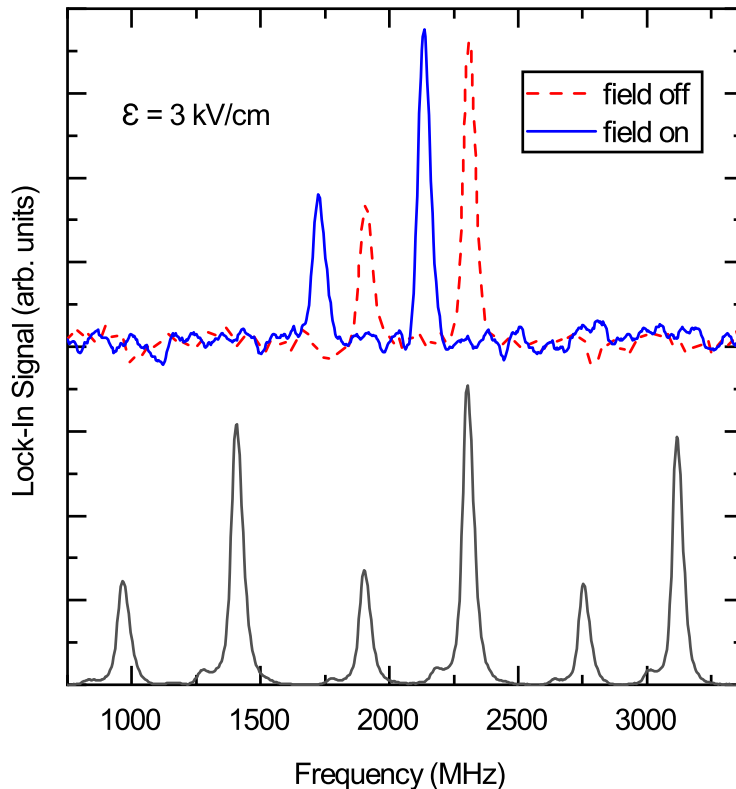


Figure 3.5: Atomic beam spectra for the case of the  $(F' = 4) \rightarrow (F'' = 4, 5)$  transitions of the 690 nm  $6S_{1/2} \rightarrow 7P_{1/2}$  line. The field-off spectrum (red dashed line) and the spectrum with a 3 kV/cm electric field applied (blue solid line) are shown. Displayed below is the corresponding (field-free) vapor cell spectrum, including 1000 MHz FM sidebands, used for frequency referencing and calibration. The small spectral features on the shoulders of the large vapor cell peaks are due to the  $^{113}\text{In}$  isotope (4% abundance) which we account for in our line shape analysis. As noted in the text, the data shown here represent the average of thirty consecutive field off/field on scan pairs.

of “on-off” field for the scalar component. Effectively, we observe the relative Stark shift between distinctive high-field scans, where the frequency shift  $\Delta\nu$  between fields  $\mathcal{E}_1$  and  $\mathcal{E}_2$  is given by  $\Delta\nu = k_{\text{eff}}(\mathcal{E}_2^2 - \mathcal{E}_1^2)$ .

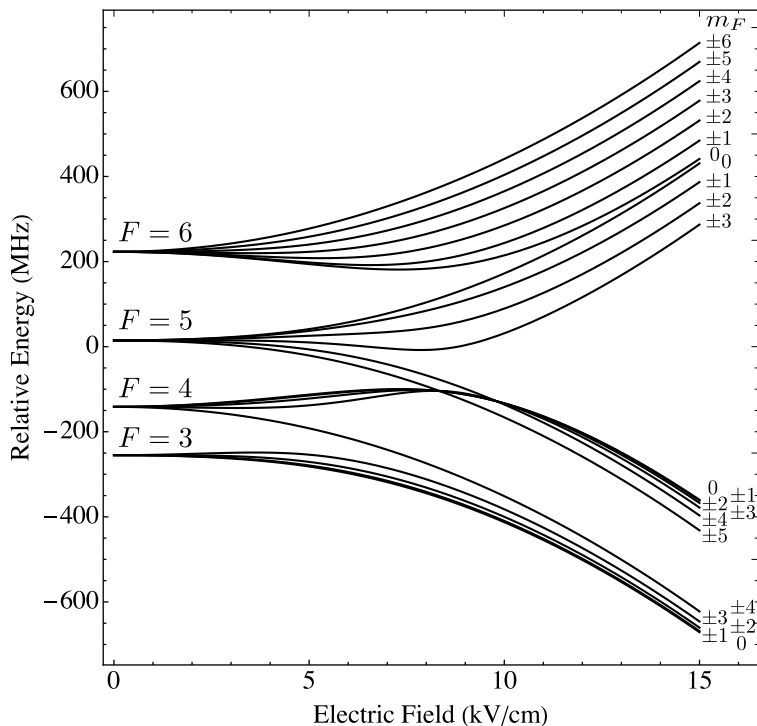


Figure 3.6: Energy eigenvalue structure under applied electric field for all hyperfine sub-levels of the indium  $7P_{3/2}$  state. Here, we again have subtracted out the large scalar shift,  $-\frac{1}{2}\alpha_0\mathcal{E}^2$ , shared by all  $|F, m_F\rangle$  levels for clarity as in Figure 2.3. However, we plot the energy shift against electric field strength instead of electric-field-square, since we physically control the field itself.

### 3.3 Data Analysis

#### 3.3.1 Data Analysis Procedure

Once we have collected desired data under a series of controlled experimental conditions, we use MATLAB software to perform fitting and analysis of the data to extract polarizability values from the raw spectra. First and foremost, since we are interested in shifts in the frequency space, we need to establish a frequency axis and linearize it for every scan using information from the red Fabry-Pérot transmission spectrum. When fitting the Fabry-Pérot data to a sum of Lorentzian peaks,<sup>4</sup> we force every peak separation to be the Fabry-Pérot cavity FSR, which has been calibrated a few times throughout the data acquisition period. The fitted function now becomes an elapsed time-to-frequency mapping that can be applied to all spectra in the same scan, which takes care of the nonlinearity of the red laser behavior

<sup>4</sup>We also explored the approach to fitting the Fabry-Pérot transmission spectra to an Airy function. The two methods yield consistent fitting results.

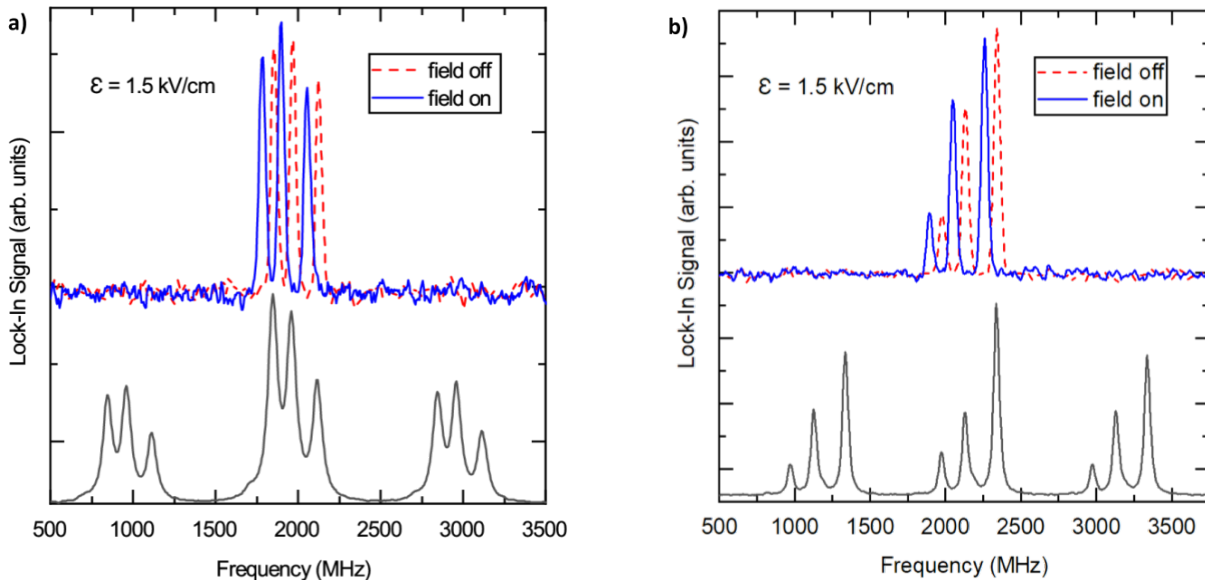


Figure 3.7: Atomic beam spectra for the case of the a)  $(F' = 4) \rightarrow (F'' = 3, 4, 5)$  transitions and b)  $(F' = 5) \rightarrow (F'' = 4, 5, 6)$  of the 685 nm  $6S_{1/2} \rightarrow 7P_{3/2}$  line. The field off spectra (red dashed line) as well as the spectra with a 1.5 kV/cm electric field applied (blue solid line) are shown. Displayed on the bottom of each plot is the corresponding (field-free) vapor cell spectrum, including 1000 MHz FM sidebands, used for frequency referencing and calibration. As in the previous figure, the data shown here represent the average of thirty consecutive field off / field on scan pairs.

at the same time. With the established frequency scale, we then fit the vapor cell spectra to sums of six Lorentzian peaks for the  $7P_{1/2}$  state (to sums of nine Lorentzian peaks for the  $7P_{3/2}$  low field case), corresponding to two (three) hyperfine peaks<sup>5</sup> and four (six) first-order EOM sidebands at  $\pm 1000$  MHz for the  $7P_{1/2}$  ( $7P_{3/2}$ ) state. These EOM sidebands also function as a definitive mechanism of the frequency axis calibration. Following the linearization mapping obtained from the Fabry-Pérot method, the analysis program often outputs a value slightly lower than 1000 MHz, typically  $\sim 998$  MHz, for a sideband's location from the center in the frequency axis. We take the ratio between the observed splittings between hyperfine peaks and their corresponding first-order EOM sidebands to the known modulation frequency of 1000 MHz as a calibration factor. The axis is then scaled by this ratio factor. Likewise, we fit the atomic beam transmission spectra and calibrate by the same scale factor obtained from the vapor cell. We then determine the change in the relative position of the atomic beam spectrum and a reference peak from the calibrated vapor cell spectrum upon application of the electric field to determine the Stark shift. For  $7P_{3/2}$  tensor polarizability scans, which contain no vapor cell signal, we use the frequency

<sup>5</sup>For the  $7P_{3/2}$  case, we can only access three of the four hyperfine levels in a given two-step excitation transition owing to selection rules.

calibration factor from vapor cell data separately taken both immediately before and after these runs.

For scans used to measure  $7P_{1/2}$  and  $7P_{3/2}$  scalar polarizabilities, Stark shifts are extracted from the atomic beam spectra using two independent fitting methods. The first approach, the “Lorentzian method,” is analogous to how we fit the vapor cell spectra. We fit the atomic beam data to sums of two Lorentzian peaks for the  $7P_{1/2}$  hyperfine doublet state or three Lorentzian peaks representing the three out of four excited hyperfine states of the  $7P_{3/2}$  state. The fit outputs the peak locations, amplitudes, and widths. We then find the differences between the resonance locations for field-on and field-off scans. The second approach, the “overlap method,” assumes no functional form of the spectra. Instead, it attempts to find the optimal shifting distance (frequency-axis translation) to overlap the field-on and field-off scans by computing the sum of squared differences between each pair of scans for many possible shifts of the field-on scan. As this value is minimized, the peaks are in fact optimally “overlapped,” and the correspondent shifting distance is the Stark shift. The potential line shape systematic errors to which these two methods are susceptible are quite different. As a result, an agreement in the respective results (as we observe) is a useful indication of the absence of significant systematics of this type.

For the  $7P_{3/2}$  tensor polarizability data taken at higher fields near 15 kV/cm, we observe a more complicated spectrum consisting of clusters of peaks that cannot be well resolved. We observe two well-defined composite peaks (each consisting of several nondegenerate  $m_F$  levels) and an unresolved “plateau”-like feature at higher frequency (see Figure 3.8), just as our simulation predicts, referring to the high-field region of Fig. 3.6. We focus on the two composite peaks of lower frequency for fitting purposes. After truncating the scans to only the two composite peaks of interest, we fit them to sums of two Lorentzian peaks and then calculate the shift of these two peaks between pairs of voltages. It is worth noting that by changing the polarization of two laser beams, we alter the observed spectrum nontrivially since the excitation probability for specific sublevels strongly depend on polarizations. We accordingly perform a subset of high-field regime scans with some particular polarization configurations, in which case we overwhelmingly populate  $m_F$  levels in the middle composite peak in terms of frequency. For these scans, the code simplifies to fitting one single Lorentzian peak. Since no vapor cell signal is generated in this high field regime, we rely on one chosen Fabry-Pérot peak as a stable frequency reference for these high-field regime measurements. We have independently confirmed that the transmission peaks of the passively-stabilized Fabry-Pérot, with its low-expansion-material construction, drift by no more than a few MHz over time scales of one hour. The net Stark shift, extracted from above fittings, can be converted to the  $k_{\text{eff}}$ . When combined with the value of  $k_0$  derived from low-field measurements, this yields a value for  $k_2$ . Numerical modeling allows us to estimate a range of  $c(F, m_F)$  coefficient values for the set of magnetic sub levels contained within each composite peak. Since we cannot predict the exact weightings of the components within the composite peak, we assign a systematic composite line shape error as part of the analysis. By considering all pairs of 14-15-16 kV/cm data scans, and subtracting the known

scalar Stark shift coefficient, we can obtain a final extracted value for  $k_2$ , and hence  $\alpha_2$ . The “overlap method” is not a reliable means of extracting the Stark shift in this case, because the widths, and hence the lineshape, of the composite peaks are expected to change when we apply different voltages. This inconvenience can be explained by the nonuniform shift of each  $m_F$  level in one composite peak. Given the Stark shift differences that we measure at these fields (roughly 500 MHz), any drift-related errors are negligible compared to our final tensor polarizability experimental uncertainty, which, at  $\pm 12\%$ , is much larger than our scalar polarizability uncertainty.

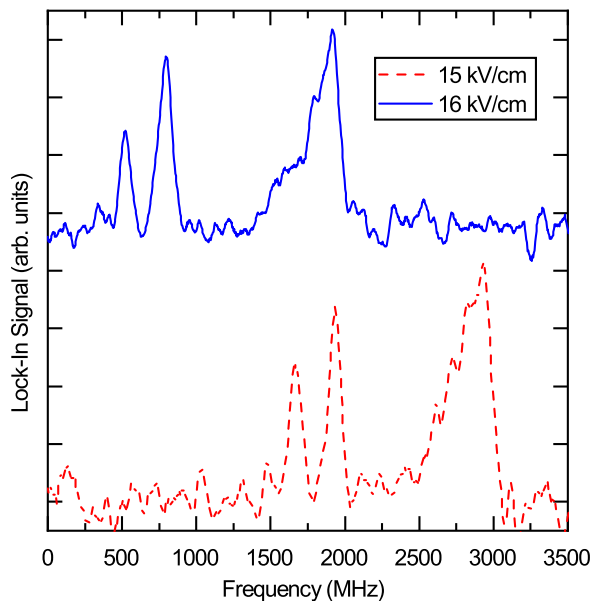


Figure 3.8: For the 685 nm  $6S_{1/2} \rightarrow 7P_{3/2}$  transition, spectra are shown for the case of  $E = 15$  kV/cm and 16 kV/cm, showing a roughly 1 GHz overall Stark shift. For each electric field value, we have averaged a series of scans taken consecutively over a period of 10 minutes for display purposes. Referring to Fig. 3.6, one can see experimental evidence supporting our numerical model, where two relatively sharp experimental peaks are accompanied by a broad composite feature at the higher frequency end of both of the scans shown.

### 3.3.2 Systematic Error Considerations

We consider two categories of error sources: statistical error and systematic error. The statistical error can be directly inferred from the fitting and analysis results, but obtaining a meaningful systematic error bar requires careful design to collect data under various experimental conditions. We take into account all kinds of experimental parameters that could attribute to discrepancy in the measured Stark shift. A considerable number of scans are taken for testing potential systematic error. We categorize the data in various binary ways

based on laser sweep direction, intermediate hyperfine level, order of “field-off” / “field-on” sequencing, spectral peak analysis method. Across these grouped scans, we look for statistically significant differences when one of the above binary parameter is changed. With most varying binary parameters, the subset of scans give rise to results that agree within the statistical uncertainty. Figure 3.9 shows an example comparison among  $k_0$  values obtained from two pairs of binary systematic sources. Occasionally, among some data subsets, these comparisons yield small resolved differences, at the level of more than  $1.5 \sim 2$  standard deviation, in which case we include associated contributions to the total error budget in Table 3.1.

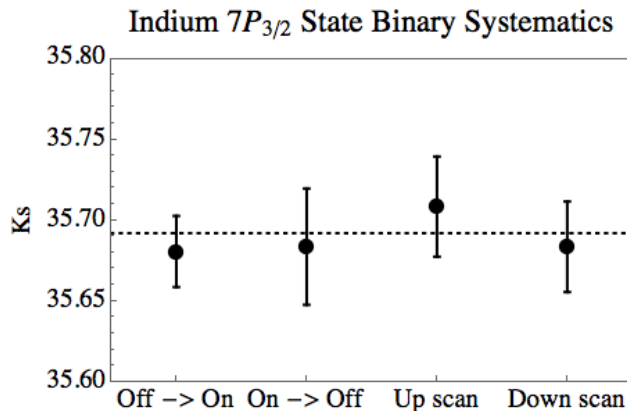


Figure 3.9: The plot shows four  $k_0$  results for the indium  $7P_{3/2}$  state. Each data point represent the weighted average value of a subset of data under the denoted experimental conditions. Here we check that there is no systematic difference in results between the up/down laser scanning direction, nor between the ‘field-off’ / “field-on” sequence when we collect data.

We also consider potential systematic errors by searching for correlations of measured polarizabilities with continuous parameters, such as applied electric field strength and laser power. An example of this is shown in Fig. 3.10b, where all of our  $6S_{1/2} \rightarrow 7P_{1/2}$  Stark shift constant results have been plotted vs. electric field. While, as expected, the *precision* of the polarizability determination is much greater at larger field (where the much larger Stark shift can be measured with much greater fractional accuracy), we see no resolved trend in the central values as the field is varied. We also consider the error contributions from imprecision in the measurement and calibration of the applied electric field, resulted from the uncertainty in the field plate separation as well as the applied voltage. Errors due to the calibration and linearization of the frequency axis are also quantified by fitting Fabry-Pérot and vapor cell spectra using a variety of different methods.

In the case of the  $7P_{3/2}$  scalar polarizability, we have collected data for both the 3-4-5 hyperfine spectra and the 4-5-6 spectra at low fields between 1.5 kV and 3 kV. It is particularly

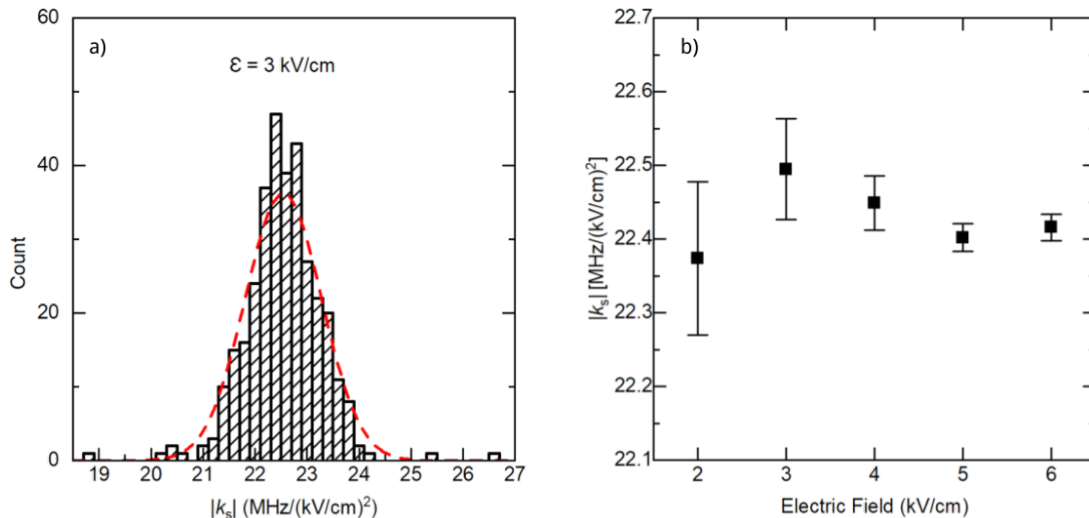


Figure 3.10: a) For the 690 nm  $6S - 7P_{1/2}$  transition, we plot the Stark shift constant derived from roughly 400 field-off / field-on scan pairs taken with  $E = 3 \text{ kV}/\text{cm}$ . A Gaussian curve is laid over the data for display purposes. Central values and standard errors from such analyses complement a weighted average analysis approach to arrive at final statistical averages and uncertainties. b) All  $7P_{1/2}$  Stark shift data, with Stark shift constant plotted versus electric field to explore potential field-dependent systematic errors. An analysis of these data shows the absence of a statistically resolved correlation.

important to study potential field-dependent systematics here, since we know that the tensor component of the polarizability will eventually cause broadening of hyperfine peaks, and differential Stark shift rates as the electric field increases and tensor contributions to the polarizability become significant. Fig. 3.11 a shows the polarizability determinations averaged over hyperfine levels in all of our 4-5-6 spectra for fields between 1 and 3  $\text{kV}/\text{cm}$ , a range over which we expect the tensor contributions to be negligible. Fig. 3.11 b shows the 3  $\text{kV}/\text{cm}$  subset of the data for the  $7P_{3/2}$  scalar polarizability measurement, where we have plotted the Stark shift constant for each hyperfine level individually, now including all four of the hyperfine levels. At this largest field value, we would expect any possible systematic error introduced by tensor polarizability-induced hyperfine line broadening and potential line shape asymmetry to be most noticeable. Similar analyses at all field values, while in some cases revealing variation across hyperfine levels that is slightly in excess of the intrinsic statistical uncertainties (for which we include an additional “hyperfine level dependence” systematic error), show no evidence of the type of tensor polarizability trends predicted for higher fields in Fig. 3.6. Furthermore, as can be seen in that figure, taking the average of all hyperfine Stark shifts at low fields should make us even more immune to any residual tensor effects.

In all cases, contributions from systematic errors remain below the 0.5% level. Varying laser polarizations will also potentially affect spectra peak determination due to changing rates

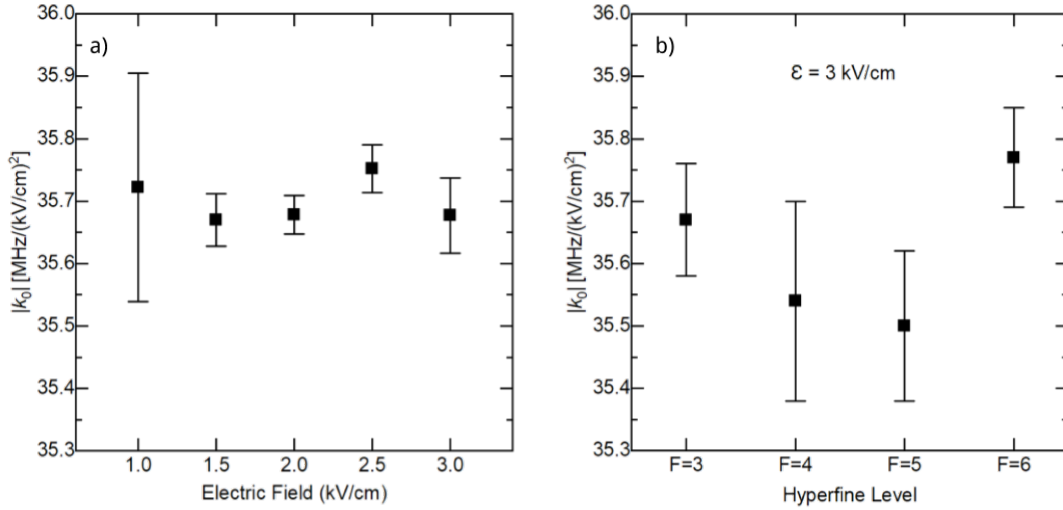


Figure 3.11: a) For the case of all data collected for the transition path  $6S_{1/2}(F' = 5)$  to  $7P_{3/2}(F'' = 4, 5, 6)$ , we average the results of the Stark shift constant for each upper-level hyperfine state, and the resulting average Stark shift constants at each electric field value are plotted. Given that the tensor polarizability is expected to contribute at higher fields, it is notable that over the 1 to 3 kV/cm range shown here we see no statistically significant variation in the measured polarizability. b) At the highest field used, where we expect some hyperfine peak broadening and possible peak asymmetry, we investigate the dependence of the measured Stark shift constant on hyperfine level, now including data taken for each of the four  $7P_{3/2}$ -state sub levels.

of excitation for nondegenerate, unresolved  $m_F$  levels contained in each observed peak, and we have been careful to explore a variety of polarizations for both lasers in our data sets. In Table 3.1 we have included small contributions from this and all other systematic errors that we have considered.

The relative laser polarization between the two lasers significantly affects these high-field spectra, since the excitation probabilities among the various  $7P_{3/2}(F, m_F)$  sub levels is highly sensitive to the polarization selection rules. Thus, we have collected high-field spectra for several choices of polarization, including polarization choices yielding the straightforward “single-peak” spectra that we mentioned earlier. Within the final experimental uncertainty that we quote, we see consistent results across various choices of polarization values. The tensor component for the polarizability for the indium  $7P_{3/2}$  state has the opposite sign from the scalar component, and is more than an order of magnitude smaller. Partly because of its relative size, and partly because of the line shape complications alluded to here, our estimation for  $\alpha_2$  has a limited final fractional uncertainty, which is roughly 12%. Although such a precision is far poorer than all of our recent scalar polarizability measurements, our experimental uncertainty is comparable to the estimated theory uncertainty for the tensor component, and, given these respective uncertainties, is in good agreement with the

|  | $k_0(7P_{1/2} - 6S_{1/2})$ | $k_0(7P_{3/2} - 6S_{1/2})$ | $k_2(7P_{3/2})$ |
|--|----------------------------|----------------------------|-----------------|
| <b>Result</b> [MHz (kV/cm) <sup>-2</sup> ] | -22.402                    | -35.646                    | +1.78           |
| <b>Statistical Error</b>                   | 0.021                      | 0.036                      | 0.09            |
| <b>Systematic Error Sources</b>            |                            |                            |                 |
| Laser scan direction                       | 0.011                      | 0.010                      | 0.05            |
| Frequency calibration                      | 0.004                      | 0.005                      | 0.04            |
| Scan linearization                         | 0.002                      | 0.003                      | 0.003           |
| Electric field calibration                 | 0.022                      | 0.036                      | 0.08            |
| Laser power and polarization               | 0.005                      | 0.006                      | 0.07            |
| First-step hyperfine transition            | 0.033                      | —                          | —               |
| Fitting method                             | 0.018                      | 0.011                      | —               |
| Hyperfine level dependence                 | —                          | 0.050                      | 0.14            |
| Unresolved sub-levels, composite peaks     | —                          | —                          | 0.08            |
| <b>Combined Error Total</b>                | 0.050                      | 0.076                      | 0.23            |

Table 3.1: Final experimental results, with statistical and systematic error contributions, for the Stark shift constants  $k_0$  and  $k_2$  of the  $6S_{1/2} - 7P_{1/2, 3/2}$  transitions in  $^{115}\text{In}$ .

theoretical prediction.

## 3.4 Summary of Results

### 3.4.1 Summary of Indium Polarizability Measurements in 7P Excited States

Over 5000 individual “field-off” / “field-on” pairs of red laser scans were collected for each of the  $6S \rightarrow 7P$  transitions over the time period of several months. In particular, starting from the summer of 2017, we have focused on taking  $7P_{1/2}$  state data along the excitation path that previous thesis work did not get to investigate and complete the systematics check. More importantly, we developed reasonable treatment for the complex spectra of the  $7P_{3/2}$  case and collected abundant data for this state. Over the course of these measurements, in addition to the electric field value, we varied experimental parameters such as the choice of intermediate ( $6S$ ) state hyperfine level, relative optical power and laser polarization, atomic beam source temperature, as well as laser sweep speed and frequency range. In both cases, the frequency axes have been linearized and calibrated using methods described in the Data Analysis section. We extract Stark shifts for each pair of scans of consecutive “field-on” / “field-off” scans; however, for display purposes, in the figures included here, we have averaged the data from 30 consecutive scan pairs taken under identical conditions over the course of roughly 20 minutes.

Table 3.2: Comparison of experimental and theoretical results for In polarizabilities.  $\Delta\alpha_0$  in the third column of results refers to the  $6S - 5P_{1/2}$  polarizability difference. CC  $6S$ ,  $5P_{1/2}$ , and  $6P$  values are from Ref.[15] and the rest of the theoretical values are cited from Ref. [9].

| State                | Theory Method           |                         | Expt.                   |
|----------------------|-------------------------|-------------------------|-------------------------|
|                      | CC                      | CI+all                  |                         |
| $\alpha_0(6S)$       | 1056(27)                | 1055(7)                 | 1050(6)                 |
| $\alpha_0(5P_{1/2})$ | 61.5(5.6)               | 62.5(2.0)               |                         |
| $\Delta\alpha_0$     | 995(28)                 | 992(7)                  | 988.0(2.7)              |
| $\alpha_0(6P_{1/2})$ | 7817(155)               | 7630(120)               | 7590(37)                |
| $\alpha_0(6P_{3/2})$ | 10506(180)              | 10259(230)              |                         |
| $\alpha_2(6P_{3/2})$ | -1432(42)               | -1407(40)               |                         |
| $\alpha_0(7P_{1/2})$ | $1.863(46) \times 10^5$ | $1.823(33) \times 10^5$ | $1.811(04) \times 10^5$ |
| $\alpha_0(7P_{3/2})$ | $2.98(14) \times 10^5$  | $2.87(6) \times 10^5$   | $2.876(06) \times 10^5$ |
| $\alpha_2(7P_{3/2})$ | $-1.75(29) \times 10^4$ | $-1.62(16) \times 10^4$ | $-1.43(18) \times 10^4$ |

We conclude that the (scalar) polarizability for indium  $7P_{1/2}$  state is  $1.811(4) \times 10^5 a_0^3$  in atomic unit. For the more complicated  $7P_{3/2}$  state, we measure the scalar polarizability to be  $2.876(6) \times 10^5 a_0^3$  and the tensor polarizability to be  $-1.43(18) \times 10^4 a_0^3$  (both in atomic unit). These experimental results achieve sub-1% level of uncertainty for the scalar polarizabilities, and approximately 12% uncertainty for the tensor component of the  $7P_{3/2}$  state, all of which provides important benchmarks for future theoretical calculations.

### 3.4.2 Theory Summary

Because of the complexity of indium's trivalent electron configuration, theoretical modeling of such a system is challenging and not as well-developed as that of the single-valence alkali systems. Our high-precision experimental measurements provide new benchmarks to test the *ab initio* atomic theory work in trivalent systems. In specific, our experimental results are used to test two competing theoretical models: the coupled-cluster (CC) approach and the configuration-interaction + all-order (CI+all) method, as mentioned in Section 1.1. The CC model treats the trivalent indium atom as a system with only one valence electron, with the other two valence electrons form a more stable pair. In contrast, the CI+all-order model considers it as a trivalent system, taking both the core-valence correlations and the strong valence-valence correlations into account. Our results presented in this thesis are the first of their kind in highly excited states of trivalent group IIIA atoms, as a valuable addition to our group's previous measurements of polarizabilities in comparatively lower-lying indium states (see Ref. [16] and [20]). Altogether, the comparison between theoretical predictions and our experimental values reveals a trend and helps differentiate between the two models. Below, I summarize the experimental and theoretical values for all indium polarizabilities.

As demonstrated in Table 3.2, the two theoretical approaches agree well within uncertainties for the lower-lying indium states. However, for highly energetic states, these two models yield divergent results. The CI+all model presents values that are in better agreement with our experimental measurements for the  $6P$  and  $7P$  excited states. A more straightforward visual comparison between these two theoretical models' predictions alongside our experimental values is presented in Figure 3.12.

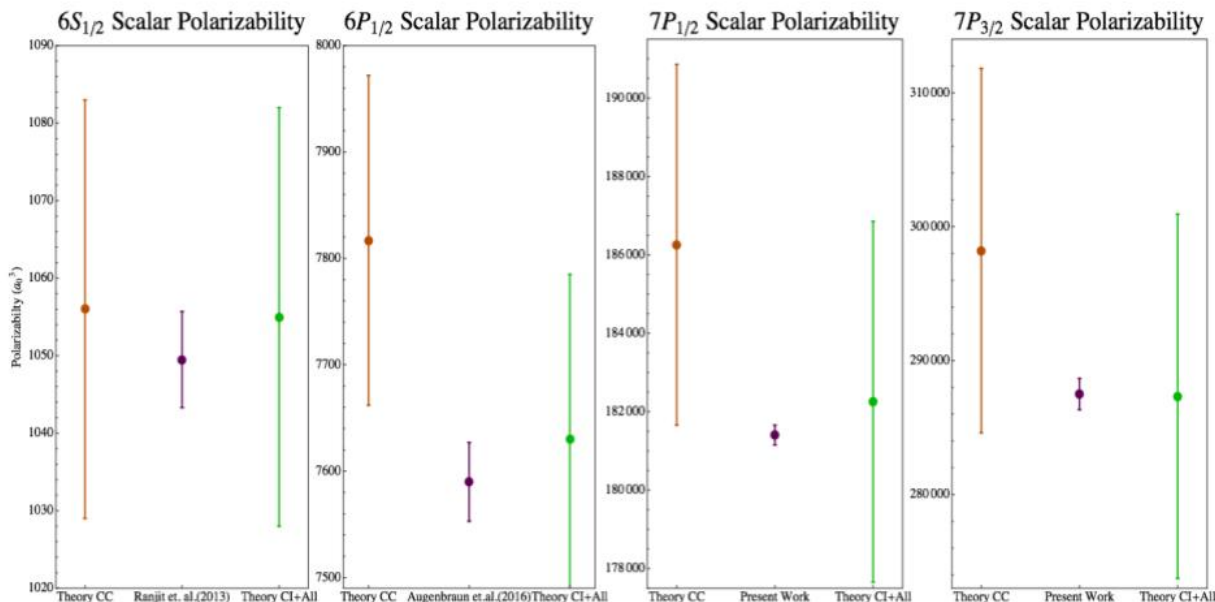


Figure 3.12: Summary of our experimental values for indium polarizabilities in the  $6S_{1/2}$ ,  $6P_{1/2}$ ,  $7P_{1/2}$ , and  $7P_{3/2}$  excited states, in comparison with the theoretical calculations using two distinct models for each state. The yellow data points show polarizability values calculated using the CC model, while the green data points are predictions from the CI+all-order approach. The middle purple data point in each plot is our experimental result.

Recall that the polarizability of a particular excited state is an infinite sum of contributions from all other states (Equation 2.20 and 2.21). Among all states, the  $7P \rightarrow 6D$  contribution is strongly dominant, giving 97% for both  $7P$  scalar polarizabilities, as listed in Ref. [9]. Such dominance is a result of the large matrix elements and very small energy differences associated with the  $7P-6D$  terms. Within the infinite sums that make up the polarizabilities, we can make a straightforward determination of these particular matrix elements using our experimental values and the known energy splittings. By subtracting from our experimental polarizability value the residual terms of the theoretical sum (which in total represent only a few percent of the net polarizability), we can isolate the dominant term in the sum, and then compute a recommended value for the particular matrix element of interest. A similar procedure was undertaken for the case of the  $6P-5D$  matrix element in Ref. [20]. From the

precise polarizability measurements of indium 7P states, we infer the values for two indium reduced matrix elements ( $\langle 6D_{3/2} || D || 7P_{1/2} \rangle$  and  $\langle 6D_{5/2} || D || 7P_{3/2} \rangle$ ), as presented alongside the theoretical predictions of these two quantities in Table 3.3. We see better agreement between our experimental results and the corresponding CI+all entries for these two reduced matrix elements.

Table 3.3: Comparison of experimental and theoretical results of the absolute values of reduced matrix elements (in atomic unit) of the leading contributor to the polarizabilities of the  $7P_{1/2}$ , and the  $7P_{3/2}$  states in indium.

| Reduced Matrix Element                      | Theory Method |           | Expt.     |
|---|---------------|-----------|-----------|
|   | CC            | CI+all    |           |
| $\langle 6D_{3/2}    D    7P_{1/2} \rangle$ | 21.50(27)     | 21.24(20) | 21.17(04) |
| $\langle 6D_{5/2}    D    7P_{3/2} \rangle$ | 29.07(80)     | 28.46     | 28.49(11) |

In conclusion, we have completed new high-precision measurements of polarizabilities in the highly excited 7P states of  $^{115}\text{In}$ . By combining the present polarizability measurements with recent ones in lower-lying states of indium, we have proven the value of such experimental benchmarks in guiding theoretical work forward via their ability to discern between competing theoretical models. The experimental values for the 6P and 7P states are clearly in better agreement with the CI+all-order calculations that treat indium, a group IIIA element, as a three-electron system with configuration mixing. In this sense, our experimental work aids the ongoing development of theory necessary for robust tests of fundamental physics in these trivalent systems.

# Chapter 4

## Lead E2 Transition Amplitude Measurements: Apparatus and Experiment Techniques

This section first describes the apparatus and optical design for measuring the ratio of the M1 and E2 transition amplitudes in a lead vapor cell, then expands upon the key technique involved in this experiment, Faraday rotation spectroscopy. Figure 4.1 provides an overview of the experimental setup, with some apparatus components omitted for clarity. We use shutters to alternately block and unblock two lasers, properly tuned to scan smoothly across the M1 and E2 transition resonances respectively. The laser radiation drives ground state lead atoms to their excited states through the M1 or the E2 path. The lead atoms are contained in a vapor cell located in our oven system, which will be discussed in detail below. We apply an external magnetic field to induce the Zeeman effect in the atoms, producing optical rotation in the lead cell so that we can perform Faraday rotation spectroscopy, which is discussed in Section 4.2. Further modulation and demodulation mechanisms allow us to acquire the tiny Faraday rotation signal, detected by two photoreceivers, with superb signal-to-noise ratio. In the following subsections, I will highlight a few core components in the apparatus setup and explain the Faraday rotation spectroscopy method in depth.

### 4.1 Experimental Setup

#### 4.1.1 Lead Vapor Cell in an Oven System

The atomic source in this experiment is a lead vapor cell heated up to near 1000 °C. The vapor cell, containing nearly pure  $^{208}\text{Pb}$ , is made of quartz with wedged windows for the purpose of eliminating reflection and interference. The cell is placed in our oven system,

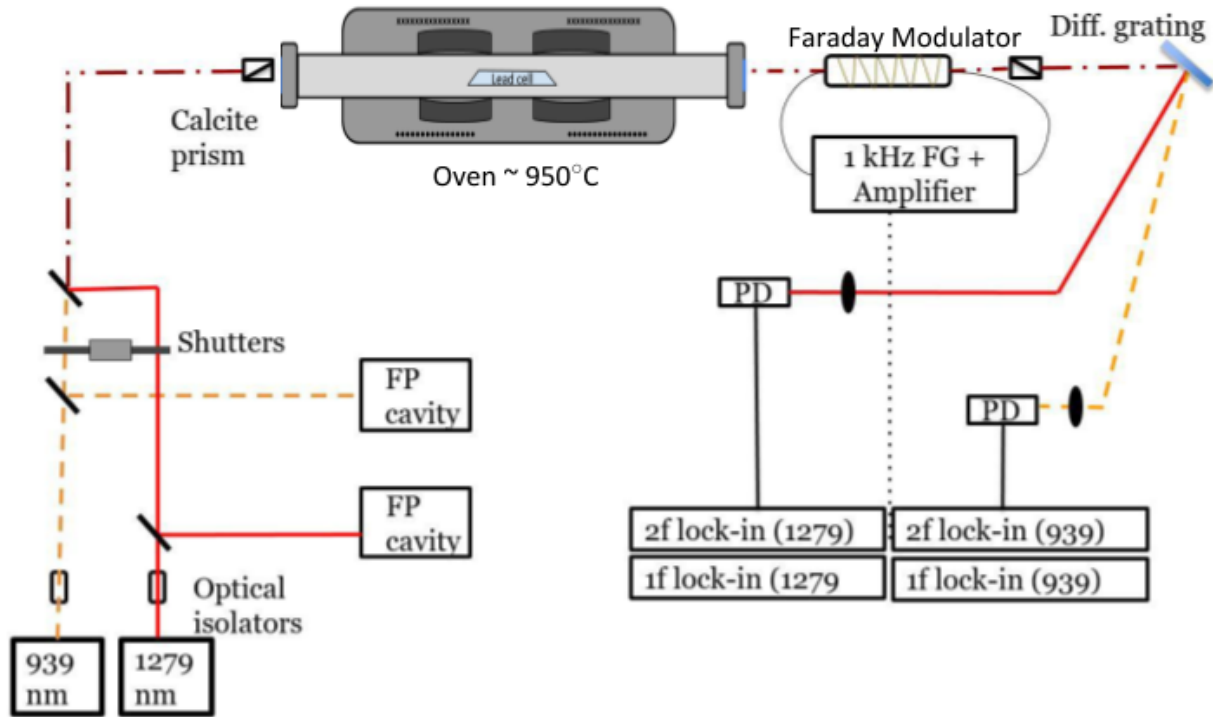


Figure 4.1: The experimental layout of the lead transition amplitudes measurements.

which provides heating and generates a magnetic field using a set of Helmholtz coils. Figure 4.2 demonstrates the oven system's structure from a cross sectional view and Figure 4.3 alternatively provides a top view. Our heating unit consists of four clamshell heaters, each powered by an audio amplifier (GTD audio T-8500). We use a function generator to drive the audio amplifiers at a high frequency. We design such a setup to generate heating current so that we avoid 60 Hz noise from a wall source (such as a Variac transformer directly connected to the wall outlet) in our sensitive Faraday rotation signal. We set the function generator at  $\sim 10$  kHz, a frequency far removed from the signal modulation frequency.

At each end of the six-inch lead cell, a pair of clamshell heaters hug the inner cylinder, which is in direct contact to the cell. Each pair of heaters spatially overlaps with the cell for 2 inches, leaving the middle 2 inches of the cell not directly surrounded by any heating element. Such a spatial design minimizes the temperature gradient throughout the vapor cell. It is also crucial to match the output power from the four amplifiers to diminish effects from uneven heating. We monitor and record the cell's temperature both at one end *and* in the middle of the cell with two thermocouples. The real-time temperature data are fed into our temperature PID control program written in Python, which sets the function generator's output voltage and thus controlling the output power, so that the temperature reaches and stably maintains equilibrium at the desired value. Over time, we achieve consistent readings from the two thermocouples to sub- $1^\circ\text{C}$  level, as Figure 4.4 demonstrates. Efforts to minimize the temperature gradient over the length of the lead cell are of great importance, because

our derivation of lineshapes is based on the assumption that the atoms in the cell are at a single fixed temperature. Such a precise knowledge of the temperature is also critical for data analysis, since by knowing the temperature, we can determine the Gaussian width, leaving only one unknown parameter, the Lorentz width, to be characterized in the complicated Voigt profile.

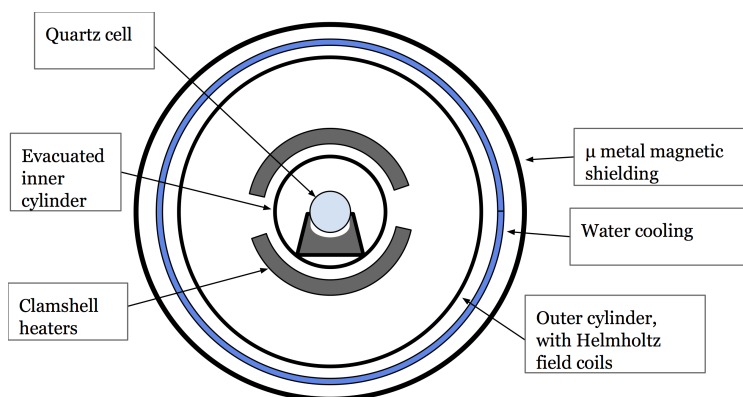


Figure 4.2: A cross-sectional view of the oven system for the lead transition amplitude measurement experiment.

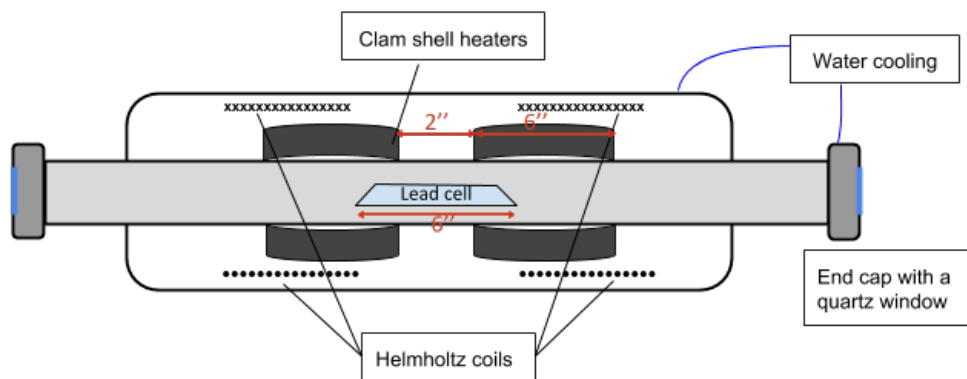


Figure 4.3: Oven setup schematics viewed from the top. The spatial configuration of the heaters and the cell is illustrated.

The applied magnetic field causes the Faraday rotations and it is vital that we have good control over the B field strength applied to the lead atomic system. For this reason, the outermost layer of the oven system is a double-layer  $\mu$  metal shield, ideally canceling, at least effectively extenuating, the Earth magnetic field's influence.<sup>1</sup> Inside the shield resides an outer aluminum cylinder wrapped by coils in a Helmholtz configuration, which produce

<sup>1</sup>The current orientation of the magnetic shielding does not perfectly align with the Earth field due to spatial limits. In the new lab, we should ensure the oven to be parallel with the local Earth field direction.

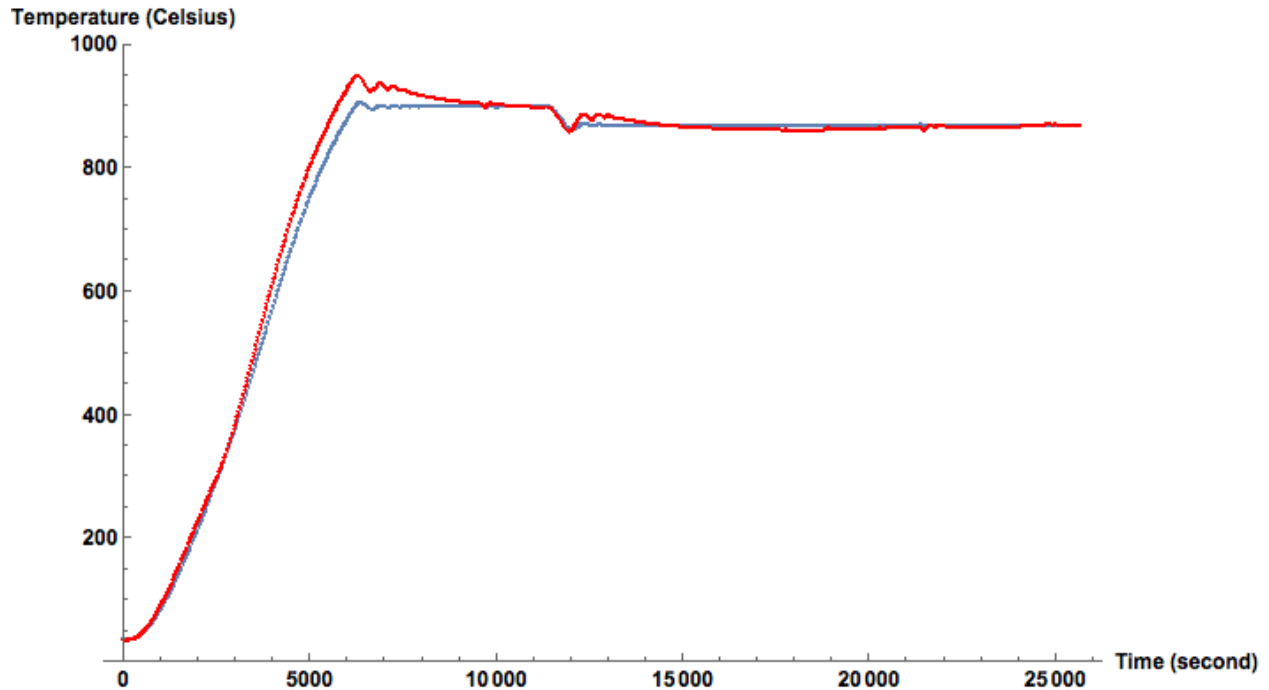


Figure 4.4: Typical temperature data from the two thermocouples over the course of a day starting from room temperature. On this particular day, the first target temperature in PID program is set to be 900°C (represented by the first converging range around 10,000 seconds), and then we lower the target temperature to 870°C to take different data sets at a lower temperature (represented by the second converging phase after 22,000 seconds).

a stable and approximately uniform magnetic field in the middle region between the coils.<sup>2</sup> At room temperature, we probe the magnetic field inside the cylinder with a 3-axis magnetometer to characterize the field strength around the cell's location. In the current operating range (1 ~ 4 A), we find the transverse field inside the Helmholtz coils to be negligible in comparison with the longitudinal field (we denote as  $\hat{z}$ -axis), and the field is close enough to a uniform static field over the length of our cell. It is worth noting that the magnetic properties of metals (mostly Ni) in the oven system change as it gets heated beyond their Curie temperature.<sup>3</sup> Therefore, we cannot quantitatively characterize the applied magnetic field at high temperatures, nor can we establish a correspondence between the magnetic field strength and the applied current in the Helmholtz coil. The good news is that since we only need to extract the ratio between two transitions, we just need to ensure that the applied magnetic field stays the same for the two transitions.

We run water cooling through the oven system to protect the  $\mu$ -metal shield as well as the coils generating magnetic field. The lead cell is housed in another inner cylinder supported

<sup>2</sup>Ultimately, we do not require the external magnetic field to be uniform across the cell, but need the field integrated over the cell length to be constant.

<sup>3</sup>Our operation temperature exceeds Ni's Curie (358°C) temperature by far.

in the center of the cylinder by stuffed fibre glass insulation. The inner ceramic cylinder is evacuated to a modest vacuum  $\sim 2$  Torr and then back-filled with argon. The motivations behind this procedure are twofold. First, we are concerned with possible distortion of the incoming laser light when it interacts with moving air due to changes in the refractive index. Second, we hope to mitigate convection currents in the cylinder by stabilizing the pressure with an inert gas. The inner cylinder is longer than the rest of system so that we can seal the ends of this component with special end caps, with embedded quartz windows letting light pass through. Concerned about thermal expansion of the end cap windows changing their refraction index, we extend the water cooling system to the two end caps.<sup>4</sup>

### 4.1.2 Lasers and Optics

Like the lasers used in the indium experiment, both lasers involved in this experiment are ECDLs in the Littrow configuration. The 940 nm home-built laser corresponds to the resonant frequency of the E2 transition, while the 1279 nm commercial laser (Sacher Lasertechnik Lynx) drives the M1 transition. We achieve a scanning range of a few GHz void of mode-hopping via PZT control and a feed-forward system, which applies current correction to the laser as we scan the PZT. One drawback of the feed-forward system is that it introduces a background slope to our transmission spectra, which needs to be taken into account when we analyze the transmission spectra. As Ref. [21] shows, we can ignore short-term laser drift and intrinsic noise for our typical scan period of  $\sim 10$  s.

A portion of each laser beam passes through a Fabry-Pérot cavity for frequency calibration, just as in the indium experiment. Since the aim of this experiment is to find the ratio between two transition amplitudes, it is necessary that we control all experimental conditions when measuring the two distinct transitions. In practice, we overlap two laser beams through the lead vapor cell and alternate them in rapid succession using a pair of shutters, in order to achieve almost identical experimental conditions. The near-resonant laser radiation is directed to pass through the polarimeter system containing the vapor cell. In the polarimeter system, we apply a magnetic field and induce Faraday rotation, which will be discussed in detail in the next section. A diffraction grating differentiates the transmitted light by wavelength, so that we not only get rid of ambient black body radiation, but also separate the light paths of the two laser beams. Each laser beam is collected by a photoreceiver with appropriate wavelength range (we use a ThorLabs PDA 100A Si photodetector for the 940 nm light and a home-built high sensitive photo receiver for the 1279 nm light, whose circuit design is adapted from Ref. [22]).

---

<sup>4</sup>We also water cool the Faraday rod, introduced in Section 4.2, which is wrapped around by coils that produce heat when current goes through.

## 4.2 Polarimeters and Faraday Rotation Technique

The extremely weak E2 transition that we aim to measure demands a highly sensitive signal detection method. Our strategy is to employ the Faraday rotation technique in the polarimeter system, which enables us to resolve rotations of light down to  $\mu\text{rad}$  level. Imagine that we pass light through two completely crossed polarizers. Then, if we rock the light's polarization back and forth by a small amount, the portion of light with slightly rotated polarization will escape and be detected.

In our experiment, we place a lead vapor cell between two crossed polarizers, made of Glan-Thompson prisms. Unlike an ideal pair of crossed polarizers that blocks 100% of light, in reality, our polarizers have a finite extinction ratio below  $\sim 10^{-6}$  with no additional optics in between. For the current optical setup, we actually measure a finite extinction ratio of order  $\sim 10^{-5}$  with the quartz windows on the end caps as well as the cell in between. This finite extinction ratio can be understood as an effective uncrossing angle  $\phi_0$  between two polarizers, as we recall the transmitted intensity after two polarizers is

$$I = I_0 \sin^2(\phi_0) \approx I_0 \phi_0^2, \quad (4.1)$$

where we take small angle approximation for  $\phi_0^2 < 10^{-5}$ . Under an applied magnetic field, the induced optical rotation in the lead cell would cause a tiny rotation  $\phi_{Pb}$  in the incoming light's polarization and enable a small amount of rotated light to transmit through the cell. The rotation angle  $\phi$  is usually below  $10^{-2}$  rad, too small to be directly detected via direct transmission. We apply a common device in spectroscopy, lock-in detection, to extract a meaningful transmission spectrum from a noisy background. To do so, we insert a Faraday modulator between the two prisms, as Figure 4.5 shows. The Faraday modulator is a 5-cm-long optically active cylinder, made of Hoya FR5 glass, residing in a solenoid. When we apply an alternating current to the solenoid, it generates an oscillating magnetic field at frequency  $\omega$  (typically 1 kHz). The modulator alters the light's polarization by approximately 1-10 mrad ( $\phi_{mod}$ ), contributing to the total rotation  $\phi_{total} = \phi_{Pb} + \phi_{mod} \cos(\omega t)$ . Then the

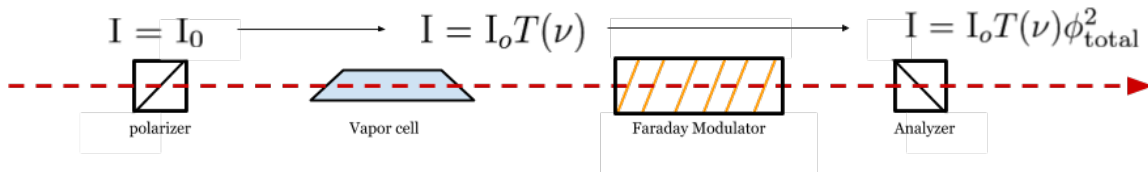


Figure 4.5: Schematic of our Faraday rotation technique. Two Glan-Thompson prisms are labeled as the polarizer and the analyzer, between which are the lead vapor cell and the Faraday modulator. The transmitted laser intensity after each step is indicated above individual components.  $T(\nu)$  represents the transmission profile through the lead cell.

transmitted intensity of laser light after the Faraday rotation unit is:

$$I(\nu) = I_0(\nu) \left[ \phi_{pb} + \phi_{mod} \cos(\omega t) \right]^2 + I_0(\nu) \phi_0^2, \quad (4.2)$$

where  $\nu$  is the frequency of light. We notice that the finite extinction term is a constant DC background, independent of the frequency. Therefore, after lock-in modulation, this term will be filtered out together with noise. Then, the post Faraday rotation light intensity can be simplified as

$$I(\nu) = I_0 T(\nu) \left[ 2\phi_{mod}\phi_{pb} \cos(\omega t) + \frac{1}{2}\phi_{mod}^2 \cos(2\omega t) + \phi_{pb}^2 + \frac{1}{2}\phi_{mod}^2 \right], \quad (4.3)$$

where we rewrite  $I_0(\nu) = I_0 T(\nu)$  to highlight the transmission profile  $T(\nu)$ . Our lock-in modulation picks out the AC terms and we demodulate at the first two harmonics  $\omega$  and  $2\omega$ , outputting what we call  $1f$  and  $2f$  signals respectively:

$$\begin{aligned} 1f &: 2I_o T(\nu) \phi_{mod} \phi_{pb} \\ 2f &: \frac{1}{2} I_o T(\nu) \phi_{mod}^2. \end{aligned} \quad (4.4)$$

The  $1f$  term is proportional to both the transmission profile and the optical rotation in lead, while the  $2f$  term only depends on the transmission  $T(\nu)$ . Dividing the  $1f$  signal by the  $2f$  signal, the obtained quotient  $4\phi_{mod}^{-1}\phi_{pb}$  simply scales with the atom-induced optical rotation. From this modulation-demodulation scheme, we extract the optical rotation associated with lead cells, from which the matrix elements could be inferred as demonstrated in Section 2.3. Our Faraday rotation technique yields absorption spectra ( $2f$  signal) and Faraday rotation spectra ( $1f$  signal) with superb signal-to-noise ratio, as we will see in chapter 5.

# Chapter 5

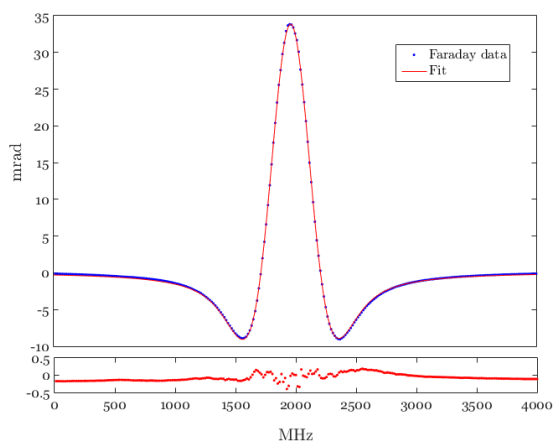
## Lead E2 Transition Amplitude Measurements: Data Analysis and Preliminary Results

Before taking a large amount of data for both the M1 and E2 transitions and obtaining the ratio between the two transition amplitudes, more preparatory work is necessary to establish a robust fitting routine of the collected Faraday rotation and transmission spectra. Below we outline the data analysis scheme and highlight our approach to fitting the convoluted lineshapes.

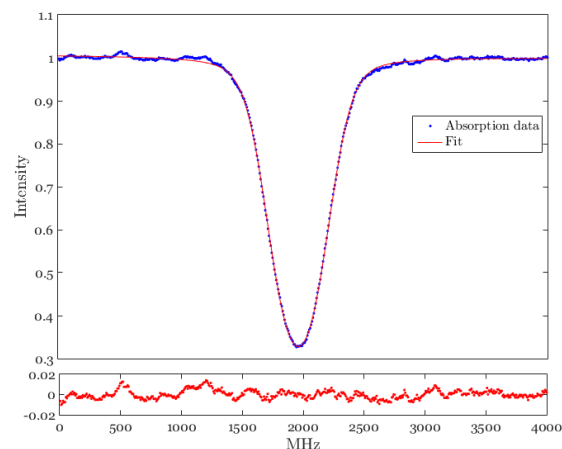
### 5.1 Data Acquisition Scheme

We use an automated program written in LabVIEW to carry out our data collection process. Similar to our data collection scheme for the indium polarizability experiment, the program controls two shutters placed in the two distinct laser beam paths to alternatively drive the two transitions in the lead cell. We drive the M1 and E2 transitions in rapid successions, as a way of minimizing changes in the controlled experimental conditions. The LabVIEW program also controls the presence and strength of a current source responsible for generating the external magnetic field. As a result, we acquire spectra with the magnetic field on and off, and thus with and without atomic optical rotation, for both M1 and E2 transitions with the ECDLs scanning across the resonant frequencies. For each individual scan, we record four categories of spectra: the voltage ramp driving the scanning laser, the Fabry-Pérot transmission signal, the lock-in 1f signal, and the 2f signal which we introduced in Equation 4.4. The lock-in demodulated 1f and the 2f signals represent the Faraday rotation spectrum and the direct transmission spectrum respectively. Figures 5.1 and 5.2 showcase the absorption and the Faraday rotation spectra we acquire in a typical scan, whose characteristic

lineshapes agree with our theoretical predictions, as discussed in Section 2.3. For the E2 transition case, we still collect the almost trivial 2f signal. Even though it offers little information about the transition itself, it reflects the laser power fluctuation and real-time noise behavior.

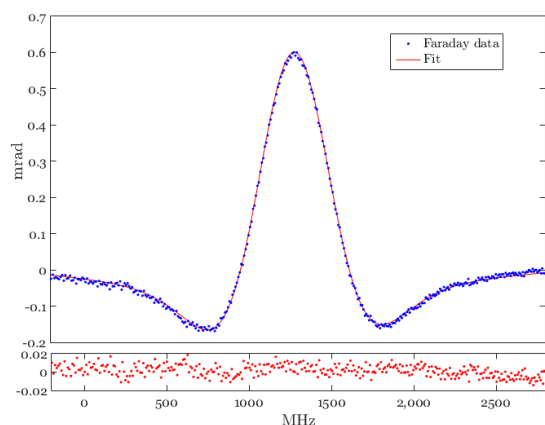


(a) Faraday spectrum for the M1 transition with fit residuals. (1f lock-in signal)

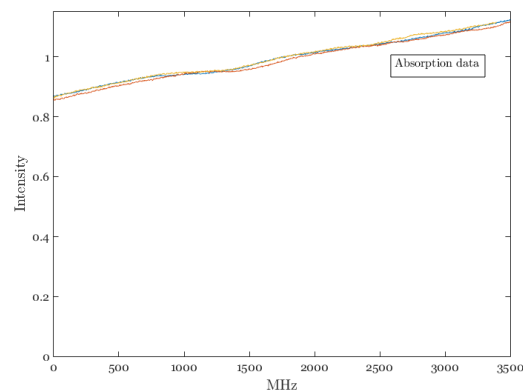


(b) Absorption spectrum for the M1 transition with fit residuals. (2f lock-in signal)

Figure 5.1: Representative spectra from the M1 transition. Note that the y-axis scales are different for each spectrum.



(a) Faraday spectrum for the E2 transition, with fit residuals. (1f lock-in signal)



(b) Absorption spectrum for the E2 transition. Here we show three scans overlapped. (2f lock-in signal)

Figure 5.2: Representative spectra from the E2 transition. Note that figure (a) shows only one scan, whereas figure (b) shows the signal from three, in order to distinguish noise from overall trends.

We are near but not quite at the stage of data collection, as we still try to improve our data analysis procedure, especially the spectra fitting process. To aid the process of analysis program development, we first took some preliminary data of the E2 transition at various temperatures magnetic field strengths. These data sets may not directly contribute to the transition amplitude ratio measurement, but proved crucial for polishing and modifying the data analysis method.

## 5.2 Improving Data Analysis Method

As previously mentioned, extracting precise information from our complex spectra demands a reliable fitting routine to extract both the Lorentzian width and the Doppler width from the transmission Voigt profile (2f signal) or the convoluted Faraday rotation signal (1f signal). The interplay between the two width parameters is not only intricate, but also sensitive to the initial guesses given to the analysis procedure, posing challenges to the process of fitting convoluted lineshapes. We have developed a new analysis method, specifically tackling the width parameter fitting challenge. In this section, we first overview the data analysis procedure for ultimately calculating the amplitude ratio, and then focus on our analysis effort in fitting the complicated spectral lines with floating Gaussian width  $\Gamma_D$  and Lorentzian width  $\gamma$ .

### 5.2.1 Analysis Routine Outline

We hope to develop two sets of data analysis routine in parallel. The first analysis method, written in MATLAB, consists of three sequential steps: normalization, calibration, and line-shape fitting, following the legacy of Eli Hoenig's thesis work [6]. The specific steps in our MATLAB analysis routine will not be extensively described here, but I highlight the essential ideas behind the method. We first linearize the frequency axis using the Fabry-Pérot transmission just as in the indium experiment. Although our goal in this experiment to extract the spectral peak's amplitude, the linearization and frequency calibration process necessitates the subsequent fitting procedure as the convoluted curves are frequency dependent and the laser behavior also relates to frequency. We then use the byproduct of the linearization step, the data-point-to-frequency mapping, to convert the collected spectra to frequency space. We fit the spectra to convoluted functions and extract the height of the spectral peaks. The critical curve-fitting step dictates the accuracy and precision of our results, so we devote much effort to the refinement of our fitting scheme, as discussed in the next section. Referring to Equation 4.4, the quotient of the Faraday rotation signal (1f lock-in output) and the transmission (2f lock-in output) is directly proportional to the optical rotation angle in lead. We thus divide the Faraday rotation spectrum by the normalized transmission spectrum of the same scan. To extract a meaningful amplitude ratio between the M1 scans and the E2 scans, we need an additional calibration step to correctly convert

the observed voltage to the physical rotation angle. Lastly, we calculate the measured peak amplitude ratio between the two transitions and apply the conversion relationship stated in Section 2.3 to obtain the ratio of the reduced matrix elements for the two transitions.

On the other hand, a new analysis approach written in Python is under development, whose main goal at the current stage is to explore various parameter spaces and develop a robust fitting program for the convoluted lineshapes. Eventually, we will develop a complete analysis program in Python, independent from the MATLAB one. Given the complexity of the convoluted spectral lineshapes, the consistency between these two fitting schemes would grant us more confidence in our results. If any significant disagreement between the two analysis schemes arises, we would further investigate into the analysis methodology and possibly quote a systematic error in terms of analysis methods.

Our curve-fitting procedure in Python first linearizes the data using the Fabry-Pérot transmissions and then fits the data to a convoluted function with initial guesses we calculate from observable experimental conditions. For the Faraday rotation spectra, we find that the empirical asymmetries in the two “troughs” on each side of the spectral peak of the observed Faraday rotation lineshape, convoluted by the Doppler effect (as shown in Figure 5.2a), influence the width parameters of the fitted curve significantly. Susceptible to the random background noise, the shape and position of the “troughs” could detrimentally skew our fitting result. As a solution, we average four runs of collected Faraday rotation signal so that the relative size of the random noise is scaled down. Features of the expected lineshape as shown in our simulation (Figure 2.7) are more pronounced in the averaged Faraday rotation signal, and thus, its fitted curve tend to yield more reliable results than that from one individual scan. This averaging process relies on aligning the raw data in the frequency axis and the Fabry-Pérot transmission signal provides a countable ruler for the frequency. We pick out the second Fabry-Pérot peak in each scan and shift every spectra accordingly. Then, we perform the linearization procedure on the overlapped average Fabry-Pérot spectrum. Figure 5.3 visually demonstrates this process of averaging four Fabry-Pérot traces, aligning in the frequency axis, and finally linearizing the frequency based on the Fabry-Pérot cavity’s FSR (free spectral range).

The linearized Fabry-Pérot spectrum (average of four traces) then functions as the frequency reference for each collection of four data scans. We overlay the lock-in outputs and linearize the data points using the calibrated Fabry-Pérot transmission. We then fit the averaged 1f and 2f spectra numerically to the convoluted functions. While the 1f spectrum, the convoluted Faraday rotation signal, corresponds to the functional form in Equation 2.51, the 2f spectrum, the broadened transmission signal, corresponds to the Voigt profile introduced in Section 2.1.3. The lacking of a analytical solution to either spectral lineshape makes the numerical fitting procedure highly sensitive to initial guesses and parameter boundaries. The next section dedicates to explaining our strategy to treat such a complex lineshape.

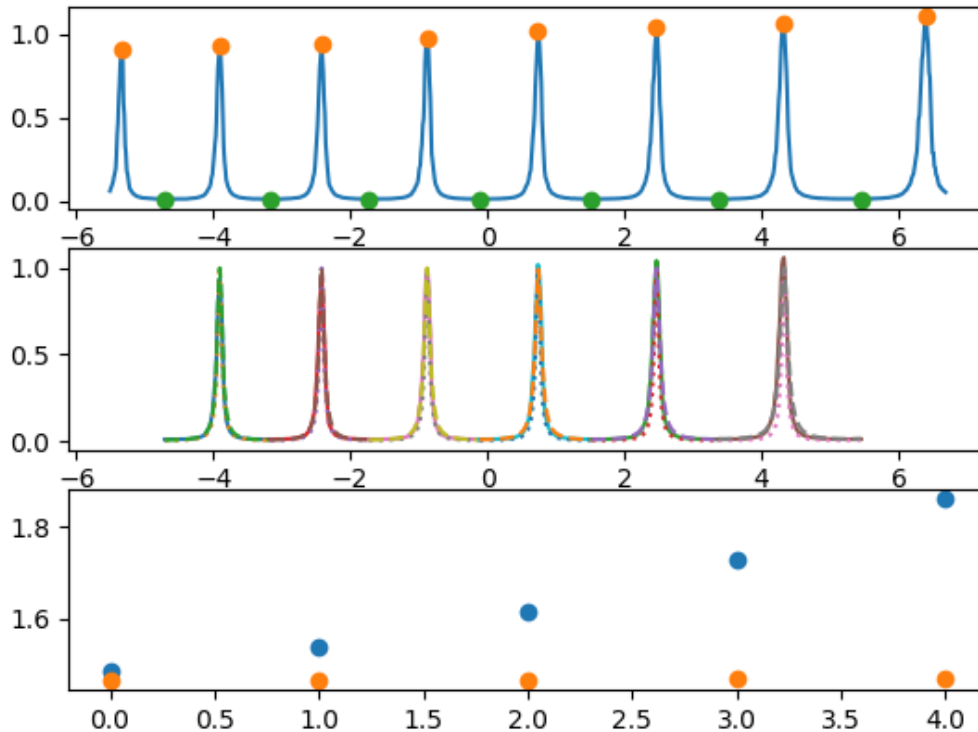


Figure 5.3: Top panel shows a raw Fabry-Perot transmission signal from one of the four traces taken. The middle panel fits to each Fabry-Perot peak overlaid with each peak, and the bottom panel plots the differences between each peak before (blue points) and after (orange points) linearization.

### 5.2.2 Fitting Convolved Lineshape and Extracting Width Parameters

For the purpose of exploring the lineshape fitting scheme, the M1 transition is an ideal candidate, as it provides useful information from both transmission and Faraday rotation spectra. It would be reassuring to test the consistency between the width parameters yielded from fitting these two distinct lineshapes. Yet, the 1279 nm commercial laser driving the M1 transition has unfortunately been out of commission by the time this thesis is written. Limited by the time frame required to fix the 1279 nm laser by technicians, we opt to first exploit the E2 transition alone as a means of gaining insight of the complicated Faraday rotation lineshape and developing our analysis program. The E2 transition alone also suffices the purpose of investigating the temperature stability of the oven system and the atomic behavior under different magnetic fields.

In contrast to the M1 transition, the weaker E2 transmission does not offer any reference knowledge due to the “invisibility” of its direct absorption. Confined to a single Faraday rotation spectrum (1f signal) from every scan, we face an analysis challenge because of the complexity and uncertainty in components of the Faraday rotation function convoluted by the Doppler broadening. While fitting the complicated lineshape poses difficulties initially, resolving the challenge would ease the rest of our analysis process. In order to pin down the unknown fitting parameters in the complicated 1f output, we try to make educated guesses and put constraints on these parameters based on measurable quantities.

Recalling the functional forms of the two width parameters  $\Gamma_D$  (see Equation 2.6) and  $\gamma$  (the collisional width, see Equation 2.11), they both depend on the temperature. It is for this exact reason that we put great effort to achieve a sub-1 °C temperature control throughout the cell. Knowing the temperature, the Doppler width  $\Gamma_D$  is straightforwardly estimated since it does not depend on any other unknown. For the case of Lorentzian width  $\gamma$ , overwhelmingly dominated by the collisional broadening width, three undetermined factors participate in the equation: the temperature  $T$ , the vapor pressure  $p_v$ , and the collisional cross section  $\sigma_b$ . The vapor pressure  $p_v$  is also temperature-dependent and can be readily estimated,<sup>1</sup> leaving only one parameter to be determined,  $\sigma_b$ . The kinetics of collisions is rather complicated and few experiments have been conducted to measure the lead-lead collisional cross section. A rough estimation of  $\sigma_b$  based on the mean free path between lead atoms at around 950 °C and the number density puts its order of magnitude to a few hundred or a thousand Å. In the fitting procedure, we place strict constraints on the temperature while allow the cross section  $\sigma_b$  to vary in a much more tolerating range. Starting from the educated initial guesses with proper bounds, the program proceeds to numerically fit the data to the Faraday rotation equation convoluted by a Gaussian distribution (Equation 2.51) and minimize the  $\chi^2$  to find the optimized combination of parameters. Figure 5.4 shows the typical 1f and 2f signals and the fitted curve.

### 5.3 Preliminary E2 Fitting Results and Systematics

In comparison to the Lorentzian width  $\gamma$ , the Doppler width  $\Gamma_D$  simply depends on the temperature as Equation 2.6 explicitly demonstrates. Hence, it is worth checking first whether the fitted Doppler width scales with  $\sqrt{T}$  as expected according to the Maxwell-Boltzmann distribution. We collected near 500 scans of the E2 transition at a series of temperatures, ranging from 810 °C to 990 °C. Figure 5.5 plots the extracted Doppler widths against the temperature and we can see the found Doppler widths depend on the temperature as predicted up to a scaling factor. For the case of the Lorentzian width  $\gamma$ , its relationship with temperature  $T$ , counting both the direct dependence and the indirect connection through the temperature-dependent vapor pressure, is shown in Figure 5.6 alongside the extracted

---

<sup>1</sup>For lead liquid (the lead sample will first melt and then vaporize during the heating process), the vapor pressure formula is  $p/\text{Pa} = 10^{4.911-9701/T}$ , citing Ref. [23].

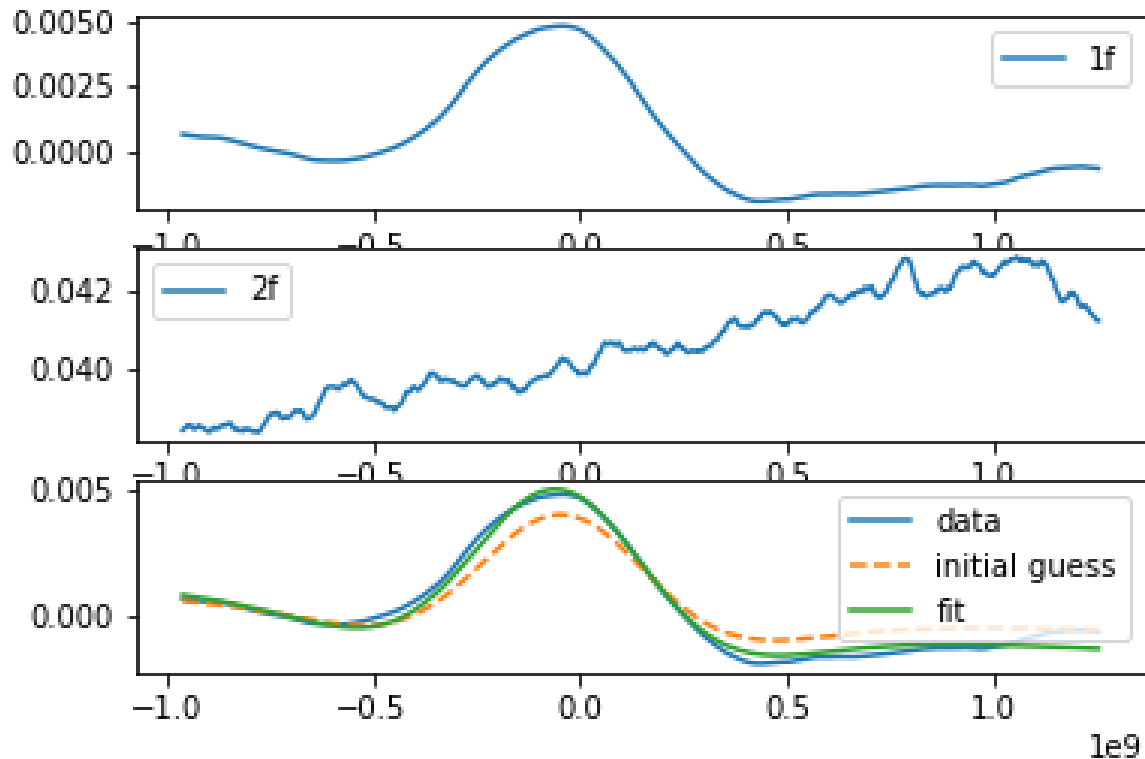


Figure 5.4: The top panel shows a typical 1f lock-in signal (Faraday rotation spectrum) of the E2 transition. The middle panel shows the 2f signal (transmission) and we suspect the slope is a result of birefringence of optics in the apparatus and laser power drift. We can further investigate this effect by altering optical configurations in future scans. The bottom panel shows the fitted curve along with the input initial guesses.

Lorentzian widths at various temperatures. Unlike the clear correspondence between the data scatter and functional form we observe in Figure 5.5, the Lorentzian widths have an ambiguous upwards trend, but show significant divergence from the expected shape. Further study of the behavior of the Lorentzian width is needed to address this problem. However, the deviation of our small set of Lorentzian widths from the expected curve should not discourage us from trusting the present experimental and analysis method. After all, the Lorentzian width ( $\sim 50$  MHz) is an order of magnitude smaller than its Gaussian counterpart ( $> 500$  MHz). Therefore, the overall width extracted by the fitting program has a higher precision and reliability than what it may appear in the scattering of fitted Lorentzian widths.

One important systematic error source is the external magnetic field generating the Zeeman effect in the lead cell. As we stated earlier, we do not have a way to quantitatively convert the current strength driving the Helmholtz coils to the longitudinal magnetic field strength at high temperatures above the Ni's (contained in the heating element) Curie point, but

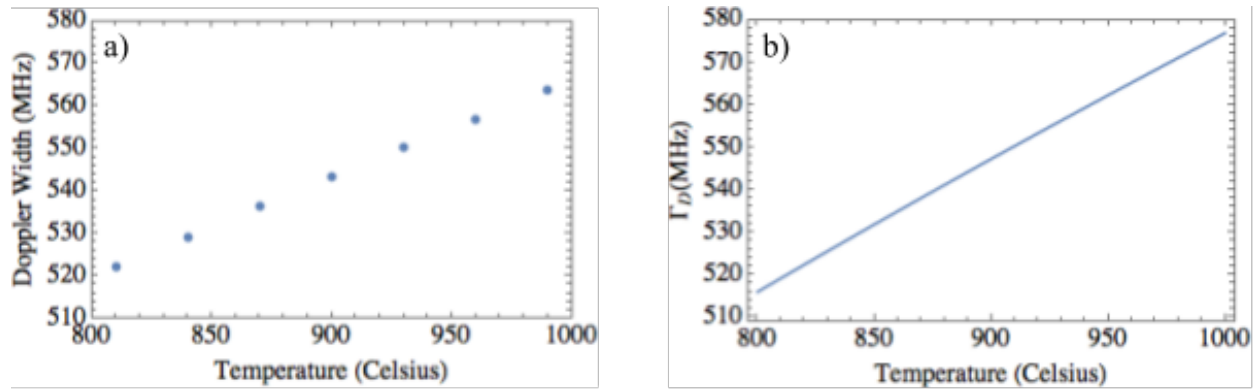


Figure 5.5: a) shows the extracted Doppler widths plot against temperature. b) the relationship between the expected Doppler width and temperature (Equation 2.6). They agree in the general shape up to a scaling factor.

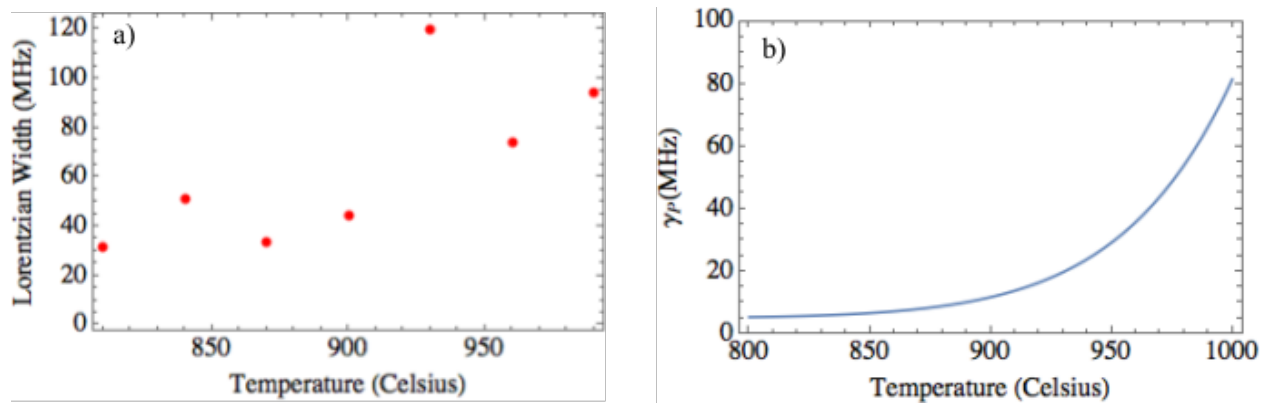


Figure 5.6: a) shows the extracted Lorentzian widths plot against temperature. b) the general relationship (Equation 2.11) between the collisional width and temperature, up to a scaling factor.

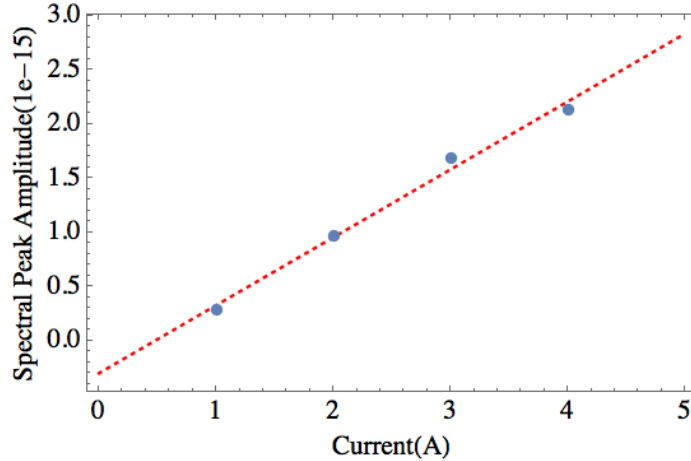


Figure 5.7: The measured spectral amplitudes plotted against the current driving the magnetic field coils. The linear relationship indicates that the observed peak amplitude simply scales with the field strength as expected from theory.

we estimate the magnetic field to scale linearly with the applied current in the low field regime. Then, the observed peak height should have a linear relationship with the current, while the shape of the Faraday rotation curve and thus the widths should not be altered. Figure 5.7 and Figure 5.8 illustrate the fitted amplitude and Lorentzian width  $\gamma$  in relation to the applied current magnitude. The observed peak amplitude scales with the current as we predicted, but no conclusion can be drawn concerning the relationship between the extracted Lorentzian width and current (magnetic field). Limited by the sample size, it is premature to determine if there is a trend in the way that  $\gamma$  varies with current, or if we just see scattering data points. More data need to be taken for statistics and we could add error bars to these data point by looking at the scattering of values of  $\gamma$  at a given field strength.

The refinement of the analysis routine shall be continued as we collect more data of both the E2 and the M1 transition and we are confident to improve the fitting scheme and come up with a reasonable uncertainty range of the Lorentzian width  $\gamma$ . It is worth reminding ourselves again that the uncertainty in the Lorentzian width parameter plays a small role when it comes to the ratio between the two transition amplitudes. Eli derived the error propagation relationship between the Lorentzian width and the transition amplitudes [6]:

$$\begin{aligned} \frac{\Delta\Gamma}{\Gamma} &= 0.05 \frac{\Delta E2}{E2}, \\ \frac{\Delta\Gamma}{\Gamma} &= 0.07 \frac{\Delta M1}{M1}. \end{aligned} \tag{5.1}$$

Given this error propagation relation, approximately 15% to 20% uncertainty in the Lorentzian width would suffice to achieve our goal of  $\sim 2\%$  error in the final ratio measurements. Therefore, our experimental and analysis method is very promising to produce a high-precision

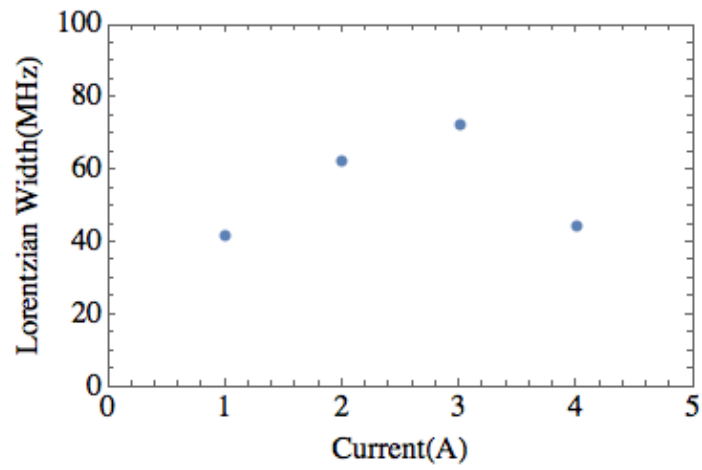


Figure 5.8: The fitted Lorentzian widths plotted against the current driving the magnetic field coils.

measurement of the E2 transition amplitude.

# Chapter 6

## Future Work

### 6.1 Complete the Lead E2 Transition Measurement

We hope to complete the high-precision measurement of the lead E2 transition amplitude in the very near future. We first need to incorporate some minor adjustments into the current experimental setup and further refine our analysis scheme. Then, an abundant amount of data shall be collected to achieve our desired statistical precision, and multiple data sets will need to be taken under varying experimental conditions to look for systematic errors. We hope to achieve a final result of the E2 transition amplitude with an approximately 2% uncertainty level.

#### 6.1.1 Improvement in the Heating Element

Our current apparatus setup is mostly well-developed and reliable, with the only exception concerning the oven's heating system. At the moment, we detect abnormal fluctuation in the resistance of one of the four clam shell heaters. It takes time to customize a new heater with matching size. As a temporary solution, we put a load in series to avoid too high of a current when the resistance of the malfunctioning heater drops. We match the output power of the other three heaters with it so that the heating process is still uniform. In the future, the imperfect clam shell heater will be replaced.

#### 6.1.2 Refinement of the Analysis Program using Data from the M1 Transition

As I alluded in chapter 5, the M1 transmission and Faraday rotation spectra together provide a more ideal testing field for our fitting programs. We would like to further test the robustness

of our present analysis routine using the M1 transmission and Faraday rotation data. We will extract Lorentzian and Gaussian width parameters from the two different lineshapes and compare the results, whose consistency assures the fitting program’s reliability.

Moreover, the analysis program ultimately aims to extract the transition amplitude ratio between the E2 and the M1 transitions. We need the transmission and Faraday rotation spectra from both transitions in order to verify that the existing fitting scheme is successful and efficient to yield the transition amplitudes’ ratio.

### 6.1.3 Systematic Error Exploration

Once we improve the experimental apparatus and refine our data analysis routine, we aim to collect many data sets under varying experimental conditions both to accumulate statistical consistency and to seek potential systematic error sources, similar to the systematics exploration in our indium Stark shift experiment. Apart from the atomic system’s temperature and the applied magnetic field strength, we shall consider controlling parameters such as the laser power, polarization, scanning direction and period.

## 6.2 Future Applications of the Faraday Rotation Technique

### 6.2.1 Hyperfine Structure and Isotope Shift Measurements in $^{207}\text{Pb}$ $6p^2\ ^3P_2$ Using Faraday Rotation Spectroscopy

After completing the current lead E2 transition measurement, we plan to include another more interesting isotope of lead,  $^{207}\text{Pb}$ , into the picture. As we previously mentioned,  $^{207}\text{Pb}$  has hyperfine structure (HFS), a feature that would radically complicate the Faraday lineshapes as the Zeeman effect mixes with hyperfine splittings. However, it serves as a great testbed if HFS is indeed what we want to investigate. In Hoenig’s thesis [6], the HFS and transition isotope shift (TIS) in the lead  $6s^26p^2\ ^3P_1$  were measured through the M1 excitation path using absorption spectroscopy. Assisted with our sensitive Faraday rotation technique, we could conduct these measurements in the otherwise “invisible” E2 transition.

To do so, we will replicate the Faraday rotation unit, which is composed of the oven system, the polarimetry scheme and the Faraday modulation rod, as described in chapter 4, but the oven contains a nearly pure  $^{207}\text{Pb}$  cell instead. The two Faraday rotation units containing two Pb isotopes will be placed side-by-side, and we direct the 940 nm ECDL to both cells. With the appropriate modulation-demodulation method using Faraday rods in the beam paths through both lead cells, we could acquire high quality spectra for both isotopes. The optical design may be readily adjusted from the current setup to pass the laser light through

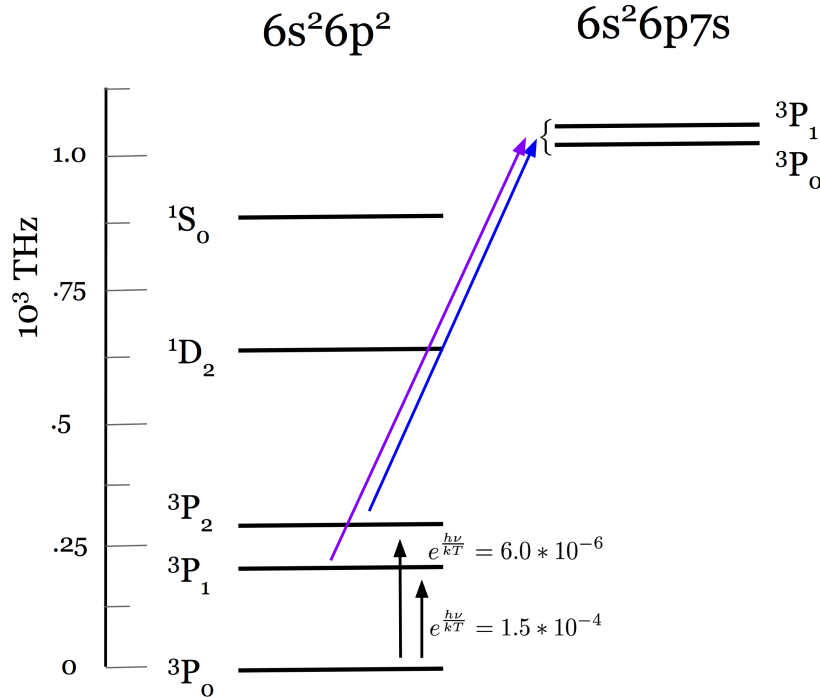


Figure 6.1: Low-lying states for  $^{208}\text{Pb}$ . The fractional populations of lead atoms (determined by thermal excitation) at the two ground states are shown for a temperature of  $1000^\circ\text{C}$ . The indicated transition path requires the driving laser to be around 368 nm.

both heated lead isotope cells and collect the transmitted spectra. As mentioned earlier,  $^{208}\text{Pb}$ , the isotope void of hyperfine structure, simplifies the lineshape analysis. For the odd isotope  $^{207}\text{Pb}$ , the LS-coupling Zeeman effect theory no longer captures the whole picture due to the mixing between Zeeman shifted levels and the hyperfine levels. More theoretical work is necessary for developing an analysis routine for the more complicated  $^{207}\text{Pb}$  spectra.

### 6.2.2 368 nm ECDL Construction for Probing a Lead Transition

Another promising future project relevant for further study of  $^{208}\text{Pb}$  involves constructing an ECDL tuned to roughly 368 nm. As Figure 6.1 shows, we would like to study the  $6s^2 6p^2 \rightarrow 6s^2 6p 7s$  transition. The resonant frequency of light needed is at 368.34 nm, a wavelength that is slightly below the lower operation limit of a diode laser in room temperature. We would like to build an ECDL using a commercial 375 nm diode (from Toptica), which has worked in ECDLs down to 369 nm. We hope to achieve a wavelength just below 369 nm by cooling the diode below a standard TEC.

### 6.3 Stark Shift Polarizability Measurements in Thallium or Lead Atomic Beam

Our recent work in the series of experiments in measuring the Stark shift polarizabilities in indium atomic beam inspires similar projects of Stark shift measurements in another Group IIIA element, thallium. The current atomic beam experimental setup can be readily adapted for measuring thallium polarizability, as well as the data acquisition and analysis scheme. In particular, our theoretical approach and experimental strategy of the indium  $7P_{3/2}$  states with scalar *and* tensor polarizabilities can be transferred to the case of thallium  $7P_{3/2}$  and  $8P_{3/2}$  excited states. In particular, we have precisely measured the hyperfine structure in the  $8P_{3/2}$  state in thallium using our two-step excitation method in a vapor cell (for results see Ref. [6]). Hence, we are equipped with the optical devices to conduct an atomic beam measurement for the same two-step transition.

The atomic beam apparatus could also cater to the study of the Stark shift effect in lead, offering guidance for the wavefunction calculation of the even more exciting four-valence-electron system. One example candidate electric dipole transition paths are  $6s^26p^2\ ^3P_{1,2} \rightarrow 6s^26p^27s\ ^3P_{0,1}$ , the transition that our cooled diode laser would be required to realize. Our group has never conducted atomic beam experiment with lead and this promising future project would be an exciting start.

# Appendix A

## Summary of Indium Polarizability Data

### A.1 Indium $7P_{1/2}$ data summary

Over the period of several months, we collected over 1000 scans of data for the  $7P_{1/2}$  state Stark shift. Below, we summarize the collected data sets under various experimental conditions for the purpose of checking systematic error sources. Not all controlled experimental parameters are listed in Table A.1. Instead, we selected a few main varying experimental conditions of the atomic beam unit for display and comparison. Information about other controlling variables, such as the polarization and power of light going through the indium cell, the vapor cell temperature, as well as the time constant and sensitivity setting of the lock-in amplifiers, are omitted for clarity.

Table A.1: The summary of collected indium  $7P_{1/2}$  Stark shift data. The “Voltages” column specify the order of voltage associated with the applied electric field in each scanning cycle. The two columns titled  $\lambda/2$  indicate the values of the two half-wave plates in the UV and red laser beam paths, by adjusting which, we alter the relative polarization of the first-step and second-step light.

| Set | Voltages (in order) | First Step | Period (s) | Red $\lambda/2$ | UV $\lambda/2$ | UV Power( $\mu$ W) | Red Power(mW) | Temp ( $^{\circ}$ C) | nscans |
|-----|---------------------|------------|------------|-----------------|----------------|--------------------|---------------|----------------------|--------|
| 1   | 3,1,5,2,4           | F=4 ->F'=5 | 33.2       | 106             | 309            | 543                | 5             | 1100                 | 24     |
| 2   | 4,2,5,1,3           | F=4 ->F'=5 | 32.9       | 106             | 309            | 534                | 5.09          | 1110                 | 24     |
| 3   | 1,5,4,2,3,6         | F=4 ->F'=5 | 31         | 150             | 309            | 602                | 5             | 1100                 | 24     |
| 4   | 3,1,5,2,4           | F=4 ->F'=5 | 23.6       | 150             | 309            | 600                | 5             | 1100                 | 24     |
| 5   | 2,4,3,5,1           | F=4 ->F'=5 | 23.5       | 150             | 309            | 700                | 5.05          | 1100                 | 24     |
| 6   | 2,3,1,5,4           | F=4 ->F'=5 | 31         | 150             | 309            | 530                | 4             | 1100                 | 24     |
| 7   | 3,5,2,6,4           | F=5 ->F'=4 | 31         | 195             | 309            | 713                | 4.51          | 1100                 | 24     |
| 8   | 4,2,6,3,5           | F=5 ->F'=4 | 29.2       | 195             | 309            | 634                | 4.28          | 1100                 | 24     |
| 9   | 3,6,4,5,2           | F=5 ->F'=4 | 29.6       | 150             | 309            | 650                | 4.48          | 1100                 | 24     |
| 10  | 4,5,2,6,3           | F=5 ->F'=4 | 28.2       | 195             | 309            | 654                | 4.12          | 1100                 | 24     |
| 11  | 2,4,6,5,3           | F=5 ->F'=4 | 28.7       | 195             | 309            | 545                | 4.8           | 1100                 | 24     |
| 12  | 5,3,6,2,4           | F=5 ->F'=4 | 28.6       | 195             | 280            | 685                | 4.54          | 1100                 | 24     |
| 13  | 4,6,5,3             | F=4 ->F'=5 | 28.7       | 150             | 309            | 692                | 4.56          | 1100                 | 24     |
| 14  | 3,5,2,4,6           | F=4 ->F'=5 | 28.9       | 150             | 309            | 623                | 4.77          | 1100                 | 24     |

## A.2 Indium $7P_{3/2}$ data summary

Likewise, we summarize the acquired data for the  $7P_{3/2}$  state in Table A.2. We collect data for the  $7P_{3/2}$  case in the low electric field and high electric field regimes so that both the scalar piece and the tensor piece of polarizability could be extracted.

Table A.2: The summary of collected indium  $7P_{3/2}$  Stark shift data. The ‘‘Voltages’’ column specify the order of voltage associated with the applied electric field in each scanning cycle. Note that some sets are taken in the low field regime, while the rest are taken at higher frequencies where the tensor component of the polarizability becomes prominent. Similar to Table A.1, the columns titled  $\lambda/2$  suggest the relative polarization of the two laser radiations.

| Set | Voltages(kV)  | First Step              | Period (s) | Red $\lambda/2$ | UV $\lambda/2$ | UV Power( $\mu$ W) | Red Power(mW) | Temp( $^{\circ}$ C) | nscans |
|-----|---------------|-------------------------|------------|-----------------|----------------|--------------------|---------------|---------------------|--------|
| 1   | 1.5, 1, 2     | F=4 ->F <sup>i</sup> =5 | 16.2       | 105             | 310            | 616                | 4.82          | 1140                | 24     |
| 2   | 1.5,2.5,1,3,2 | F=4 ->F <sup>i</sup> =5 | 16.2       | 105             | 310            | 683                | 4.85          | 1100                | 30     |
| 3   | 2,1.5,3,1,2.5 | F=4 ->F <sup>i</sup> =5 | 16.2       | 150             | 310            | 756                | 4.89          | 1100                | 30     |
| 4   | 2.5,1.5,2,1,3 | F=4 ->F <sup>i</sup> =5 | 16.2       | 105             | 265            | 576                | 4.82          | 1100                | 30     |
| 5   | 14,15,16      | F=4 ->F <sup>i</sup> =5 | 33.2       | 140             | 305            |                    |               | 1100                | 22     |
| 6   | 14,15,16      | F=4 ->F <sup>i</sup> =5 | 33.2       | 140             | 305            | 574                | 4.76          | 1100                | 24     |
| 7   | 14, 15, 16    | F=4 ->F <sup>i</sup> =5 | 35.1       | 140             | 305            | 579                | 4.91          | 1100                | 24     |
| 8   | 13,14,15,16   | F=4 ->F <sup>i</sup> =5 | 17.5       | 96              | 320            | 546                | 5.04          | 1100                | 24     |
| 9   | 13,14,15,16   | F=4 ->F <sup>i</sup> =5 | 19.5       | 96              | 290            | 539                | 5.04          | 1100                | 24     |
| 10  | 13,14,15,16   | F=4 ->F <sup>i</sup> =5 | 19.5       | 80              | 320            | 527                | 4.97          | 1100                | 24     |
| 11  | 1.5,2.5,2,3,1 | F=4 ->F <sup>i</sup> =5 | 16.3       | 120             | 310            |                    |               | 1100                | 30     |
| 12  | 2.5,1.5,2,1,3 | F=4 ->F <sup>i</sup> =5 | 12.9       | 120             | 310            | 408                | 3.89          | 1100                | 30     |
| 13  | 2,1.5,3,1,2.5 | F=4 ->F <sup>i</sup> =5 | 13.6       | 105             | 310            | 408                | 4.27          | 1100                | 30     |
| 14  | 2,1.5,3,1,2.5 | F=4 ->F <sup>i</sup> =5 | 13.9       | 120             | 310            | 372                | 3.76          | 1100                | 30     |
| 15  | 1.5,3,2,2.5,1 | F=4 ->F <sup>i</sup> =5 | 14.7       | 105             | 310            | 340                | 3.86          | 1100                | 30     |
| 16  | 3,2,1.5,1,2.5 | F=4 ->F <sup>i</sup> =5 | 13.7       | 132             | 310            | 338                | 3.98          | 1100                | 30     |
| 17  | 1.5,3,1,2,2.5 | F=4 ->F <sup>i</sup> =5 | 14.5       | 120             | 330            | 341                | 4.21          | 1100                | 30     |
| 18  | 2.5,2,1,3,1.5 | F=5 ->F <sup>i</sup> =4 | 16.5       | 198             | 348            | 1200               | 8.2           | 1080                | 30     |
| 19  | 2,1,3,2.5,1.5 | F=5 ->F <sup>i</sup> =4 | 25.2       | 198             | 348            | 650                | 8.3           | 1100                | 30     |
| 20  | 2,1,3,2.5,1.5 | F=5 ->F <sup>i</sup> =4 | 18.4       | 198             | 348            | 335                | 8.2           | 1100                | 30     |
| 21  | 1.5,3,1,2,2.5 | F=5 ->F <sup>i</sup> =4 | 16.1       | 198             | 348            | 630                | 3.8           | 1100                | 30     |
| 22  | 2.5,1,3,1.5,2 | F=5 ->F <sup>i</sup> =4 | 16.1       | 245             | 348            | 690                | 7.6           | 1100                | 30     |
| 23  | 2,3,2.5,1,1.5 | F=5 ->F <sup>i</sup> =4 | 14.1       | 245             | 300            | 610                | 4             | 1100                | 30     |
| 24  | 2.5,2,1,3,1.5 | F=5 ->F <sup>i</sup> =4 | 14.1       | 198             | 348            | 670                | 7.7           | 1100                | 30     |
| 25  | 3,2           | F=5 ->F <sup>i</sup> =4 | 14.1       | 198             | 348            | 675                | 4             | 1100                | 30     |

# Bibliography

- [1] D. DeMille, J. M. Doyle, and A. O. Sushkov, *Science* pp. 990–994 (2017).
- [2] P. A. Vetter, D. M. Meekhof, P. K. Majumder, S. K. Lamoreaux, and E. N. Fortson, *Phys. Rev. Lett.* **74**, 2658 (1995).
- [3] U. I. Safronova, M. S. Safronova, and M. G. Kozlov, *Phys. Rev. A* **76**, 022501 (2007).
- [4] S. G. Porsev, M. G. Kozlov, M. S. Safronova, and I. I. Tupisyn, *Phys. Rev. A* **93** (2016).
- [5] N. B. Vilas, Bachelor’s thesis, Williams College (2017).
- [6] E. V. Hoenig, Bachelor’s thesis, Williams College (2017).
- [7] B. L. Augenbraun, Bachelor’s thesis, Benjamin L. Augenbraun (2015).
- [8] A. L. Carter, Bachelor’s thesis, Williams College (2016).
- [9] N. B. Vilas, B.-Y. Wang, P. M. Rupasinghe, D. L. Maser, M. S. Safronova, U. I. Safronova, and P. K. Majumder, *Phys. Rev. A* **97**, 022507 (2018).
- [10] W. Demtröder, *Laser Spectroscopy: Basic Concepts and Instrumentation* (Springer, 1998), 2nd ed.
- [11] D. Budker, D. F. Kimball, and D. P. DeMille, *Atomic Physics - An Exploration Through Problems and Solutions* (Oxford, 2004).
- [12] P. A. Vetter, Ph.D. thesis, University of Washington (1995).
- [13] R. W. Schmieder, *American Journal of Physics* **40**, 297 (1972).
- [14] J. Mitroy, M. S. Safronova, and C. W. Clark, *J. Phys. B* **43**, 202001 (2010).
- [15] M. S. Safronova, U. I. Safronova, and S. G. Porsev, *Phys. Rev. A* **87**, 032513 (2013).
- [16] G. Ranjit, N. A. Schine, A. T. Lorenzo, A. E. Schneider, and P. K. Majumder, *Phys. Rev. A* **87**, 032506 (2013).
- [17] V. Gerginov, A. Derevianko, and C. E. Tanner, *Phys. Rev. Lett.* **91**, 072501 (2003).

- [18] G. Woodgate, *Elementary Atomic Structure* (Clarendon Press, 1983), 2nd ed.
- [19] R. J. Rafac and C. E. Tanner, Phys. Rev. A **58**, 1087 (1998), URL <https://link.aps.org/doi/10.1103/PhysRevA.58.1087>.
- [20] B. L. Augenbraun, A. Carter, P. M. Rupasinghe, and P. K. Majumder, Phys. Rev. A **94**, 022515 (2016).
- [21] N. A. Schine, Bachelor's thesis, Williams College (2013).
- [22] D. M. Meekhof, Ph.D. thesis, University of Washington (1994).
- [23] C. B. Alcock, V. P. Itkin, and M. K. Horrigan, Canadian Metallurgical Quarterly **23** (1084).